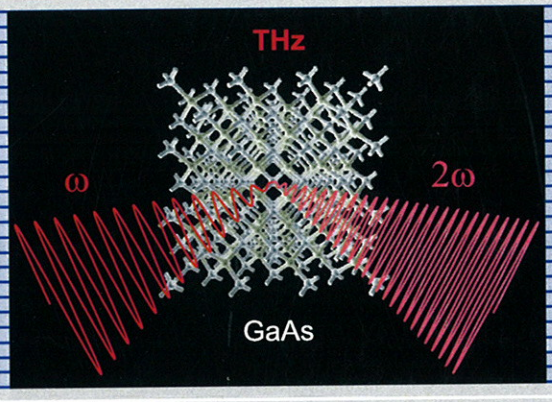


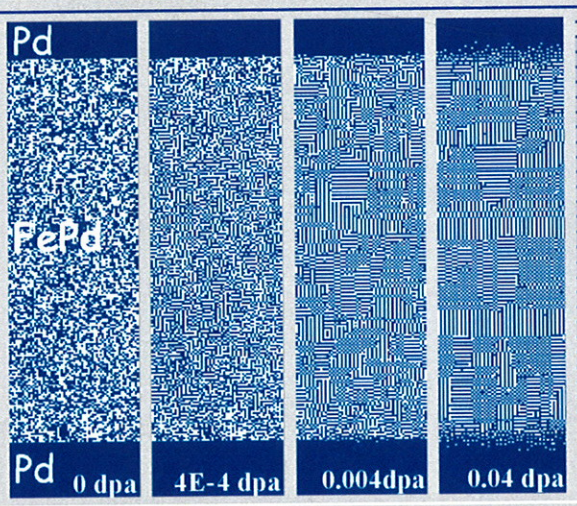


Wissenschaftlich-Technische Berichte
FZR-396 2004 · ISSN 1437-322X

# Annual Report 2003

## Institute of Ion Beam Physics and Materials Research

Forschungszentrum
Rossendorf

Wissenschaftlich-Technische Berichte
**FZR-396**
2004

# Annual Report 2003

## Institute of Ion Beam Physics and Materials Research

**Editors:**
**J. von Borany, V. Heera, M. Helm,**
**H. U. Jäger, W. Möller**

Forschungszentrum
Rossendorf

Cover Pictures:

Left:

Schematic sketch of the nonlinear-optical frequency conversion in a GaAs crystal at THz frequencies. The second harmonic generation of an input frequency is resonantly enhanced, when the frequency corresponds to half the optical phonon frequency of 8.8 THz.
See contribution at page 9.

Right:

Snapshots from Kinetic Monte Carlo simulation showing vacancy-induced "$L1_0$" chemical ordering during He ion irradiation at 550 K of a ~ 60 nm FePd film sandwiched between Pd buffer and capping layers. Due to their very large magnetic anisotropy such films are excellent candidates for future magnetic media. For details see page 21.

Forschungszentrum Rossendorf e.V.
Institut für Ionenstrahlphysik und Materialforschung

Postfach 51 01 19
D-01314 Dresden
Bundesrepublik Deutschland

| | | |
|---|---|---|
| Direktoren | Prof. Dr. Manfred Helm | Prof. Dr. Wolfhard Möller |
| Telefon | + 49 (3 51) 2 60 22 60 | + 49 (3 51) 2 60 22 45 |
| Telefax | + 49 (3 51) 2 60 32 85 | + 49 (3 51) 2 60 32 85 |
| E-mail | m.helm@fz-rossendorf.de | w.moeller@fz-rossendorf.de |
| Internet | http://www.fz-rossendorf.de/FWI | |

# Preface

The Institute of Ion Beam Physics and Materials Research (IIM) combines basic research and application-oriented studies in the fields of ion beam applications to materials and semiconductor research, with more than 100 scientists, engineers, technicians and PhD and diploma students. The institute operates a national and international ion beam center, which, in addition to its own scientific activities, offers services and transfers know-how on ion beam techniques to universities, other research institutes, and industry.

Together with four other scientific institutes, IIM is part of Forschungszentrum Rossendorf (FZR) which represents the largest governmental research institution in the "new" states of the Federal Republic of Germany, with R&D activities in the fields of the structure of matter, life sciences, and environment and safety. FZR is a member of the "Leibniz Society" (WGL), with the federal government and the federal state of Saxony each contributing about 50 % of the basic funding.

At IIM, a broad range of ion-related equipment is available, delivering ions with energies from about 10 eV (plasma treatment) to several 10 MeV (electrostatic accelerators), which are used for thin film synthesis, modification and analysis. For the diagnostics of ion-treated surfaces, other standard analytical techniques are available such as transmission electron microscopy, X-ray diffraction, Auger and photoelectron spectroscopy, and a number of chemical, mechanical, electrical and optical diagnostics. The latter facilities have been expanded recently to enable various kinds of ultrafast and stationary optical investigations over a wide frequency range. Exciting new possibilities will be soon provided by the infrared free-electron laser, which is presently under construction at the FZR in connection with the ELBE superconducting electron linear accelerator. Sample processing is routinely done in a class 100 cleanroom.

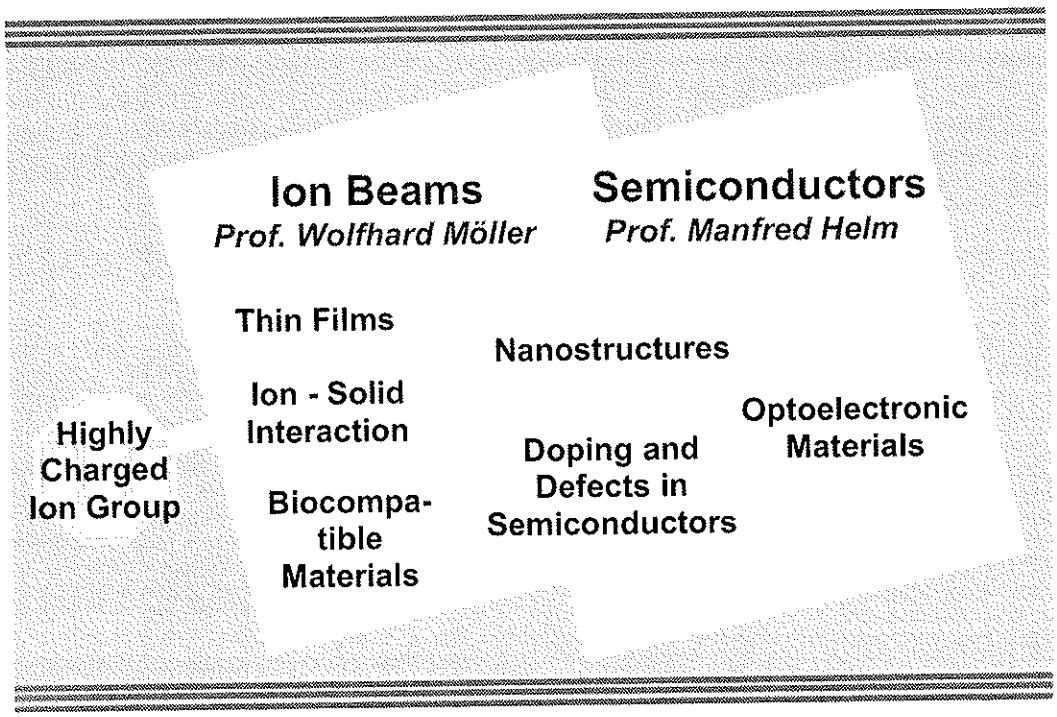


The diagram displays the main R&D activities of the institute. In the field of ion-solid interaction, the activities have been strengthened in 2003 by forming a research group for the study of the effects of highly charged ions interacting with surfaces. In addition, the institute now hosts the Highly Charged Ion Group of the Technical University of Dresden (Leader: Dr. G. Zschornack). In cooperation of both

groups, a new and unique irradiation facility is presently under construction which will provide both high fluxes of ions of medium charge states and low fluxes of ions of the highest charge states.

It is the purpose of the present Annual Report to document its scientific progress in 2003 by a few selected extended contributions, numerous short contributions, and a statistical overview on publications, conference contributions and lectures given by members of the institute. It also reports on the training of young scientists and on external and collaborative actions.

The European user programs at the Large Scale Facilities "Center for Application of Ion Beams in Materials Research" ("AIM"), and "Synchrotron Radiation Beamline for Radiochemistry and Materials Research (ROBL)" at the ESRF in Grenoble have been concluded in 2003. Unfortunately, the applications for extensions within the 6$^{th}$ Framework Programme were not successful. Nevertheless, the institute still hosted a large number of national and European guests. An appreciable number of PhD students from other European laboratories made use of the Marie-Curie Training Site "Development of Functional Layers Using Ion Beam Techniques" funded by the European Union.

The scientific progress of the institute is documented by an increased number of publications with respect to 2002, in particular in journals with high impact factor. In 2003, three diploma students and three PhD students finished their theses at the institute and their examinations at the Technical University of Dresden. The institute co-organized a summer school "Vacuum, Electron and Ion Technologies" at Varna (Bulgaria).

Industrial activities have significantly expanded in 2003. In cooperation with the small spin-off enterprise "nanoparc", a wafer-handler end station has been set up for high-energy implantation into power semiconductors. In 2003, two patents have been issued, and seven additional patents have been submitted for approval.

The institute would like to thank all partners and friends, and the organizations who supported its progress in 2003. Special thanks are due to the Executive Board of the Forschungszentrum Rossendorf, the Minister of Science and Arts of the Free State of Saxony, and the Minister of Education and Research of the Federal Government of Germany. Our partners from universities, industry and research institutes all around the world contribute essentially to the success of the institute, and play a crucial role for its further development. Last but not least, the directors would like to thank all staff of the institute for their active and excellent contributions in 2003.

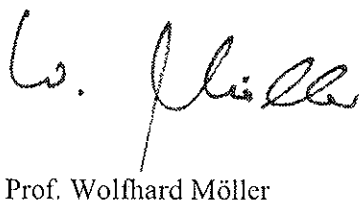

Prof. Wolfhard Möller

Prof. Manfred Helm

# Contents

## Selected Reports



## Short Contributions

## Statistics

# Selected Reports

# Infrared Phonon-Polariton Resonance of the Nonlinear Susceptibility of GaAs Investigated with a Free-Electron Laser

T. Dekorsy, V.A. Yakovlev[1], W. Seidel[2], M. Helm and F. Keilmann[3]

[1] *Institute of Spectroscopy, Russian Academy of Sciences, Troitsk, Russia;*
[2] *Institut für Kern und Hadronenphysik, Forschungszentrum Rossendorf;*
[3] *Max-Planck-Institut für Biochemie, Martinsried*

Since the invention of lasers the field of nonlinear optics evolved rapidly starting with the observation of frequency doubling of a pulsed ruby laser in crystalline quartz in 1961 [1]. Since these times a multitude of materials has been investigated and developed in order to yield high second order nonlinear susceptibilities for frequency conversion, enabling the generation of light from the mid IR to the UV covering many wavelengths where no laser source directly emits radiation. However, in the THz frequency range (1-10 THz) a remarkable gap exists in the availability of tunable and intense light sources with the consequence that nonlinear optics in this frequency range remains to great extents unexplored [2]. Thus - since the pioneering work of Faust and Henry on frequency mixing with a HeNe laser and a far-infrared (FIR) $H_2O$ laser in GaP [3] and microwave-mixing experiments in a variety of crystals by Boyd *et al.* [4] - only a few experiments on the dispersion of the nonlinear susceptibility in the THz frequency range have been performed [5-7]. The lack of firm experimental data on a large number of technologically important crystals has been an obstacle for the development of quantitative theories. In the last decade intense free-electron lasers (FEL) tunable in the FIR have become available for the study of nonlinear optical phenomena. Recently, the first quantum cascade laser has been realized in a GaAs/AlGaAs heterostructure emitting at 4.4 THz, which may open the door for integrated nonlinear optics in this frequency range [8]. Here we report on a study of second harmonic generation (SHG) in the range of 4.0 THz to 6.0 THz in thin GaAs films performed with a FEL. These experiments provide deeper insight into the influence of higher-order terms of the lattice potential on the nonlinear susceptibility in the THz frequency range and thus on the lattice potential in general [9].

The nonlinear optical susceptibility in semiconductors in the THz frequency range is governed by the superposition of electronic and ionic contributions. Faust and Henry were the first to determine the dispersion of the THz nonlinear susceptibility in GaP [3]. They observed a resonance enhancement at the TO phonon frequency and showed that the ionic and electronic contributions are of opposite sign, leading to a cancellation of both contributions below the phonon resonance. They showed theoretically that the pure electronic susceptibility $\chi_E^{(2)}$ is related to the dispersion of the susceptibility in the FIR for the case of frequency mixing via Eq. 1

$$\chi^{(2)}(\omega_1-\omega,\omega,\omega_1)=\chi_E^{(2)}\left[1+C_1\frac{1}{D(\omega)}\right] \quad (1)$$

with $D(\omega)=1-(\omega/\omega_{TO})^2-i\omega\gamma/\omega_{TO}^2$, $\omega_{TO}$ the TO phonon frequency, and $\gamma$ the damping of the TO phonon. $\chi_E^{(2)}$ is the pure electronic part of the nonlinear susceptibility and can be determined experimentally from frequency doubling above the lattice resonance, in the transparent range of the crystal [10-12]. The Faust-Henry coefficient $C_1$, which is negative for most compound semiconductors, reflects the different signs of the electronic and ionic contributions to the nonlinear susceptibility [13]. This coefficient is further important since it defines the ratio between the lattice-induced and the electronic contributions to the linear electro-optic effect [5] and the relative Raman scattering intensities from LO and TO phonons [14]. Experimentally, $C_1$ can be derived from measurements of the electro-optic coefficient, by frequency mixing or by Raman scattering.

When all frequencies involved in a nonlinear interaction described by $\chi_E^{(2)}$ are below or in the vicinity of the phonon resonance, the theoretical description has to be extended by considering higher order moments of the polarization and the lattice potential. Flytzanis calculated the dispersion of the second order susceptibility below the phonon resonance on the basis of a microscopic model for the polarizability [15]. He showed that the following general expression can be derived (Eq. 2):

$$\chi^{(2)}(\omega_3,\omega_2,\omega_1)=\chi_E^{(2)}\left[\begin{array}{l}1+C_1\left(\dfrac{1}{D(\omega_1)}+\dfrac{1}{D(\omega_2)}+\dfrac{1}{D(\omega_3)}\right)\\+C_2\left(\dfrac{1}{D(\omega_1)D(\omega_2)}+\dfrac{1}{D(\omega_1)D(\omega_3)}+\dfrac{1}{D(\omega_2)D(\omega_3)}\right)\\+C_3\left(\dfrac{1}{D(\omega_1)D(\omega_2)D(\omega_3)}\right)\end{array}\right]$$

The additional *terms* as compared to Eq. 1 have the following physical background: $C_2$ represents the phonon interaction through the second-order lattice dipole moment and $C_3$ the contribution from the third-order lattice potential anharmonicity. Besides the relevance for the THz nonlinear susceptibility these terms are also important for two-phonon sidebands in the infrared absorption, for the phonon decay [15,16], and for a quantitative description of Raman spectra [17]. For a determination of the coefficients $C_2$ and $C_3$ all frequencies involved have to be below or close above the phonon resonance. However, they cannot be determined independently. The value $3C_2+C_3$ has been obtained experimentally as 0.39 from microwave mixing experiments at 57 GHz for GaAs [4]. SHG below the phonon resonance with an intense and tunable laser source would be a most attractive method for the determination of these coefficients. In order to elucidate the benefits of this method we plot in Fig. 1 the dispersion of the three contributing terms according to Eq. 2 and their sum (plus 1 according to Eq. 2) for the case of SHG ($\omega_1=\omega_2$, $\omega_3=2\omega_1$) in GaAs. The parameters used for the calculation are $\omega_{TO}$=8.05 THz, $\gamma$=0.29 THz, $\chi_E^{(2)}=134\times10^{-12}$ m/V, $C_1$=-0.59 (experimental from Ref. [5]), $C_2$=0.14, and $C_3$=-0.07 (theoretical from [15]), giving a value of $3C_2+C_3$= 0.35, which is smaller than the experimental value 0.39 from [4]. A resonance is observed in all three terms of the right-hand side of Eq. 2 at half the TO phonon frequency (4 THz). The maximum value of $\chi^{(2)}$ in resonance exceeds the pure electronic part $\chi_E^{(2)}$ by a factor of 33 and has not yet been observed for any III-V compound. Above this resonance a sign reversal occurs in $\chi^{(2)}$. This sign reversal at 5.1 THz should lead to a minimum in the SH power. This zero-crossing frequency would enable to determine $C_2$ and $C_3$, and thereby the relative importance of the second-order dipole moment vs. the third order lattice potential. This method would not require an absolute calibration of the SH conversion efficiency which is a troublesome task in the FIR.

The first frequency doubling experiments below the phonon frequency were performed by Mayer and Keilmann in GaAs using a FIR gas laser operating in the frequency range from 0.6 THz to 1.7 THz [6]. However, these frequencies were too far away from the predicted resonance (4 THz) to see any resonance enhancement in GaAs. No value for $C_2$ and $C_3$ could be determined due to the uncertainty in the measured $\chi^{(2)}$. The zero-crossing of the second order susceptibility expected around 5.1 THz could also not be observed.

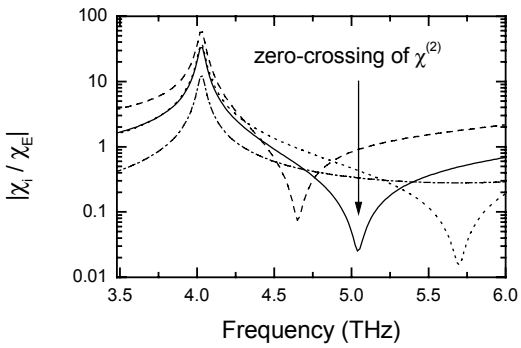


**Fig. 1:** Calculated contributions to $\chi^{(2)}_i$, relative to the electronic second order suceptibility $\chi^{(2)}_E$ according to Eq. 2 (absolute values on a logarithmic scale): $C_1$ term (dashed), $C_2$ term (dotted), $C_3$ term (dashed-dotted) and the sum of all plus 1 (solid). The arrow indicates the zero-crossing in the real part of $\chi^{(2)}$.

We perform SHG experiments on thin (211) oriented GaAs crystals with thicknesses of 7 µm to 18 µm. The crystals are of homogeneous thickness which can be determined by FIR transmission measurements to within ±2 µm. Such thin crystals are required by the short coherence length of 10-20 µm associated with the large phase mismatch for SHG in the vicinity of the phonon resonance. The FEL FELIX (Rijnhuizen, Netherlands) delivers THz pulses at a macro-bunch repetition rate of 10 Hz and a micro-bunch repetition rate of 25 MHz with 100 micro-pulses per macro-pulse. The radiation frequency is tuned between 4 THz and 6 THz with a spectral width (FWHM) of 0.2 THz to 0.25 THz and a micro-pulse energy between 4 and 8 µJ. The average power of <80 mW is low enough to avoid sample heating which could shift the phonon resonance. The

radiation was focused by a spherical mirror to a spot with < 650 µm diameter on the GaAs crystal mounted on a metallic aperture of 5 mm diameter. The SH power was measured with a high-sensitivity liquid He cooled Ge:Ga detector and integrated over a macro-pulse. Two important tasks have to be accomplished to unambiguously measure the SHG from the sample: (i) The FEL beam has to be purified from higher harmonics before the set-up, which is achieved via a crystalline quartz plate [9]. (ii) The fundamental beam transmitted through the sample has to be efficiently blocked before the detector. This is achieved with a double pass through a thick CsBr crystal [9].

Fig. 2 (a) depicts the power on the detector for a sample of 18 µm thickness vs. the fundamental frequency. Two FEL power settings, $P_0$ and $P_0/2$ are used, achieved by a calibrated broadband attenuator. A separate measurement without a sample in the beam path reveals a strongly increasing detector power for frequencies ≥5.7 THz, where CsBr starts transmitting the fundamental. In this measurement, a slight increase is also observed below 4.4 THz due to a reduced attenuation of the SH content in the FEL beam by the quartz plate. Fortunately, this signal is strongly attenuated once the GaAs sample is present, because frequencies below 8.8 THz are within the Reststrahlen band of GaAs (see e.g. inset of Fig. 3). We can conclude that the set-up is sensitive to SHG between 4.4 THz and 5.6 THz. Before we discuss the frequency dependence of the detected power in Fig. 2 (a) we check its origin. Fig. 2 (b) shows the ratio of the detector signals for the two power settings, $P_0$ and $P_0/2$. Below a frequency of 5.6 THz the ratio is close to 4 as expected for SHG. For frequencies larger than 5.8 THz the ratio drops to 2 which indicates that the fundamental is leaking through the CsBr filter, exceeding the SHG signal. The scattering of the data is due to fluctuations and drift of FEL power (each sweep of Fig. 2 (a) takes approx.~20 minutes). However, changing the fundamental power at a fixed frequency gives ratio values of 4 with errors of 10% only, for frequencies <5.6 THz. As corroborated from measurement on different sample thicknesses the data shown in Fig. 2 (a) are certainly dominated by SHG below 5.6 THz. The SHG power exhibits a maximum at 4.5 THz and drops to a minimum at approximately 5.3 THz (Fig. 2 (a)). Both features are reproduced in samples of different thickness (not shown). The maximum at 4.5 THz is the first observation of a resonant enhancement of SHG close to half the phonon energy. The maximum is shifted to somewhat higher frequencies due to the strong absorption of the SHG at $\omega=\omega_{TO}$ (see calculations below).

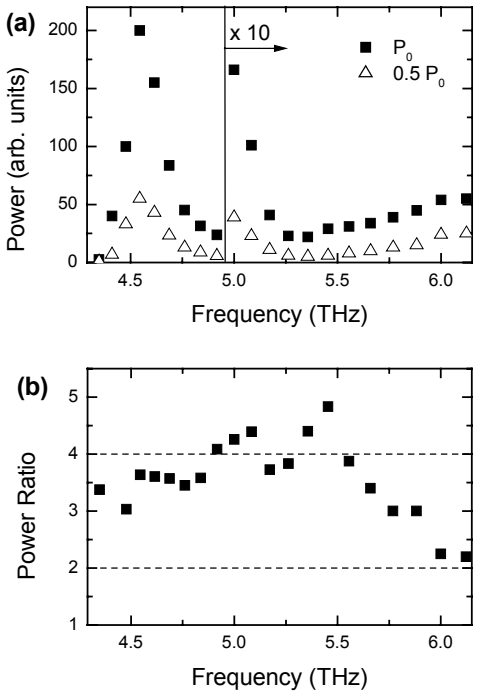


**Fig. 2:** (a) Detector signal vs. fundamental FEL frequency measured with a 18 µm thick, (211) oriented GaAs crystal. For frequencies above 4.9 THz the data are multiplied by 10. (b) Ratio of the detector signal for power settings $P_0$ and $P_0/2$ vs. fundamental FEL frequency.

The minimum observed is a clear indication of a strong drop of $\chi^{(2)}$. Since the expected rise at higher frequencies cannot be certified from the data unambiguously due to insufficient filtering of fundamental FEL power on the detector, this minimum position represents a *low-frequency* limit only of the zero-crossing of $\chi^{(2)}$. Therefore, the zero-crossing frequency is significantly higher than 5.1 THz calculated with the $C_i$ values used in Fig. 1. For a comparison we calculate the SH power including phase-matching, absorption at the fundamental and the SH frequency, the finite sample thickness, and Fresnel losses [6,7,18]. The dielectric function is calculated from an oscillator model. Fig. 3 shows the calculated SHG power for three different sets of $C_i$ values for a sample thickness of 18 µm. In addition to the dispersion of $\chi^{(2)}$ shown in Fig. 1 the SHG power is modified by the strong dispersion of the phase matching condition and the strong absorption of the SH wave close to the TO phonon. The maximum position observed around 4.5 THz is due to a maximum transmission of the GaAs crystal at the second harmonic frequency (see inset of Fig. 3). The signal decrease below 4.5 THz, likewise, is due to the Reststrahlen minimum transmission. Inserting the value for $\chi^{(2)}(\omega)$ of Fig. 1 (with

$C_1$=-0.59, $C_2$=0.14, $C_3$=-0.07) predicts the SHG minimum and a zero-crossing at 5.1 THz. Using the experimental value $3C_2 + C_3$=0.39 (while keeping the ratio $C_2/C_3$ fixed at the theoretical value of -2.0, i.e. $C_2$=0.156, $C_3$=-0.078) would result in a slightly smaller zero-crossing frequency of 5.08 THz. In order to match the zero-crossing to the experimentally observed value of 5.3 THz, the ratio of $C_2/C_3$ has to be changed significantly from -2.0 to values between -1.23 and -1.30 with corresponding values of $3C_2 + C_3$ between 0.35 and 0.39, respectively. We thus conclude that the contribution of the phonon interaction through the third-order lattice potential anharmonicity ($C_3$) is significantly larger than calculated by theory [15], relative to the contribution from the second-order lattice dipole moment ($C_2$).

In summary we observed the resonance of the second order nonlinear susceptibility of GaAs at half the phonon frequency [9]. A vanishing SHG power between half the phonon frequency and the phonon frequency has been observed as predicted. This minimum in the SHG is based on the cancellation of the electronic and ionic part - including higher-order polarizations and lattice potential anharmonicity - of the susceptibility. The determination of this zero-crossing allows us to derive new weights of relative contributions to the second order nonlinear susceptibility. We believe that the presented method is valuable for the determination of these coefficients in other technologically important materials.

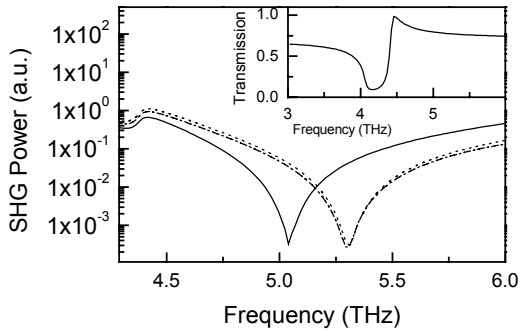


**Fig. 3:** Calculated SHG power for a 18 µm thick GaAs film for 3 different sets of $C_i$'s: $C_2/C_3$=-2.0, $3C_2+C_3$=0.35 (solid), $C_2/C_3$=-1.23, $3C_2+C_3$=0.35 (dotted), $C_2/C_3$=-1.3, $3C_2+C_3$=0.39 (dashed-dotted). The inset depicts the transmission coefficient at the SH frequency vs. the fundamental frequency.

## Acknowledgements

We thank J. Kuhl and A.F.G. van der Meer for fruitful discussions. We gratefully acknowledge the support by the Stichting voor Fundamenteel Onderzoek der Materie (FOM) in providing the required beam time on FELIX and highly appreciate the skilful assistance by the FELIX staff. This work was supported in part under the 'Access to Research Infrastructure' action of the European Community.

## References

[1] P.A. Franken, A.E. Hill, C.W. Oeters, G. Weinreich, Phys. Rev. Lett.**7** (1961) 118

[2] F. Keilmann, Infrared Phys. **31** (1991) 373

[3] W.L. Faust, C.H. Henry, Phys. Rev. Lett. **17** (1966) 1265; W.L. Faust, C.H. Henry, R.H. Eick, Phys. Rev. **173** (1968) 781

[4] G.D. Boyd, T.J. Bridges, M.A. Pollack, E.H. Turner, Phys. Rev. Lett. **26** (1971) 387

[5] W.D. Johnston, I.P. Kaminov, Phys. Rev. **188** (1969) 1209

[6] A. Mayer, F. Keilmann, Phys. Rev B **33**, (1986) 6954

[7] M. Barmentlo, G.W. 't Hooft, E.R. Eliel, E.W.M. van der Ham, Q.H.F. Vrehen, A.F.G. van der Meer, P.W. van Amersfoort, Phys. Rev. A **50** (1994) R14

[8] R. Köhler, A. Tredicucci, F. Beltram, H.E. Beere, E.H. Linfield, A.G. Davies, D.A. Ritchie, R.C. Iotti, F. Rossi, Nature **417** (2002) 156

[9] T. Dekorsy, V.A. Yakovlev, W. Seidel, M. Helm, F. Keilmann, Phys. Rev. Lett. **90** (2003) 055508

[10] J.J. Wynne, N. Bloembergen, Phys. Rev. **188** (1969) 1211

[11] J.H. McFee, G.D. Boyd, P.H. Schmidt, Appl. Phys. Lett. **17** (1970) 57

[12] M.M. Choy, R.L. Byer, Phys. Rev. B **14** (1976) 1693

[13] C.C. Shih, A. Yariv, J. Phys. C **15** (1982) 825

[14] A. Pinczuk, E. Burstein, in Light Scattering in Solids I, Ed. M. Cardona, Topics in Appl. Phys. **8**, 2nd Ed. (Springer, Berlin, 1983), pp.23-78

[15] C. Flytzanis, Phys. Rev. B **6** (1972) 1264

[16] C. Flytzanis, Phys. Rev. Lett. **29** (1972) 772

[17] S. Go, H. Bilz, M. Cardona, Phys. Rev. Lett. **34** (1975) 580

[18] N. Bloembergen, P.S. Pershan, Phys. Rev. B **128** (1962) 606

# Origin of Anomalous Temperature Dependence of Highly Efficient Silicon Light-Emitting p-n Diodes Prepared by Ion Implantation

J.M. Sun, T. Dekorsy, W. Skorupa, B. Schmidt and M. Helm

The implementation of silicon-based optoelectronics requires the realization of light emitters, waveguides and photodiodes compatible with standard silicon processing technology [1]. Light emitters, such as silicon nanoclusters, Er-doped Si-rich $SiO_2$, SiGe quantum dots, and silicon p-n junctions are presently considered as potential light sources [2]. The latter ones are especially attractive, since they are fully compatible with silicon ultra-large-scale integration technology including low operation voltages. Although bulk silicon, being an indirect semiconductor with inefficient radiative recombination, has been neglected for this purpose for a long time, significant improvements in the electroluminescence (EL) efficiency from bulk silicon p-n diodes have been reported recently [3,4]. The main concept for improving the light emission from silicon is based on a decrease of non-radiative decay channels possibly with carrier confinement in the active region of the device. Green et al. [3] employed surface texturing in combination with efficient surface passivation of high-purity float-zone silicon to improve the light extraction from the p-n junction. Ng *et al.* [4] prepared silicon light-emitting diodes by high boron-dose implantation for the p-type doping in silicon p-n junctions. They explained the increased EL efficiency by carrier confinement introduced by dislocation loops formed during implantation, where the strain-induced potential at dislocations loops prevents carriers from diffusing to non-radiative channels, thus leading to a strong band-edge electron-hole recombination. Similar high EL efficiency was also reported in silicon $p^+$-n junctions prepared by thermal diffusion of high boron concentrations ($3\times10^{19}$ $cm^{-3}$) in the surface layer [5]. All these p-n diodes with highly boron-doped surface layers have in common the interesting feature of an anomalous increase in EL efficiency with temperature, which is in stark contrast to the conventional behaviour of photoluminescence from bulk silicon. A study of this anomalous temperature dependence is essential for the understanding of the enhancement of the EL with increased boron doses. However, up to now no detailed experimental investigation has been reported for clarifying the origin of the anomalous temperature dependence and its relation to the high EL efficiency in such p-n diodes. In a previous study of low temperature EL spectra of silicon p-n diodes we found two luminescence peaks with maxima around 1.05 eV and 0.95 eV from excitons bound to traps which are introduced by the high-dose boron implantation and the subsequent annealing [6]. A more detailed study indicates that these peaks can be explained by recombination of spatially indirect excitons (with electrons and holes localized in spatially separated potential minima) which are formed by a locally increased boron concentration in combination with strain-free or highly strained environments surrounding dislocations [7,8]. The strong trapping and de-trapping of excitons bound to these traps can strongly influence the conductivity via the free carrier concentration and contribute to an S-type current bistability at low temperature [6]. Here we concentrate on the dependence of the EL on the boron implantation dose and the lattice temperature [9]. The strong correlation between the temperature dependence of the EL intensity from the band-edge recombination and from bound excitons provides strong evidence that the release of electron-hole pairs from the excitonic traps to the valence and conduction band play an important role in the anomalous temperature dependence and high efficiency of the diodes. Efficient room-temperature (RT) EL with power efficiency up to 0.12 % is observed from such silicon p-n diodes with further improvements to be expected.

The silicon p-n diodes were prepared by boron implantation into (001) oriented Sb-doped n-type (0.1 Ωcm) silicon substrates at a tilt angle of $7^o$ through a 50 nm thermally grown $SiO_2$ layer. Boron doses between $2\times10^{13}$ and $3\times10^{17}$ $cm^{-2}$ were implanted at an energy of 25 keV. All samples were subsequently furnace annealed at 1050 °C for 20 minutes and processed into 1 mm diameter diodes with aluminium metallic ring contacts on top. For low-temperature EL studies, the diodes were mounted on the cold finger of a closed-cycle cryostat with silver paste. EL signals were recorded with a monochromator and a liquid-nitrogen cooled InGaAs detector. All EL spectra

were measured at a constant current of 50 mA supplied by a sourcemeter (Keithley 2410), with a typical forward bias of 0.85 V at RT. The absolute EL power from the diode at RT was measured using a calibrated large-area optical power meter placed in proximity to the diode. The external EL power efficiency is calculated by dividing the total EL output power from the front plus the back surface by the input electrical power.

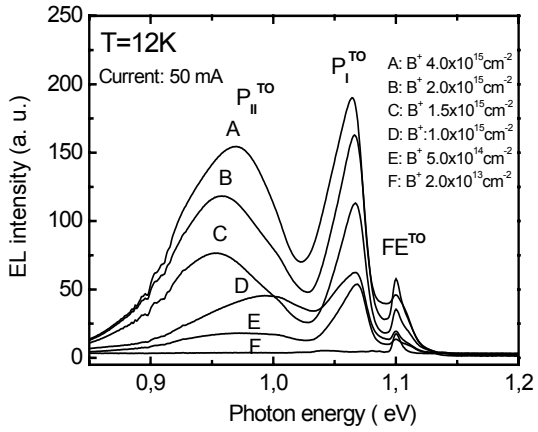


**Fig. 1:** EL spectra from silicon p-n diodes prepared by boron implantation at an energy of 25 keV and different doses as given in the figure. All samples are annealed at 1050 °C for 20 minutes. The spectra are recorded under forward bias at a current of 50 mA.

Fig. 1 shows the EL spectra at 12 K from the silicon p-n diodes prepared by boron implantation at different doses of $4\times10^{15}$ (A), $2\times10^{15}$ (B), $1.5\times10^{15}$ (C), $1\times10^{15}$ (D), $5\times10^{14}$ (E), and $2\times10^{13}$ cm$^{-2}$ (F). At implantation doses higher than $5\times10^{14}$ cm$^{-2}$, the spectra show a peak from the transverse optical (TO) phonon-assisted free exciton recombination at 1.1 eV ($FE^{TO}$) and two asymmetric broad EL peaks close to 1.05 eV and 0.95 eV from TO phonon-assisted recombination of excitons bound to traps ($P_I^{TO}$ and $P_{II}^{TO}$, respectively). At very low boron implantation doses of $2\times10^{13}$ cm$^{-2}$, no luminescence from bound excitons is observed in the EL spectrum (F). Above an implantation dose of $5\times10^{14}$ cm$^{-2}$, the bound-exciton peaks ($P_I^{TO}$, $P_{II}^{TO}$) increase strongly with increasing the boron doses up to $4\times10^{15}$ cm$^{-2}$. The photon energy of these peaks also changes with changing the boron doses. These results indicate that both peaks are strongly correlated to the traps created by high-dose boron implantation and the subsequent annealing. In Fig. 2 the dependence of the EL intensity at 12 K of the two bound-exciton peaks on the boron doses from $2\times10^{13}$ to $3\times10^{17}$ cm$^{-2}$ is plotted. It is clearly seen that their EL intensities increase strongly up to a boron dose close of 2-3 times the boron solubility limit of $1.53\times10^{20}$ cm$^{-3}$ at the annealing temperature of 1050 $^{o}$C [10] and then decrease with further increasing the boron doses. Higher boron implantation doses lead to an increased damage of the lattices structure as well as the formation of boron precipitates [11], therefore a decrease of the EL intensity is observed due to the associated creation of additional non-radiative recombination centers. The correlation in Fig. 2 of the *low-temperature* emission from the excitonic bands with the *RT EL efficiency* from band-edge recombination will be discussed later.

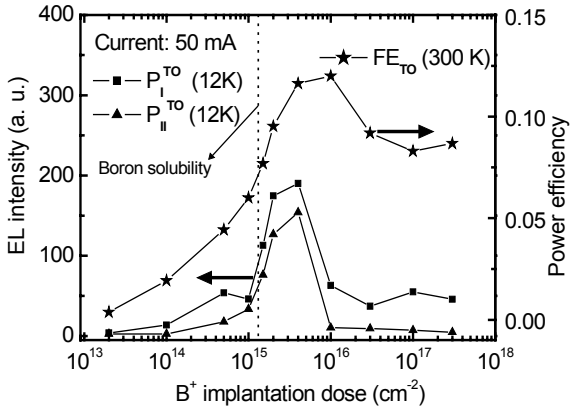


**Fig. 2:** Boron-dose dependence of the EL intensity from bound-exciton bands at 12 K (full squares and triangles) and the EL power efficiency from the band-edge recombination at RT (asterisks). The vertical line represents the boron solubility limit of $1.53\times10^{20}$ cm$^{-3}$ at the annealing temperature of 1050 °C.

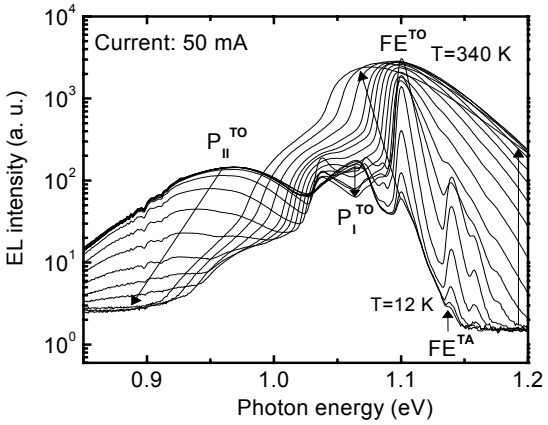


**Fig. 3:** EL spectra at different temperature from 12-340 K from sample (A) implanted with a $B^+$ dose of $4\times10^{15}$ cm$^{-2}$; the arrows indicate the change of the spectra with increasing temperature.

The temperature dependence of the EL spectra was studied at a fixed current of 50 mA for diode (A) prepared by boron implantation with a dose of $4\times10^{15}$ cm$^{-2}$, which exhibits the highest EL intensity of the bound-exciton peaks at low

temperatures. Fig. 3 shows a strong increase and broadening of the $FE^{TO}$ peak with increasing temperature. At RT, after the thermal quenching of $P_I^{TO}$ and $P_{II}^{TO}$ peaks, the spectrum resembles the typical band-edge recombination spectrum of bulk silicon. The peak height of the bound-exciton peaks $P_I^{TO}$ and $P_{II}^{TO}$ as well as the overall integrated EL intensity of the $FE^{TO}$ peak and its phonon replicas is plotted as a function of temperature in Fig. 4, where the peak height of the $P_I^{TO}$ peak is obtained by subtracting the contributions of the phonon replicas of the free electron-hole recombination. In addition, the temperature dependence of the integrated *photoluminescence* of the $FE^{TO}$ peak of the n-doped substrate is shown for comparison. The photoluminescence spectra are obtained from the substrate of the diodes under excitation with a He-Ne laser (power ~10 mW).

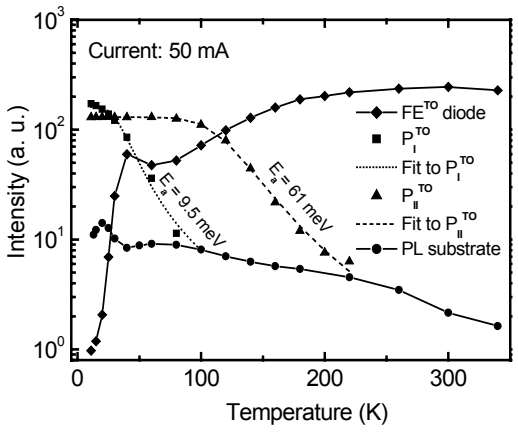


**Fig. 4:** Dependence of the EL intensity from different bands on the lattice temperature for sample (A). The dotted and dashed lines are theoretical fits to the experimental data of the bound-exciton peaks. The solid lines are guides to the eye. The temperature dependence of the photoluminescence from the band-edge recombination of n-type silicon substrate is shown for comparison. Note that the relative scale for EL and photoluminescence is arbitrary.

The $P_I^{TO}$ peak starts to decrease from 15 K and is completely thermally quenched at 80 K. The $P_{II}^{TO}$ peak starts to decrease at 80 K, and is thermally quenched at a temperature of 260 K, where the maximum intensity of the $FE^{TO}$ peaks is reached. The increase of band-edge EL intensity is in strong contrast to the temperature dependence of the PL from the n-type substrate, which exhibits no trap-related luminescence. The EL intensity of the $FE^{TO}$ peak shows a two-step increase with rising temperature in close correlation with the decrease of the two bound-exciton peaks: The first increase of the $FE^{TO}$ peak at low temperature is related to the thermal quenching of the $P_I^{TO}$ line with a characteristic activation energy of 9.5 ± 1.5 meV; the second increase is correlated to the thermal quenching of the $P_{II}^{TO}$ line with an characteristic energy of 61 ± 2 meV. The activation energies of the bound excitons to free electron-hole pairs in the continuum states of the valence and conduction bands are obtained by fitting the intensity with the expression $I=I_0/[1+g\cdot T^{3/2}exp(-E_a/kT)]$ [12], where $E_a$ is the activation energy, $I_0$ is the EL intensity at low temperature, $g\cdot T^{3/2}$ equals the capture rate of free excitons to excitonic traps times the density of effective states in the valence and conduction bands [13], and $k$ is the Boltzmann constant. This correlation indicates that the increase of the band-edge free electron-hole recombination comes from the thermal dissociation of bound excitons with increasing temperature. Our results also reflect the typical low recombination rate of the spatially indirect bound excitons in the p-n diodes, which have a recombination rate over 100 times lower than the thermal emission rate at 220 K as calculated by a rate equation model considering the transition between bound excitons and free excitons/electron-hole pairs [14].

Our interpretation about the relevance of the excitonic traps is corroborated by comparing the electroluminescence efficiency at the $FE^{TO}$ band at RT with the low-temperature emission from the bound excitons – as shown in Fig. 2 as a function of the implantation dose. The RT power efficiency of the diode shows the same strong increase as the low-temperature bound-exciton emission close to a boron concentration around three times the solubility limit of boron at the post-implantation annealing temperature of 1050 °C. This underlines the role of the excitonic traps produced by boron implantation as a source term for free electron-hole pairs at elevated temperatures: They prevent the carriers from decaying in fast non-radiative decay channels at higher temperatures, which govern the usual decreasing photoluminescence intensity as the temperature is increased.

The power efficiency of 0.12 % obtained for our diode is comparable to those reported for similar Si:B diodes [4] and also to electrically pumped Er-doped $SiO_2$ layers. The latter ones have large external quantum efficiencies of 10 %, however, considering the larger bias voltage (electric fields) of 43 V (7 MV/cm) necessary for electrical excitation of the $Er^{3+}$-ions, the external power efficiency of 0.18 % [15] is comparable to the values reported here.

In summary, efficient EL with power efficiency up to 0.12 % was observed from silicon p-n diodes prepared by boron implantation [9]. The temperature dependence of the electroluminescence from bound excitons and free electron-

hole pairs shows that excitonic traps act as a temporary storage of electron-hole pairs, which effectively enhance the band-edge radiative recombination in silicon p-n diodes by supplying free electron-hole pairs at elevated temperature.

## Acknowledgments

We would like to thank I. Winkler for the ion implantation, I. Beatus, G. Schnabel, and B. Scheumann for the diode processing.

## References

[1] A. Polman, Nature Materials **1** (2002) 10

[2] L. Pavesi, J. Phys.: Condens. Matter **15** (2003) R1169

[3] M.A. Green, J. Zhao, A. Wang, P.J. Reece, M. Gal, Nature **412** (2001) 805

[4] Wal Lek Ng, M.A. Lourenco, R.M. Gwillia, S. Ledain, G. Shao, K.P. Homewood, Nature **410** (2001) 192

[5] A.M. Emel'yanov, N.A. Sobolev, T.M. Melnikova, S. Pizzini, Semiconductors **37** (2003) 730

[6] J.M. Sun, T. Dekorsy, W. Skorupa, B. Schmidt, M. Helm, Appl. Phys. Lett. **82** (2003) 2823

[7] H. Weman, B. Monemar, G.S. Oehrlein, S.J. Jeng, Phys. Rev. B **42** (1990) 3109

[8] J.M. Sun, T. Dekorsy, W. Skorupa, B. Schmidt, A. Mücklich, M. Helm, submitted to Phys. Rev. B

[9] J.M. Sun, T. Dekorsy, W. Skorupa, B. Schmidt, M. Helm, Appl. Phys. Lett. **83** (2003) 3885

[10] S. Solmi, F. Baruffaldi, R. Canteri, J. Appl. Phys. **69** (1991) 2135

[11] S. Solmi, E. Landi, F. Baruffaldi, J. Appl. Phys. **68** (1990) 3250

[12] G. Davies, Phys. Rep. **176** (1989) 83

[13] V.V. Kveder, E.A. Steinman, S.A. Shevchenko, H.G. Grimmeiss, Phys. Rev. B **51** (1995) 10520

[14] T. Dekorsy, J.M. Sun, W. Skorupa, B. Schmidt, M. Helm, Appl. Phys. A **78** (2004) 471

[15] M.E. Castagna, S. Coffa, M. Monaco, A. Muscara', L. Caristia, S. Lorenti, A. Messina, Mat. Res. Soc. Symp. Proc. **770**, (2003) I2.1.1.

# ta-C Deposition Simulations: Film Properties and Time-Resolved Dynamics of Film Formation

H.U. Jäger and A.Yu. Belov[1]

[1] *TU Dresden, Institut für Werkstoffwissenschaft, D-01062 Dresden*

The atomic network of hydrogen-free amorphous carbon films [1] consists of three- ($sp^2$) and fourfold coordinated ($sp^3$) sites. The respective fractions of these two bonding types determine the film properties, which vary from graphite- to diamond-like as the $sp^3$ content increases. Films with a high content (80% - 90%) of tetrahedrally coordinated atoms can be deposited by means of hyperthermal carbon ion beams with energies of typically ~20 eV - 1 keV. These films are known as tetrahedral amorphous carbon (ta-C), and are expected to become significant for applications, e.g. as ultrathin coatings in magnetic storage technology [2], or as cathode material in field emission displays [3].

It is now widely accepted that the formation of ta-C films is due to an internal subsurface growth induced by the shallow carbon ion implantation. The deposition process was analyzed in terms of phenomenological models [4] such as the "subplantation models" of Lifshitz *et al*. [5] and of Robertson [6]. The film structure in these models is determined by an interplay between two processes: densification by incoming energetic ions and relaxation of density. While the ballistic part of the deposition process is now well understood, the nature of relaxation phenomena in ta-C growth still remains unclear. In particular, the strong dependence of the $sp^3$ content on substrate temperature $T_s$ is not yet fully explained. The structure of as-deposited films is known to depend critically on $T_s$. Deposition at room temperature produces films containing up to ~85% of carbon atoms with $sp^3$ hybridization. This value remains nearly constant below a transition temperature $T_c$ of ~200°C. Above $T_c$, it falls abruptly, indicating a transition from ta-C to graphitic carbon with dominating $sp^2$ bonding.

It is an attractive goal to understand the ta-C deposition process and especially its critical dependence on substrate temperature from an atomistic perspective. During the past decade, the increasing computational capabilities and the progress in developing empirical C–C atom potentials encouraged some groups to approach the problem and to perform related classical molecular-dynamics (MD) investigations [7-9].

For ta-C deposition simulations [8], we adopted a phenomenological potential [10] proposed by Brenner and modified it in a simple way in order to improve the simulation of transitions from diamond- to graphite-like carbon systems. For this purpose the C-C interaction cutoff value was increased. The ta-C film deposition was investigated at first only at a low substrate temperature (100 K). More than $10^3$ carbon atom impacts were simulated, so that the steady-state growth mode of the films was achieved. In the simulated films, the surface region, the transition region to the substrate, and the inner film region with nearly constant properties can be identified. The $sp^3$ fractions of the inner regions lie between 52 and 95% for $C^+$ ion energies of 30 - 80 eV. The intrinsic stress and the elastic properties of these films were investigated in subsequent papers [11]. Altogether the approach reproduced essential trends of experimental data on diamond-like carbon. Recently, we performed therefore a series of further, very time-consuming MD deposition simulations, using the same model. The aim was to check the approach more thoroughly under realistic process conditions, not only at a very low substrate temperature, but also at room temperature and at elevated temperatures. This allows for the effect of deposition temperature on relaxation processes during the film growth to be investigated. Films with a thickness of up to 10 nm were modeled, and the relaxation time after an ion impact was chosen relatively long (15 ps).

This report provides information about the bulk properties of the computed films; for all simulation results, see Ref. [12]. In Fig. 1, the calculated $sp^3$ fractions are plotted vs. ion energy and substrate temperature. At a low substrate temperature (100 K), ta-C structures with a high $sp^3$ content are modeled for beam energies $E_{ion} \geq 30$ eV. The simulated $sp^3$ content decreases with increasing substrate temperature. At room temperature, the $sp^3$ fractions are only in qualitative agreement with experimental data. The upper values are too low, about 65% instead of the observed values of up to 80 - 90%. The minimum energy which is required to deposite $sp^3$-rich films depends on temperature, it varies from ~25 eV at

100 K to ~35 eV at 20 °C. For higher substrate temperatures, at $E_{ion}$=40 eV, the model predicts a transition from an $sp^3$ content of (62.3±12.7)% at $T_s$=80°C to a value as low as (18.2±4.6)% at $T_s$=130°C. This sharp transition is almost in agreement with reported data and may be considered as the most essential result of the present investigations. In the experiments [1,13] the transition was found at somewhat higher temperatures, when $T_s$ exceeds a critical temperature $T_c$ of 150 - 200°C. $T_c$ decreases [13] with increasing ion energy $E_{ion}$, and equals 150°C for 120 eV deposition [1].

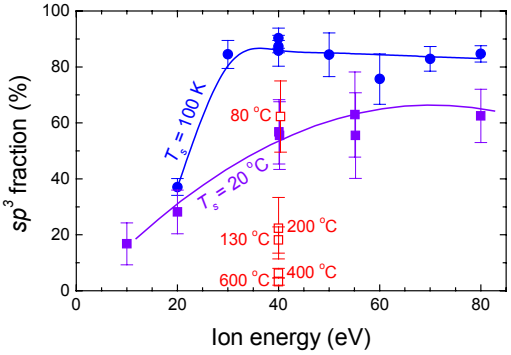


**Fig. 1:** Variation of $sp^3$ bonding in the simulated ta-C films as a function of $C^+$ ion energy $E_{ion}$ and deposition temperature $T_s$. Different symbols are used in order to characterize temperature of the substrate: $T_s$=100 K (closed circles), 20 C (closed squares), and 80-600°C (open squares). The lines are included to guide the eye.

The energetics of the simulated films can be examined by analyzing cohesive energies. Fig. 2 shows the relationship between the average potential energy per bulk atom and the fraction of fourfold coordinated atoms. The figure reveals that a graphitic film consisting of only threefold coordinated atoms ($x$=0) is predicted to have a lower energy than films with $x$>0. Pure (100%) tetrahedral amorphous carbon would be a metastable state. Fitting the data by a polynomial of second order yields an energy curve which has a maximum near medium film composition. Accepting the fit in spite of its large statistical errors, the energy barrier separating a film of 85% $sp^3$ content from the more stable graphitic forms is about 0.04 eV. Although this low value, which corresponds to a temperature of about 400 K, nicely correlates with the critical substrate temperature of $T_s$~100 °C from the deposition simulations (Fig. 1), it does not entirely explain the dependence of subsurface film growth on temperature. The question arises why the thermal stability of ta-C films against post-deposition annealing is significantly higher. During post-deposition thermal annealing in ultrahigh vacuum [14] an $sp^3$ content of 87% decreases only slightly up to 1100°C. Thus, bulk ta-C must be separated from graphitic carbon by another barrier, being much higher than ~0.04 eV. Recently we performed adequate MD annealing simulations [15] for ta-C, using the same empirical potential as in this paper, and reproduced the high thermal stability. The paradox between high graphitization temperature during annealing and low transition temperature in ion beam deposition can be resolved by the nonlocal character of the $sp^3$ to $sp^2$ conversion, being represented by a collective reconstruction of an amorphous network involving many atoms.

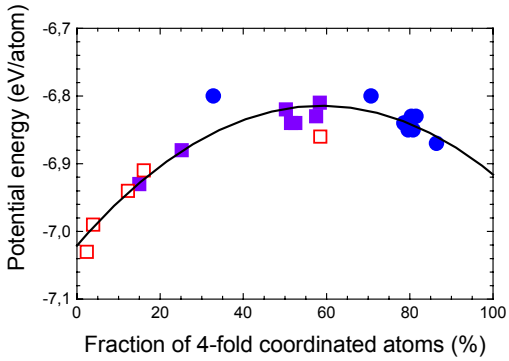


**Fig. 2:** Energetics predicted for the inner film regions. The average potential energy per atom at a film temperature of 0 K is plotted versus the fraction of fourfold coordinated atoms; for the types of symbols, see Fig. 1. The solid line is the result of a polynomial fit of second order. The inner film regions contain 3-, 4- and 5-fold coordinated atoms. The fractions of the fivefold coordinated atoms vary here between 0.8 and 6.3%, and the tendency is that this admixture increases with the fraction of fourfold coordinated atoms, i.e. with the x-axis values.

In the following we focus on the two deposition simulations performed for $E_{ion}$=40 eV at substrate temperatures $T_s$ of 80 and 130 °C, which is just below and above the transition temperature $T_c$ , respectively (Fig. 1). For a series of successive atom impacts the movement of the atoms in these two simulation runs was recorded in great detail. Fig. 3 presents, as a function of time and averaged over 500 ion impacts, the increase in the number of highly coordinated atoms. In addition, the instant temperature of the atoms coupled to the heat bath is plotted. Zero time is defined by the moment when the depth difference between the incident atom and the top surface atom is equal to the outer cutoff of the potential.

First the evolution of temperature is considered. The temperature given in Fig. 3(a) was derived from the kinetic energies of the atoms, which are outside a cylinder surrounding the “ion track" and are coupled to the heat bath. Due to energy flux out of the impact zone, this temperature begins to rise after 30 fs, on average. The peak

temperature occurs after ~400 fs. In case of dissipating the 40-eV incident energy to the kinetic and potential energies of all active atoms (about 1000), a maximum temperature increase by 0.02 eV or 200°C would be expected. However, because of permanent cooling the actual rise in temperature is only ~80°C. The model system cools again down to the substrate temperature $T_s$ in typically 5 ps. After thermalization, fluctuations in the temperature of the system may appear if temperature-driven relaxation processes consume or release kinetic energy.

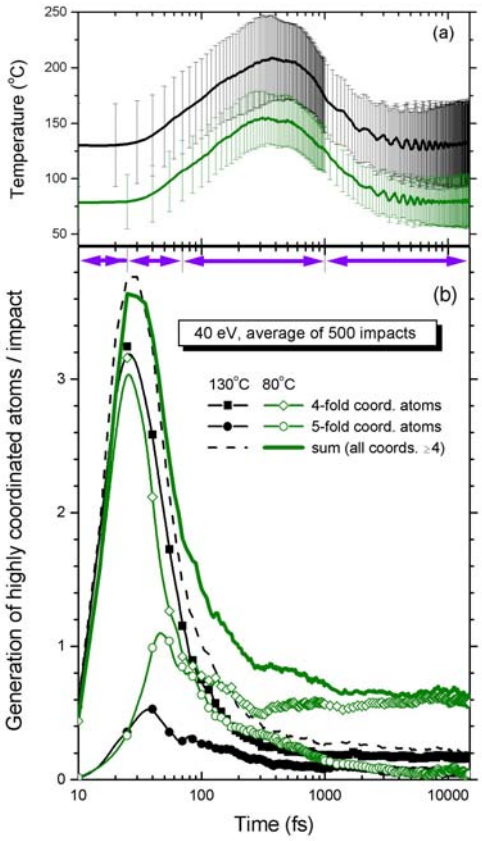


**Fig. 3:** The formation of highly coordinated atoms after a 40 eV $C^+$ ion impact, shown for the two substrate temperatures $T_s$=80 and 130°C being just below and above the critical temperature for ta-C film simulation (compare Fig. 1). The Fig. presents (a) the temperature of the atoms coupled to the heat bath and (b) the increase in the number of four- and fivefold coordinated atoms as a function of time. The quantities were calculated by averaging over 500 successive events during steady-state film growth. The horizontal arrows mark time periods as discussed in the text.

The presentation in Fig. 3(b) provides information on the chronological order of the film formation processes. To simplify the explanation of the specific curves, four time regimes are marked by horizontal arrows, which are discussed in the following.

Subplantation ($t$ = 0 - 25 fs)

The curves reflect the increasing number of atoms in the first neighbors sphere of the projectile when it is entering the target. The recoils begin just to move, changes in their bonds to target atoms do not dominate yet the plot. If the incident atom is forced initially between three atoms being before 1× twofold and 2× threefold coordinated ones, then 3 new highly coordinated atoms are generated. The peaks of the curves at 25 fs are somewhat higher than 3, since there are contributions where the twofold coordinated atom mentioned is replaced by a higher coordinated atom. In the course of these 25 fs the projectile loses half of its kinetic energy, on average.

Stopping and temperature-independent relaxations ($t$ = 25 - 70 fs)

The incident atom comes almost to rest during this period, it is decelerated to an energy of about 1 eV. The instant temperature of the atoms coupled to the heat bath begins to rise. Fivefold coordinated atoms are (transiently) produced. The coordinations of the slowed down collision cascade atoms are significantly controlled by the potential energy contour . Only in this way one can explain that the total production of highly coordinated atoms per incidence decreases and reaches values near unity. An ultimate value of unity would be realized in case of steady-state growth of a purely $sp^3$-bonded film. In our example, the average values at 70 fs amount to 1.8 and 1.5 new highly coordinated atoms for substrate temperatures of 80 and 130 °C, respectively. In a first approximation, these two values can be considered to be equal to each other, and thus to be independent on temperature.

Temperature-dependent relaxation ($t$ = 70 - 1000 fs)

At the beginning of this period the simulation cell temperature continues to rise. The maximum value is achieved, thereafter the temperature decreases. The film relaxation is now governed by temperature. For the higher substrate temperature ($T_s$=130°C), the numbers of new four- and fivefold coordinated atoms decrease continuously, and at $t$ =1000 fs a total fraction of only 0.26 new highly coordinated atoms exists per event. For the lower substrate temperature ($T_s$=80°C), the number of new fivefold coordinated atoms decreases too, even to a larger degree. But for $t$ >300 fs, an essential part of the vanishing fivefold coordinated atoms relaxes to fourfold coordinated ones, and thus the fraction of new fourfold coordinated atoms increases again.

Temperature-driven stabilization ($t > 1$ ps)

For times $t > 1$ ps the relaxation processes continue and act in a similar way. Because of the falling cell temperatures, bond breaks or formations happen less frequently. For longer times (~9 - 15 ps), before the next beam atom impinges on the sample, statistical fluctuations begin to dominate all curves plotted in Fig. 3, the averaged derivatives are nearly zero.

Fig. 3 explains why the theoretical critical temperature of $T_c$ ~100°C for 40 eV could be smaller than in experiments. In the period when the most important temperature-dependent relaxation processes are predicted to occur ($t$ =70 - 1000 fs), the total temperature of the part of the simulation cell which is coupled to the heat bath exceeds the pre-defined substrate temperature $T_s$. A more accurate reproduction of $T_c$ would require larger lateral MD cell dimensions to ensure better modeling of thermostatting.

The time scales of the physical processes involved in ta-C film formation were estimated more than one decade ago, when the ideas of subplantation have been established. According to Lifshitz *et al*. [5,16,17], three time scales characterizing the evolution of the film can be expected and described as follows: (i) a collisional stage, in which the projectiles transfer their kinetic energy to the target atoms (100 fs); (ii) a thermalization stage, in which the energetic atoms participating in the collision cascade dissipate their excess energy to lattice (less than 10 ps); (iii) a long-term relaxation stage (more than 100 ps), in which the final structure of the material is determined. The second stage, which is poorly understood, is often discussed in “thermal spike" notations. The third stage is assumed to be governed by thermally activated processes such as diffusion of interstitials and vacancies, phase transformations and chemical reactions [16].

Fig. 3 reveals that the atomistic simulations provide similar time intervals only for the collisional regime and for thermalization of the cascade region. New results are the high degree of structure relaxation during the initial collisional regime, and the extensive formation of the final film properties, which depend on temperature, at times as small as ~1 ps. For the relaxation during the collisional and thermalization stages, the many-body effects are predicted to be more important than it was previously expected.

## References


[1] Y. Lifshitz, Diam. Relat. Mater. **8** (1999) 1659, and references therein

[2] J. Robertson, Thin Solid Films **383** (2001) 81

[3] W.I. Milne, A. Ilie, J.B. Cui, A. Ferrari, J. Robertson, Diam. Relat. Mater. **10** (2001) 260

[4] H. Hofsäss, H. Feldermann, R. Merk, M. Sebastian, C. Ronning, Appl. Phys. A **66** (1998) 153, and references cited therein in section II.

[5] Y. Lifshitz, S.R. Kasi, J.W. Rabalais, Phys. Rev. Lett. **62** (1989) 1290

[6] J. Robertson, Diam. Relat. Mater. **2** (1993) 984

[7] H.-P. Kaukonen, R.M. Nieminen, Phys. Rev. Lett. **68** (1992) 620; M. Kaukonen, R.M. Nieminen, Phys. Rev. B **61** (2000) 2806

[8] H.U. Jäger, K. Albe, J. Appl. Phys. **88** (2000) 1129

[9] N.A. Marks, N.C. Cooper, D.R. McKenzie, D.G. McCulloch, P. Bath, S.P. Russo, Phys. Rev. B **65** (2002) 075411; N. Marks, J. Phys.: Condens. Matter **14** (2002) 2901

[10] D.W. Brenner, Phys. Rev. B **42** (1990) 9458; **46** (1992) 1948

[11] A.Yu. Belov, H.U. Jäger, Mater. Res. Soc. Symp. Proc. **648** (2001) P6.53; Comp. Mater. Sci. **24** (2002) 154; Surf. Coat. Technol. **151-152** (2002) 128

[12] H.U. Jäger, A.Yu. Belov, Phys. Rev. B **68** (2003) 024201

[13] M. Chhowalla, J. Robertson, C.W. Chen, S.R.P. Silva, C.A. Davis, G.A.J. Amaratunga, W.I. Milne, J. Appl. Phys. **81** (1997) 139

[14] A.C. Ferrari, B. Kleinsorge, N.A. Morrison, A. Hart, V. Stolojan, J. Robertson, J. Appl. Phys. **85** (1999) 7191

[15] A.Yu. Belov, H.U. Jäger, Nucl. Instr. Meth. B **202** (2003) 242

[16] Y. Lifshitz, S.R. Kasi, J.W. Rabalais, W. Eckstein, Phys. Rev. B **41** (1990) 10468

[17] Y. Lifshitz, G.D. Lempert, E. Grossmann, I. Avigal, C. Uzan-Saguy, R. Kalish, J. Kulik, D. Marton, J.W. Rabalais, Diam. Relat. Mater. **4** (1995) 318

# Ordering Intermetallic Alloys by Ion Irradiation

K.-H. Heinig, H. Bernas[1], J.-Ph. Attane[2], D. Halley[2], D. Ravelosona[3], A. Marty[2], P. Auric[2], C. Chappert[3] and Y. Samson[2]

[1] *CSNSM, CNRS-IN2P3, Orsay, France;*
[2] *CEA Grenoble, DRFMC, 38054 Grenoble, France;*
[3] *Institut d'Electronique Fondamentale, CNRS–Universite' Paris XI, 91405 Orsay, France*

Atomic collisions in solids are often associated with the concept of disorder. In fact, the mobility induced in alloys by ion irradiation at appropriate temperatures can produce a wealth of phases [1] which may (or not) be related to the equilibrium phase diagram. Research on such ''driven alloys'' [2] is quite active. The possibility of irradiation-induced ordering was conjectured with impressive insight by Néel [3], and then forgotten. Recently, it was demonstrated that irradiation may even induce chemical order in intermetallic alloys [4,5]: significant structural and magnetic order was obtained and controlled in FePt by postgrowth He ion irradiation at ~570 K, well below the ordering temperature. The chosen examples were the ferromagnetic $L1_0$-structure alloys FePt and FePd, where chemical order corresponds to a layered structure with alternating Fe and Pt(Pd) planes along the *c* axis of a tetragonal structure. Their very large magnetic anisotropy energy makes these alloy films excellent candidates for future magnetic media [6], if only uniaxial ordering with the easy magnetic axis parallel (or perpendicular) to the surface may be achieved. Whereas codeposited films order at growth temperatures (≥700 K for FePt [7], ~650 K for FePd [8]) which are prohibitive [9] for media processing, it was shown that an ion irradiation process [10] operating at the more favorable temperature [6] of ~550 K on chemically disordered FePt films could drive a transition to *L*10 order. However, the attempts to establish a relation between the sample's preirradiation short range order (SRO) and postirradiation long-range order (LRO) led [5] to an incorrect interpretation. Here we present kinetic Monte Carlo simulations of the irradiation-induced ordering, based on new experiments with films grown by a ''layer-by-layer'' technique [11] which produces an anisotropy bias in the film plane. This combination allows us to prove that the presence of *directional short range order* (DSRO) in the preirradiated sample provides the basis for a mechanism by which practically complete ordering perpendicular to the film plane may be obtained by ion irradiation in FePd(Pt). We expect this novel approach to prove valid for other layered-structure intermetallics, thereby leading to applications in surface technology.

The ''layer-by-layer'' FePd(Pt) films were obtained [11] by masking the Fe or Pd(Pt) atomic fluxes in a molecular beam epitaxy system, growing a biatomic period multilayer (typically 10–50 nm thick) of alternating pure Fe and pure Pd(Pt) atomic planes on a MgO (001) substrate at 300 K covered by a 3 nm Cr seed layer and a 60 nm (001) Pd(Pt) buffer layer. Oxidation was avoided by a 2 nm capping layer.

Three requirements were satisfied by the irradiating beam: small energy transfers, minimizing recoil displacements, a low collision cross section in order to avoid defect interactions, sufficient beam energy to ensure that ions stopped well inside the substrate. Using He ions at energies around 30–130 keV [12], recoils are limited [13] to one (or rarely two) atomic distance(s). The number of displaced atoms per incoming ion and depth in the alloy is ~ $5\times10^{-2}$ $nm^{-1}$, and all He ions stop in the substrate below the deposited layers. For the film thicknesses used here, about one Frenkel (associated interstitial and vacancy) pair is thus introduced in the entire film per incident ion. Over half of these pairs recombine athermally [14]; a small fraction may lead to antisite defect formation in the ordered phase. Pairs also recombine thermally, but due to our thin film geometry most (very mobile) interstitials disappear at surfaces. Thus, about 10% of the initial vacancies survive (interstitials will henceforth be neglected). At temperatures where atomic movements are limited, atomic site exchange processes in a crystal are normally suppressed by the high energy barriers. Introducing mobile vacancies by irradiation allows successive pairwise exchanges of atoms that are determined only by the vacancy jump probability. The latter in turn depends exponentially on the ratio of the Fe-Fe, *M*-*M*, and Fe-*M* binding energies to $kT$ (where $M$ − Pd or Pt). The system then explores the nonequilibrium paths towards the lower energy configurations corresponding to chemical order. X-ray diffraction intensities of the (001) and (003) superstructure

peaks identify the variant of the $L1_0$ ordered structure with the quadratic *c* axis perpendicular to the film surface. Integrating these peaks and the fundamental (002) and (004) peaks, we calculated [11] the LRO parameter *S* for the FePd(Pt) films. We define $S = |n_{Fe} - n_{Pd}|$, where $n_{Fe(Pd)}$ is the site occupancy by one of the elements on the Fe or Pd sublattice. Thus *S* ranges from zero (disordered film) to unity (perfectly ordered film). The initial LRO was weak, typically $S$=0.1. Polarized extended X-ray-absorption fine structure spectroscopy measurements [11] revealed that this did not preclude a high degree of DSRO and significant in-plane homocoordination. Our films were then irradiated at temperatures ranging from 293 to 573 K with 130 keV He ions at a fluence of $2.0\times10^{16}$ ions/cm$^2$. $L1_0$ long-range ordering (up to $S \sim 0.65$) was obtained after irradiation at 573 K (partially masked samples confirmed that heating alone had no effect). This irradiation led [5] to a rotation of the easy magnetization axis from in plane to out of plane. The quality factor $Q = K_u/[(1/2)\mu_0 M_s^2]$ that compares the uniaxial anisotropy $K_u$ to the shape anisotropy may be derived from the in-plane and out-of-plane hysteresis loops. For FePd (with $M_s$=1050 emu cm$^{-3}$, bulk value of $K_u=7\times10^6$ emu cm$^{-3}$), it increased from 0.76 (easy axis in plane) to $1.5 \pm 0.1$ (easy axis out of plane) after irradiation at 473 or 523 K; the perpendicular saturation and nucleation fields are both correspondingly reduced. For FePt layers (with $M_s$ = 1070 emu cm$^{-3}$ ), *Q* increased from 1.9 (as grown) to ~3.2 after irradiation at 573 K [the bulk value of $K_u$(FePt) = $7\times10^7$ emu cm$^{-3}$ would lead [15] to *Q* close to 6]. Note that the ordering temperature is higher because Pt mobility and wetting are lower than those of Pd. The perpendicular magnetic remanence was also strongly enhanced (up to 100%) upon irradiation. Although both parameters increased under irradiation, there was no simple relation between *Q* and *S*. Moreover, *Q* and *S* were *not* irradiation enhanced in codeposited films, where the initial SRO [11] is weaker. Because the magnetic anisotropy (due to the spin-orbit interaction) is primarily sensitive to changes in the local environment around the magnetic atoms, we have probed the effect of local order on the anisotropy via Mössbauer spectroscopy.

Kinetic lattice Monte Carlo (KLMC) simulations demonstrate the influence of pairwise interactions and of the initial DSRO on irradiation-induced ordering. They were performed for FePd in a 256×64×64 atom box, comparable to the actual film thickness, on an fcc lattice with an equiatomic average composition. In order to simplify KLMC calculations, the true $L1_0$ tetragonal structure was not introduced. Atomic size effects are thus neglected, but since the corresponding energies are much smaller than the ordering energy, this does not affect our conclusions regarding ordering. As mentioned, the kinetics are entirely due to vacancy motion. The film being thin, the Frenkel pair production rate being very low, and the ion flux being weak, vacancies act one by one − their activation energy and diffusion constant play no role and do not affect ordering thermodynamics [18]: the ordering rate depends only on their allowing pairwise exchanges. Energy barriers between Fe and Pd atoms were deduced [19] from the element's cohesive energies: the bond strength values used here were 0.70 eV (Fe-Fe), 0.65 eV (Pd-Pd), and 0.78 eV (Fe-Pd). In the absence of a measured value for FePd, we used the fcc($A1$)→$L1_0$ ordering enthalpy of FePt [20] as an upper limit. Boundary conditions were periodic in the horizontal plane. Layers of pure Pd were introduced above and below the FePd layer to account for the buffer and capping layers, and the upper surface and the bottom Pd/MgO interface (which contains dislocations [7]) were sinks for diffusing vacancies. The KLMC code was described elsewhere [21]. Two cases were considered. The initial distribution of Fe and Pd atoms was either random or taken from the DSRO values of Gehanno *et al.* [11]. In the latter, starting from a central Fe atom the probabilities of finding a Fe (Pd) atom in the plane are 0.82 (0.18), and out of the plane they are 0.39 (0.61). Figure 1(a) shows snapshots of the ordering process in the first case (no SRO), while Fig. 1(b) shows the corresponding evolution in a film with the DSRO of our samples. We note that (1) The driving force for ordering is the energy gained by maximizing the number of Fe-Pd bonds, and this nearest-neighbour scale mechanism is the energy gained by maximizing the number of Fe-Pd bonds, and this nearest-neighbour scale mechanism is clearly effective. Directional ordering then depends on the existence and size of a pure Fe (or Pd) layer ''template.'' The main effect of the initial DSRO anisotropy is to favour ordering along the [001] variant, perpendicular to the film plane, as shown in Fig. 1(b). (For completeness, we have selected a simulation which also illustrates that a small proportion of domains with other orientations may develop.) If the DSRO is reduced as in samples prepared via codeposition or sputtering [4,5], ordering occurs along other variants [Fig. 1(a) confirms that the three variants are equally populated in the absence of SRO], leading to a lowered *Q* factor. (2) Layer defects (e.g., bilayer islands of Fe or Pd) are quickly erased under vacancy motion for the reason

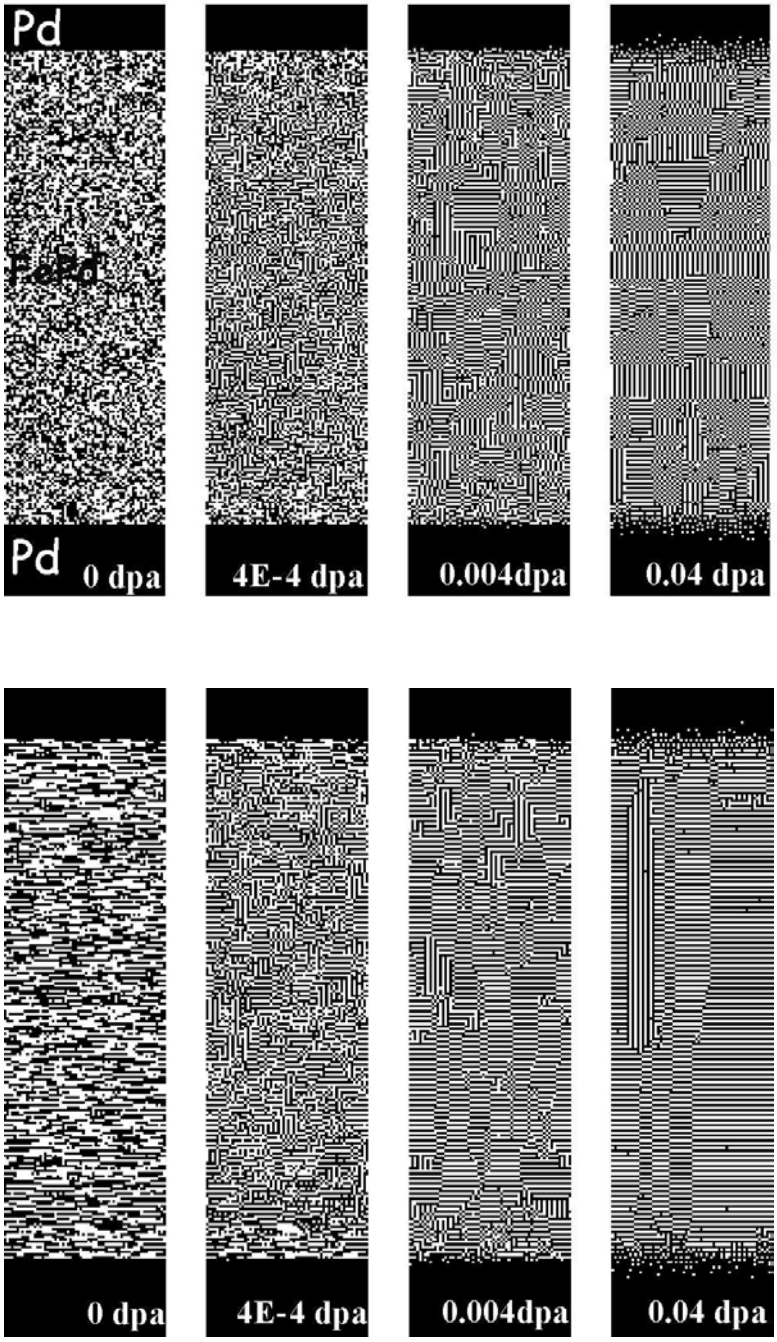


**Fig. 1:** Snapshots from KLMC simulation showing vacancy-induced ''$L1_0$'' chemical ordering during He ion irradiation at 550 K of a ~60 nm FePd film sandwiched between a Pd buffer layer and a Pd capping layer. The figures are cuts (2 atomic planes thick) through the simulation cell—for clarity, only Pd atoms are shown (in black). The (001) orientation of the $L1_0$ structure is in the $z$ direction. The number of displacements per atom dpa (which is here the number of vacancies per atom introduced into the simulation cell) is shown on each snapshot. The initial structure (first snapshot on left) is either random [no SRO, upper row] or incorporates the experimentally determined DSRO from Ref. [11] (lower row). In the case of no initial SRO (upper row), ordering occurs equally along the three possible variants (horizontal and vertical stripes correspond to the variants along the $z$ and $x$ axes, and checkerboards to the $y$ direction variant). In the case of a small deviation from initial randomness (lower row), DSRO favours ordering along the $z$-axis variant perpendicular to the film; practically complete ordering (third snapshot) corresponds to a vacancy input of about $2\times10^{15}$ cm$^{-2}$ or 0.04 displacements per atoms (0.04 dpa), in agreement with the experimental value. See comments in text.

discussed above, and site-antisite pairs are eliminated even more efficiently. (3) The {100} antiphase boundaries develop as the [001]-oriented domains grow. Their low energy (in the meV range) allows them to survive but they do not affect the magnetic anisotropy.

In summary, because He ion irradiation-induced rearrangements are on a near-neighbour scale, successive pairwise interactions lead to efficient ordering. Simulations show that ordering proceeds from the initial DSRO, via the energy gained by maximizing the number of Fe-Pd bonds. The final degree of order and the ordering rate depend on the initial DSRO. Taking advantage of the ''local'' nature (spin-orbit dependence) of the magnetic anisotropy, we manipulate the DSRO to obtain films with perpendicular anisotropy values as large as those measured in bulk FePd. Our process therefore provides a postgrowth method to orient high density magnetic media, and should also apply to nanoparticulate media whose narrow size dispersion is otherwise difficult to preserve [22] during their high-temperature $L1_0$ ordering process. More generally, by playing with competing bonding strengths and starting (where necessary) from deposited films with appropriate DSRO, ion beam ordering of intermetallics may also be envisaged as a new tool in thin film growth technology and surface property improvement.

## Acknowledgements

We thank O. Kaitasov and S. Gautrot for their technical contributions, K. Barmak for a discussion, and R. Maynard for drawing our attention to Ref. [3]. This work was partially supported by the ISARD Program (Universite´ Paris II), and the French Ministry of Research under ACI ‘‘Nanorad.’’ H. Bernas is grateful to IIM/FZ–Rossendorf for hospitality and support.

## References

[1] An early example: R.S. Nelson, J.A. Hudson, D.J. Mazey, J. Nucl. Mater. **44** (1972) 318

[2] G. Martin, P. Bellon, Solid State Phys. **50** (1997) 189

[3] J. Paulevé, D. Dautreppe, J. Laugier, L. Néel, C.R. Acad. Sci. (Paris) **254** (1962) 965

[4] D. Ravelosona, C. Chappert, V. Mathet, H. Bernas, Appl. Phys. Lett. **76** (2000) 236

[5] D. Ravelosona, C. Chappert, H. Bernas, D. Halley, Y. Samson, A. Marty, J. Appl. Phys. **91** (2002) 8082

[6] D. Weller, A. Moser, IEEE Trans. Magn. **36** (2000) 10

[7] R.F.C. Farrow, D. Weller, R.F. Marks, M.F. Toney, A. Cebollada, G.R. Harp, Appl. Phys. Lett. **69** (1996) 1166

[8] V. Gehanno, A. Marty, B. Gilles, Y. Samson, Phys. Rev. B **55** (1997) 12552

[9] For example,Y. Xu, J.S. Chen, J.P. Wang, Appl. Phys. Lett. **80** (2002) 3325

[10] C. Chappert, H. Bernas, J. Ferre´, V. Kottler, J.P. Jamet, Y. Chen, E. Cambril, T. Devolder, F. Rousseaux, V. Mathet, H. Launois, Science **280** (1998) 1919

[11] V. Gehanno, C. Revenant-Brizard, A. Marty, B. Gilles, J. Appl. Phys. **84** (1998) 2316

[12] J. Chaumont, H. Bernas, F. Lalu, M. Salomé, Nucl. Instr. Meth. Phys. Res. **189** (1981) 193

[13] J. Ziegler, J. Biersack, U. Littmark, The Stopping of Ions in Matter, Pergamon Press, New York, 1985; SRIM 2000 code (http://www.srim.org).

[14] A. Seeger, D. Schumacher, W. Schilling, J. Diehl, Vacancies and Interstitials in Metals, North-Holland, Amsterdam, 1970

[15] T. Klemmer, D. Hoydick, H. Okumura, B. Zhang, W.A. Soffa, Scr. Metall. Mater. **33** (1995) 1793

[16] V. Gehanno, P. Auric, A. Marty, B. Gilles, J. Magn. Magn. Mater. **188** (1998) 310

[17] When comparing Figs. 1(a) and 1(b), note that the magnetic anisotropy’s orientation (and hence the MS line intensities) are affected by the fact that the magnetic anisotropy of FePt is 5 times larger than that of FePd.

[18] This may be contrasted with temperature-induced reordering kinetics: see, e.g., J.C. Ewert, G. Schmitz, Eur. Phys. J. B **17** (2000) 391

[19] Y. Grandjean, P. Bellon, G. Martin, Phys. Rev. B **50** (1994) 4228

[20] K. Barmak, J. Kim, S. Shell, E.B. Svedberg, J.K. Howard, Appl. Phys. Lett. **80** (2002) 4268

[21] M. Strobel, K.-H. Heinig, W. Möller, Phys. Rev. B **64** (2001) 245422

[22] S. Sun, C.B. Murray, D. Weller, L. Folks, A. Moser, Science **287** (2000) 1989

# Diamond Formation in Cubic SiC

H. Weishart, V. Heera, F. Eichhorn, W. Skorupa, B. Pécz[1] and L. Tóth[1]

[1] *Research Institute for Technical Physics and Materials Science, Budapest, Hungary*

The last decade is characterized by the search for new semiconductor materials for high temperature, high frequency and high power applications. Numerous activities concentrated on silicon carbide and diamond. The fabrication of diamond-SiC heterostructures is a new and interesting approach to novel semiconductor devices. Epitaxial growth of polycrystalline diamond onto SiC substrates has been intensively studied [1-9]. Ion Beam Synthesis (IBS) is a superior technique for producing precipitates or even complete layers of a new phase within any material. The main advantages over growth techniques are (i) no introduction of impurities because of mass separation during implantation, (ii) the possibility to synthesize almost any phase in any matrix due to the absence of thermodynamic equilibrium and (iii) the ability to synthesize nanocrystals in the host matrix. A drawback of this technique is the damage inflicted upon the host crystal by the impact processes of ion impingement. In order to reduce implantation induced damage and to facilitate *in-situ* annealing IBS should be performed at elevated temperatures [10].

Our approach of diamond formation in cubic SiC is the high-fluence implantation of C at temperatures of at least 900°C. The feasibility of diamond formation using IBS with these parameters was already demonstrated by us for 6H-SiC [11]. Here, we present the results of recent studies on diamond formation in C-implanted cubic SiC [12]. We use cubic SiC as a substrate because (i) cubic SiC, epitaxially grown on Si, is widely available and cheaper than the hexagonal polytype, and (ii) the crystal structures of diamond and 3C-SiC are similar. Therefore, a facilitated diamond formation inside SiC could be expected, which then again may lead to larger nanocrystals. The latter one is based on the assumption that the SiC lattice serves as a template for the diamond nanocrystals, which are embedded in the matrix.

Carbon was implanted with an energy of 60 keV into 956 nm thick 3C-SiC epilayers on (100) Si substrate. According to TRIM [13] calculations this ion energy creates a completely buried, 60 nm thick carbon rich layer at a mean projected range $R_p$ = 130 nm within the SiC. The two fluences under investigation, namely $1\times10^{18}$ $C^+$ $cm^{-2}$ and $3\times10^{18}$ $C^+$ $cm^{-2}$, amount to layers with mean composition of $Si_{0.22}C_{0.78}$ and $Si_{0.11}C_{0.89}$, respectively. Implantations were performed at 900, 1100 and 1200°C, respectively. The flux of C-ions was kept constant during each implantation run and varied between 4.8 µA $cm^{-2}$ ($3.0\times10^{13}$ $cm^{-2}$ $s^{-1}$) and 46 µA $cm^{-2}$ ($2.9\times10^{14}$ $cm^{-2}$ $s^{-1}$) in different experiments. The implanted samples were characterized using Raman spectroscopy in backscattering geometry with an 100 mW YAG laser at $\lambda$ = 532.14 nm. X-ray diffraction using a Siemens /

**Table 1:** Parameters for high-fluence carbon implantation into 3C-SiC and synthesized phases found in the samples.

| Temperature (°C) | Fluence ($C^+$ $cm^{-2}$) | Ion flux ($cm^{-2}$ $s^{-1}$) | Phase | Nanocrystal size (nm) | |
|---|---|---|---|---|---|
| | | | | XRD | TEM |
| 900 | $1\times10^{18}$ | $3.0\times10^{13}$ | Diamond | | 5 |
| 900 | $1\times10^{18}$ | $6.7\times10^{13}$ | Diamond | 5 | |
| 900 | $1\times10^{18}$ | $1.5\times10^{14}$ | Graphite | | 10 |
| 1100 | $1\times10^{18}$ | $1.4\times10^{14}$ | Diamond | | 4.5 - 6.5 |
| 1100 | $1\times10^{18}$ | $2.9\times10^{14}$ | Diamond | 5 | 2.5 - 5.5 |
| 1100 | $3\times10^{18}$ | $1.4\times10^{14}$ | Diamond | 7 | 2.5 - 20 |
| 1200 | $1\times10^{18}$ | $1.5\times10^{14}$ | Diamond | | 5 - 10 |

Bruker-AXS X-ray diffractometer, type D5005 with Eulerian cradle, and Cu-Kα radiation ($\lambda$ = 0.15406 nm) helped to characterize quality and quantity of crystalline phases. Additionally, phase formation was investigated by cross-sectional transmission electron microscopy (XTEM). Cross sectional specimens were prepared by ion milling. Conventional electron microscopy was done using a Philips CM20 electron microscope at 200 kV, while high-resolution images were taken in a JEOL 3010 microscope at 300 kV.

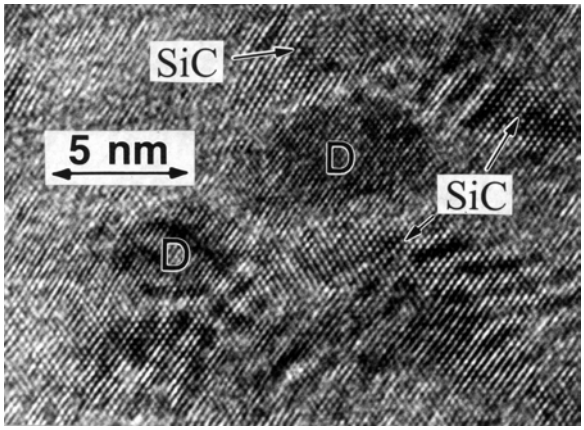


**Fig. 1:** High resolution image of a 3C-SiC layer implanted at 900°C with $C^+$ ions to a total fluence of $1x10^{18}$ $cm^{-2}$ at low flux ($3.0x10^{13}$ $cm^{-2}$ $s^{-1}$). Two of the formed diamond grains are marked by the letter D.

The complete list of implantation parameters and synthesized nanocrystalline phases is given in Table 1. The samples implanted at 900°C unambiguously show the influence of flux. Fig. 1 shows a XTEM micrograph of the sample implanted with carbon at a low flux of 4.8 μA $cm^{-2}$ ($3.0\times10^{13}$ $cm^{-2}$ $s^{-1}$). Small precipitates of diamond (marked with D) within the SiC-matrix can be seen. All the diamond grains synthesized in this way are epitaxial to the host cubic SiC. When increasing the flux to 24 μA $cm^{-2}$ ($1.5\times10^{14}$ $cm^{-2}$ $s^{-1}$), however, only graphite can be found in the implanted zone.

This flux effect also shows a dependence on implantation temperature. When samples were implanted at 1100°C or 1200°C, diamond grains were synthesized at the high flux ($1.4\times10^{14}$ $cm^{-2}$ $s^{-1}$) as well. Fig. 2 shows an example of implantation at 1200°C. The diffraction spots of diamond in the SAED pattern of Fig. 3 are a good indication that large amounts of diamond have been formed. The typical size of the diamond grains is 5-10 nm, as determined on dark field images.

X-ray diffraction confirms the formation of diamond in the samples implanted at 90°C at a flux of $6.7\times10^{13}$ $cm^{-2}$ $s^{-1}$ and at 1100°C with fluxes of $1.4\times10^{14}$ $cm^{-2}$ $s^{-1}$ and $2.9\times10^{14}$ $cm^{-2}$ $s^{-1}$, respectively. Fig. 4 shows a radial scan along the <111>-direction. The diamond nanocrystals are epitaxially oriented within the 3C-SiC matrix. Strain within the diamond grains causes a slight shift of the diamond peaks with respect to the literature value. No signals due to graphitic phases are found in the XRD spectra. A more detailed analysis of the diamond peaks from the radial as well as the angular scan shows that the amount of synthesized crystalline diamond with (111) texture in the sample implanted at 1100°C to a fluence of $2.9\times10^{18}$ $C^+$ $cm^{-2}$ is by 25% higher than in the samples implanted to a fluence of $1\times10^{18}$ $C^+$ $cm^{-2}$. Assuming that the broadening of the peak from the

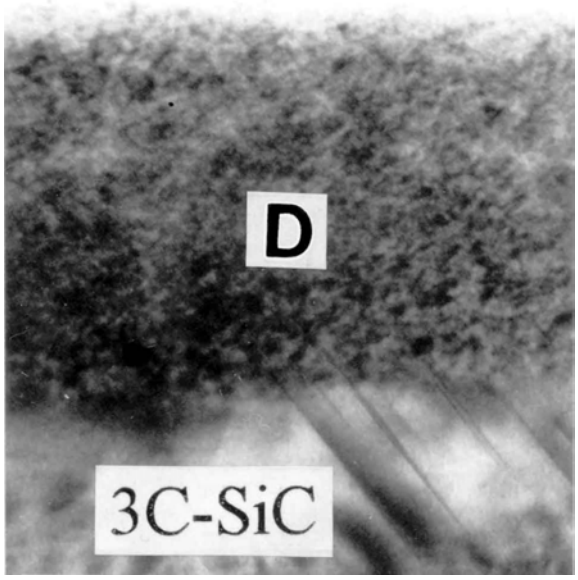


**Fig. 2:** Cross sectional image of a SiC layer implanted at 1200°C with high flux ($1.5\times10^{14}$ $cm^{-2}$ $s^{-1}$) to a total fluence of $1\times10^{18}$ $cm^{-2}$. The letter D indicates a region where diamond grains were formed inside the cubic SiC.

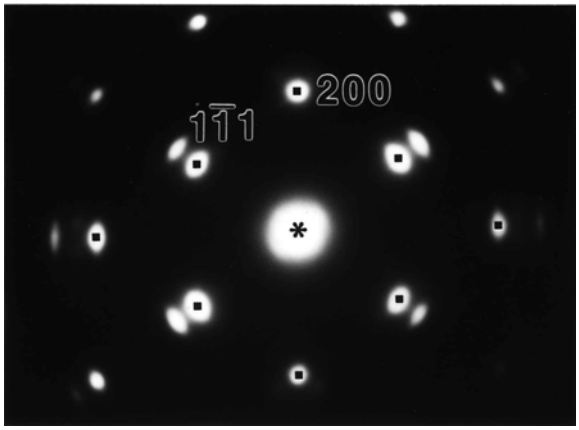


**Fig. 3:** Selected area electron diffraction (SAED) pattern taken from the zone D of Fig. 2, showing that diamond grains formed epitaxially to SiC. The outer reflections belong to diamond, while the stronger, inner reflections of each pair (indicated by small dark dots) belong to 3C-SiC.

radial scan is determined only by the crystallite size we get an average size of $5.4 \pm 0.2$ nm and $6.6 \pm 0.2$ nm for 1 and $3\times10^{18}$ $C^+$ $cm^{-2}$, respectively. The mosaicity, i.e. the orientation fluctuation of the nanocrystals within the SiC matrix, is determined from the full width half maximum of the angular scans. For the high fluence implant we find a value of approximately 5°, which is about a factor of 2 higher than for the samples implanted to $1\times10^{18}$ $C^+$ $cm^{-2}$.

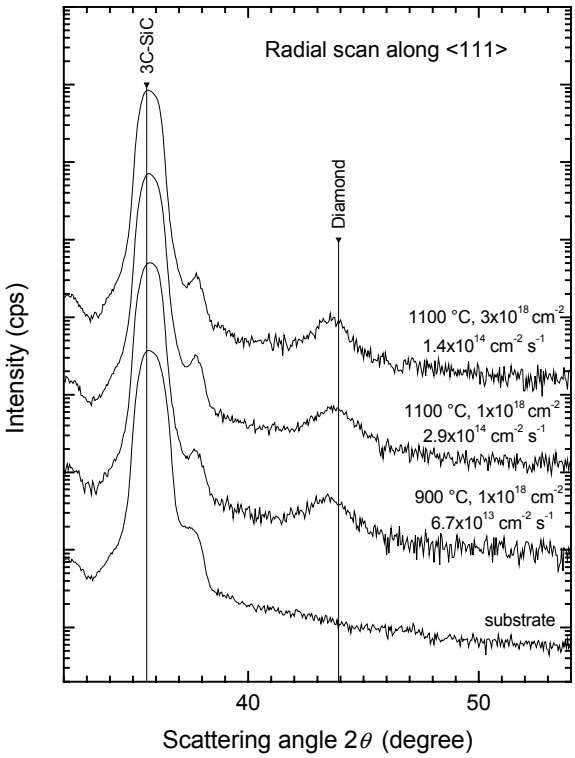


**Fig. 4:** X-ray diffraction radial scan along <111> of 3C-SiC, which was implanted with C. All C-implanted samples show a distinct diamond peak. The scattering angles of diamond and cubic SiC (111) are denoted by a line.

The explanation for the increase in amount of crystalline, epitaxial diamond by only 25% when the C-fluence is increased by a factor of 3 may be extracted from the Raman spectra, depicted in Fig. 5. The appearance of a distinct D- (1360 $cm^{-1}$) and G-peak (1600 $cm^{-1}$) proves the presence of $sp^2$ bonds (disordered graphite). The diamond signature expected at 1332 $cm^{-1}$ is not visible in the spectra, since the intrinsic Raman intensity of graphite is 50 times that of the diamond [14] and, additionally, graphitic inclusions reduce the light penetration into the substrate due to strong extinction. The clearest D- and G-peaks, however, are present in the spectrum of the sample implanted to a fluence of $3\times10^{18}$ $C^+$ $cm^{-2}$. This increase in disorder means that not only the SiC but also the diamond crystallites get damaged in the course of implantation. The higher mosaicity of the diamond crystals found by XRD in the sample implanted to $3\times10^{18}$ $C^+$ $cm^{-2}$ confirms an accumulation of damage due to the higher fluence. An equilibrium between diamond formation and destruction may establish, which determines the maximum size and amount of diamond crystals that can be formed by this process.

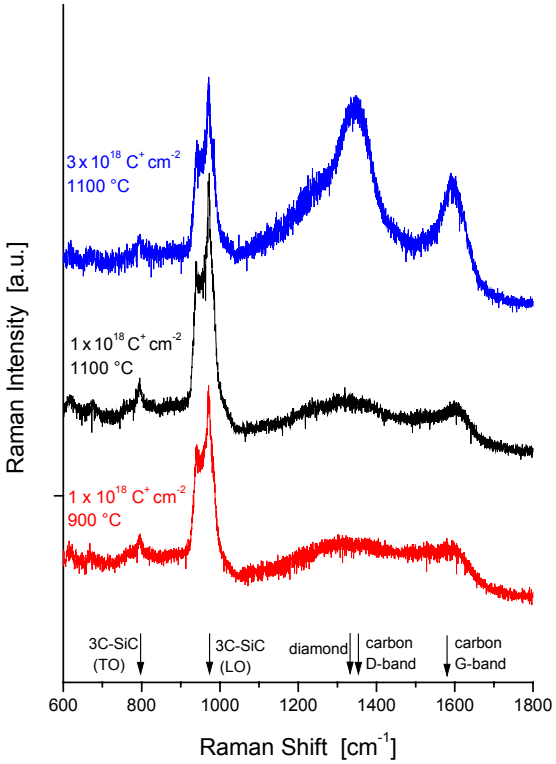


**Fig. 5:** Raman spectra of SiC samples implanted with carbon at 60 keV. The graphitic bands are visible for all spectra. The D- and G-peak become more and more pronounced with increasing implantation temperature and fluence, respectively.

The flux dependence of diamond formation inside SiC may be explained as follows. Before the implanted carbon ions come to rest they have a small amount of energy left which allows them to diffuse through the SiC host matrix until they may find a proper substitutional lattice position. Since the C-C bond is stronger than the Si-C bond, carbon atom clusters give the more stable configuration. The surrounding cubic SiC lattice structure forces the carbon to form diamond. On the other hand, the implanted carbon ions destroy the SiC by cascades of secondary ions, which create a trace of displaced atoms. Implantation at elevated temperatures allows this implantation-induced damage in SiC to anneal out. The process of recrystallization to preserve the SiC lattice structure has a certain time constant. If another ion cascade arrives before this process is complete, the

crystalline template can be damaged irreversibly. Without the external force of the lattice template, however, the thermodynamically more favourable graphite will form. Hence, growth of graphite is preferential if a too high frequency of overlapping cascades, which is the case at a high flux, prevents self annealing of the crystal structure.

The rate of self annealing and diamond formation, respectively, depend on temperature. The higher the implantation temperature, the shorter the time constant for self annealing of the lattice and the faster the process of restoring the original SiC which in turn forces the carbon atoms into a diamond lattice structure. A critical temperature $T_c$ may be defined, below which - at a given flux - graphite will form. In accordance with the well established theory for ion-beam induced epitaxial recrystallization [15,16], $T_c$ depends on the ion flux. However, more experiments are needed in order to verify this relation.

In conclusion we have shown that C implantation into cubic SiC leads to the formation of nanocrystalline diamond, which is epitaxially aligned to the SiC host matrix. The phase formation itself is strongly dependent on both, implantation temperature and flux. When implantation is performed at low temperatures and/or at high fluxes, graphite will form. Diamond-crystallites only form when implanting at high temperatures and/or low fluxes. The average size of these grains increases with fluence. In the sample implanted to a fluence of $3\times10^{18}$ $C^+$ $cm^{-2}$ XTEM revealed some diamond nanocrystals of 20 nm size, which is the largest ever reported for ion beam synthesis in SiC.

## Acknowledgements

The authors thank A. Scholz and U. Lucchesi for their technical help. This work is partly supported by the Deutsche Forschungsgemeinschaft under Contract No HE 2604/4-1.

## References

[1] W. Zhu, X.H. Wang, B.R. Stoner, G.H.M. Ma, H.S. Kong, M.W.H. Braun, J.T. Glass, Phys. Rev. B **47** (1993) 6529

[2] X. Jiang, K. Schiffmann, C.P. Klages, J. Appl. Phys. **83** (1998) 2511

[3] B.R. Stoner, J.T. Glass, Appl. Phys. Lett. **60** (1992) 698

[4] R. Kohl, C. Wild, N. Herres, P. Koidl, B.R. Stoner, J.T. Glass, Appl. Phys. Lett. **63** (1993) 1792

[5] T. Suzuki, M. Yaki, K. Shibuki, Appl. Phys. Lett. **64** (1994) 557

[6] H. Kawarada, T. Suesada, H. Nagasawa, Appl. Phys. Lett. **66** (1995) 583

[7 ] T. Suesada, H. Nagasawa, H. Kawarada, Jpn. J. Appl. Phys. 1 **34** (1995) 4898

[8] H. Kawarada, C. Wild, N. Herres, R. Locher, P. Koidl, H. Nagasawa, J. Appl. Phys. **81** (1997) 3490

[9] L. Chang, J.E. Yan, F.R. Chen, J.J. Kai, Diam. Relat. Mater. **9** (2000) 283

[10] S.X. Wang, L.M. Wang, R.C. Ewing, Phys. Rev. B **63** (2000) 024105

[11] V. Heera, W. Skorupa, B. Pécz, L. Dobos, Appl. Phys. Lett. **76** (2000) 2847

[12] B. Pécz, H. Weishart, V. Heera, L. Toth, Appl. Phys. Lett. **82** (2003) 46

[13] J.F. Ziegler, J.P. Biersack, U. Littmark, The Stopping and Range of Ions in Solids, Pergamon Press, New York, 1985, Vol. 1

[14] D.S. Knight, W.B. White, J. Mater. Res. **4** (1989) 385

[15] T. Henkel, V. Heera, R. Kögler, W. Skorupa, J. Appl. Phys. **82** (1997) 5360

[16] E. Glaser, T. Fehlhaber, B. Breger, Nucl. Instr. Meth. B **148** (1999) 426

# Competing Influence of Damage Buildup and Lattice Vibrations on Ion Range Profiles in Si

M. Posselt, M. Mäder, R. Grötzschel and M. Behar[1]

[1] *Instituto de Fisica, P.O.Box 15051, 91501-970 Porto Alegre, Brazil*

For many years it has been known that channeling effects influence the shape of ion range distributions obtained by implantation into single crystalline silicon [1-6]: The orientation of the ion beam relative to the crystal axes determines the fraction of incident ions that moves initially within axial or planar channels. However, the motion of energetic projectiles in the crystal is not only influenced by the geometrical arrangement of the lattice sites but also by thermal vibrations of the atoms and the buildup of radiation damage during implantation. This may lead both to dechanneling and rechanneling of the implanted ions. Therefore, at a given implantation energy the shape of the ion range profiles may depend on the following implantation parameters: implantation temperature, dose, and dose rate. In silicon device manufacturing these parameters must be accurately controlled in order to obtain reproducible electrical dopant profiles [7]. The present work reports on a detailed study on the competing influence of temperature and dose on the shape of as-implanted depth profiles of phosphorus. The experimental results are not only interpreted qualitatively, they can also be reproduced quantitatively by atomistic computer simulations.

Phosphorus ions were implanted into a p-type (001) Si substrate at 140 keV at doses of about $5x10^{13}$ $cm^{-2}$ and $5x10^{15}$ $cm^{-2}$ at a dose rate of about $5x10^{11}$ $cm^{-2}$ $s^{-1}$. The exact values of the implanted doses are given in Figs. 1 and 2. Implantations in both the [001] axial channel direction and in a direction 7° off axis were performed. The ion beam was aligned into the [001] direction prior to implantation by a standard procedure employed in channeling Rutherford backscattering spectrometry (RBS/C) [8]. For the nonchanneled low dose implants, the 7° tilt angle with respect to [001] and the 22.5° rotation angle relative to [110] were set using the five-axis goniometer that was employed for beam alignment for [001] channeling implantation. The high dose implant was performed using the standard implanter setup for 7° tilted implantations. The implantations were carried out at room temperature (RT) as well as at elevated temperatures (300 and 350°C). The temperature was controlled by a thermocouple. For the high temperature implants a BORALECTRIC® heater was used. After implantation, RBS/C analysis was performed to obtain information about the as-implanted damage. The phosphorus depth profiles were measured by secondary ion mass spectrometry (SIMS) at Evans East (East Windsor, NJ) using a Phi quadrupole SIMS instrument. The P detection limit in Si was $1x10^{15}$ $cm^{-3}$. The accuracy of the depth calibration was 5-10%.

The thick lines in Figs. 1 (a) and 1 (b) depict the SIMS data for the low dose implants at RT and at 350°C, respectively. A comparison of Figs. 1 (a) and 1 (b) shows that the shape of the phosphorus profiles obtained by channeling implantation is strongly dependent on the temperature. The profiles of the tilted implants are nearly independent of temperature. At an implantation dose of about $5x10^{13}$ $cm^{-2}$, the accumulation of radiation defects is small so it should not cause much dechanneling of the incident ions. Therefore, the temperature dependence observed for the channeling implantation profiles is solely attributed to thermal vibrations whose dechanneling effect is considerably stronger at 350°C (Fig. 1 (b)) than at RT (Fig. 1 (a)).

The phosphorus profiles obtained by the high dose implantation at RT and at elevated temperatures (300 and 350°C) are depicted in Figs. 2 (a) and 2 (b), respectively. Again, a significant dependence of the shape of the phosphorus profiles on the temperature is found. However, this dependence is opposite that observed in Fig. 1 for the low dose implant. This can be explained as follows. For the RT implant (Fig. 2 (a)), the damage buildup during ion bombardment causes strong dechanneling of the incident ions. Therefore, the shape of the channeling implantation profile differs greatly from that in Fig. 1 (a). In the case of the tilted implant, the channeling tail is not as pronounced as it is in Fig. 1 (a) since ion-beam-induced defect accumulation also prevents rechanneling. RBS/C measurements show that in both channeling and tilted implantations an amorphous layer about 280 nm thick formed. It should be noted, however, that this layer is not the main cause of the alteration in profile shape, it is the damage buildup below the amorphization threshold [6].

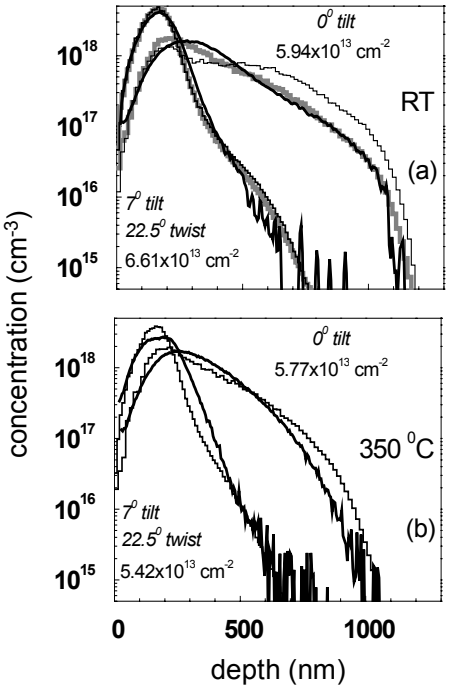


**Fig. 1:** P depth profiles obtained by 140 keV implantation into (001) Si at a dose of about $5x10^{13}$ cm$^{-2}$, at RT (a) and at 350°C (b). The exact doses are shown. Two orientations of the ion beam were considered: (i) parallel to the [001] channel direction and (ii) 7° off this direction. In the second case, the angle between the projection of the beam direction on the (001) plane and the [110] direction was 22.5°. The depth axis is parallel to [001]. The profiles depicted by thick lines were measured by SIMS at Evans East, East Windsor, NJ. The histograms show results of atomistic simulations that do not (black) and do (gray) consider damage buildup during implantation.

The shapes of the phosphorus profiles shown in Figs. 1 (b) and 2 (b) are rather similar. Obviously, at elevated temperatures the accumulation of defects which are relevant for dechanneling of the implanted ions is very small, in contrast to RT implantations. Therefore, at 300 and 350°C, these defects formed by previous ion impact should largely have disappeared before a subsequently implanted ion hits the same region of the target. The period between consecutive ion impacts into a target region where the amount of nuclear energy deposition (or displacements per atom) is larger than a critical value can be roughly estimated in the following manner. Assuming that the cascade region of a single ion impact can be modeled by a cylindrical track [9], the lateral cross-section $\sigma_0$ of this region can be calculated using

$$\sigma_0 = \frac{S_n}{E_c}.$$

$S_n$ is the nuclear stopping cross-section of the ion in the target. The critical nuclear energy deposition per atom for defect production, $E_c$, should be somewhat lower than the displacement energy for Frenkel pair generation, $E_d$, in a virgin silicon crystal, since most displacements occur in the region of a collision cascade where the target structure is no longer perfect. In the case of 140 keV phosphorus implantation, the use of the universal nuclear stopping cross-section [10] , and assuming $E_c = 0.25\ E_d$ ($E_d$ = 15 eV), leads to a lateral cross-section $\sigma_0$ of about 1 nm$^2$. Therefore, at the dose rate of $5x10^{11}$ cm$^{-2}$ s$^{-1}$, the time between consecutive ion impacts in a damaged region is of the order of 100 s. Together with previous considerations, this means that at 300 and 350°C the lifetime of defects relevant for the dechanneling is smaller than this period.

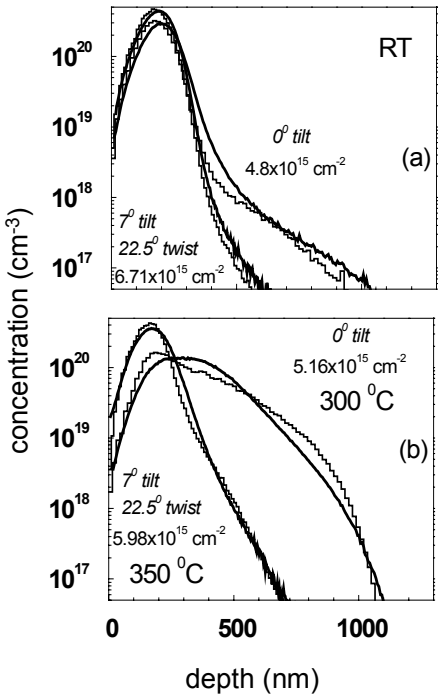


**Fig. 2:** Phosphorus depth distributions for 140 keV implantation at a dose of about $5x10^{15}$ cm$^{-2}$. Thick lines and histograms depict SIMS data and results of computer simulations, respectively. Similar to Fig. 1, the results of channeled and tilted implantations at RT (a) and at elevated temperature (b) are shown. At RT, both the channeled and the tilted implant led to amorphization. The thickness of the amorphous layer determined by RBS/C is 280 nm. The simulations yielded a thickness of 278 nm.

Atomistic computer simulations showed that the as-implanted defect structure consists of a variety of defect species [11,12]. Many single vacancies and self-interstitials as well as a certain percentage of complex defects that contain tens to hundreds of atoms form. The latter may be considered as the defects mainly responsible for dechanneling of the implanted ions [6]. The simulations demonstrated that such complex defects shrink considerably at a few 100°C [11], within 1 ns of their formation. This is consistent with the present experimental results.

The measured P depth distributions were simulated using the Crystal-TRIM program which is described in detail elsewhere [6,13-15]. This code treats the motion of implanted ions in the target material within the framework of the binary collision approximation, i.e., by the consideration of a sequence of binary collisions with target atoms in close vicinity to the ion trajectory. The black histograms in Fig. 1 show the results obtained for the low dose implant at RT and at 350°C. The agreement with the experimental data is good. In the simulations, the target was assumed to consist of a perfect Si crystal with a native $SiO_2$ surface layer 1.5 nm thick. The following values were used for parameters $C_\lambda$ and $C_{el}$ in the model for the electronic energy loss of an incident ion in a collision with a target atom [13,14]: $C_\lambda = 1.0$ and $C_{el} = 1.38$. The first parameter was employed to calculate the electronic energy loss averaged over all impact parameters using the electronic stopping cross-section given in [10]. The second parameter describes the impact-parameter dependence of electronic energy loss in the modified Oen-Robinson model [13,14,16]. Thermal vibrations of the lattice atoms were treated as follows. Since the time of binary projectile-target collision is generally much shorter than the period of thermal vibration of a lattice atom, it suffices to consider the instantaneous thermal displacement of the atom. It is assumed to obey a Gaussian distribution with a root-mean-square (*rms*) $\langle u^2 \rangle^{1/2}$ obtained by the Debye model [17]:

$$p(x) = \frac{1}{(2\pi \langle u^2 \rangle)^{1/2}} \exp\left(-\frac{x^2}{2\langle u^2 \rangle}\right) ,$$

$$\langle u^2 \rangle^{1/2} = \frac{12.06 \text{ Å}}{\left(\frac{T_D}{\text{K}} \frac{M_t}{\text{amu}}\right)^{1/2}} \left(\frac{1}{4} + \frac{1}{y^2} \int_0^y \frac{z\, dz}{\exp(z) - 1}\right)^{1/2} ,$$

$$y = \frac{T_D}{T} ,$$

where $M_t$ is the mass of a target atom. $T_D$ and $T$ are the Debye temperature and the actual temperature of the target, respectively. In the Crystal-TRIM code a Debye temperature of 500 K is used. This value is in agreement with results of precise channeling radiation measurements of thermal vibrational amplitudes [18,19]. The formula for the *rms* of thermal displacements shows that the temperature dependence of this quantity is particularly pronounced if the Debye temperature is relatively low, like in the case of silicon. For example, if under otherwise identical conditions a silicon carbide target with $T_D = 1120$ K were to be used in low dose P implantation, the temperature dependence of the profile shape would be much smaller than that in the case of Si.

Atomistic computer simulations were also performed for the high dose (about $5 \times 10^{15}$ cm$^{-2}$) implants. In Fig. 2 the histograms show the results. In order to describe the accumulation of defects which are relevant for dechanneling of the implanted ions, a known phenomenological model for the damage buildup, elucidated, e.g., in [20], was employed in simulation of the profiles obtained at RT implantation. The introduction of such a model is necessary, since Crystal-TRIM *per se* can only treat ballistic processes during ion bombardment, not subsequent relaxation processes which are responsible for the formation of the final as-implanted defect structure. In the simulations, the values of the two model parameters $C_a$ and $p_t$ (cf. [20], Eq. (1)) were 5.33 meV$^{-1}$ and 0.1, respectively. These data were also employed in previous investigations [6] of dechanneling of implanted P ions. Both parameters are used to calculate the probability that a P ion collides with an atom located within a region of an extended defect. $C_a$ and $p_t$ describe the increase of this probability with growing nuclear energy deposition per target atom and the onset of amorphization in the target region considered, respectively. Fig. 2 (a) shows a good agreement between the SIMS data and the simulated profiles. The thickness of the amorphous layer calculated by Crystal-TRIM is nearly identical to the measured value. The damage buildup model was also used to simulate the low dose implants at RT. In Fig. 1 (a) the gray histograms show the corresponding results. The agreement with the experimental data is better than for simulations that do not consider damage buildup. This shows that in RT implants, at a dose of about $5 \times 10^{13}$ cm$^{-2}$, defect accumulation influences slightly the shape of channeling implantation profiles. In the simulation of the P profiles obtained at elevated temperatures damage buildup is completely neglected. The good agreement with experimental data (Fig. 2 (b)) demonstrates the validity of this assumption.

The results of atomistic simulations are generally consistent with the qualitative interpretation of the experimental results given above. The small deviation between simulated and measured depth profiles should be mainly due to the relatively simple models used in the simulations for electronic energy loss, lattice vibrations, and damage buildup.

## Acknowledgements

The authors are grateful to Evans East, East Windsor, NJ, for the SIMS analysis. In particular they thank Dr. M. S. Denker and Dr. S. W. Novak for valuable comments.

The present results have been recently published as M. Posselt *et al.,* Appl. Phys. Lett. **83** (2003) 545.

## References

[1] G. Dearnaley, J.H. Freeman, G.A. Gard, M.A. Wilkins, Can. J. Phys. **46** (1968) 587

[2] G. Carter, W.A. Grant, Ion Implantation of Semiconductors, Edward Arnold Ltd., London, 1976

[3] R.G. Wilson, J. Appl. Phys. **60** (1986) 2797

[4] K.M. Klein, C. Park, A.F. Tasch, Nucl. Instr. Meth. B **59-60** (1991) 60

[5] G. Hobler, Radiat. Eff. Defects Solids **139** (1996) 21

[6] M. Posselt, B. Schmidt, C.S. Murthy, T. Feudel, K. Suzuki, J. Electrochem. Soc. **144** (1997) 1495

[7] E. Rimini, Ion Implantation: Basics to Device Fabrication, Kluwer Academic Publishers, Boston, 1995

[8] W.-K. Chu, J.W. Mayer, M.-A. Nicolet, Backscattering Spectrometry, Academic Press, New York, 1978

[9] F.F. Morehead Jr., B.L. Crowder, Radiat. Eff. **6** (1970) 27

[10] J.F. Ziegler, J.P. Biersack, U. Littmark, The Stopping and Range of Ions in Solids, Pergamon Press, New York, 1985

[11] M.-J. Caturla, T. Diaz de la Rubia, L.A. Marques, G.H. Gilmer, Phys. Rev. **B 54** (1996) 16683

[12] M. Posselt, Mat. Res. Soc. Symp. Proc. **647** (2001), O2.1.1

[13] M. Posselt, Radiat. Eff. Defects Solids **130/131** (1994) 87

[14] C.S. Murthy, M. Posselt, T. Frei, J. Vac. Sci. Technol. **B 14** (1996) 278

[15] M. Posselt, B. Schmidt, T. Feudel, N. Strecker, Mater. Sci. Eng. B **71** (2000) 128

[16] O.S. Oen, M.T. Robinson, Nucl. Instr. Meth. **132** (1976) 647

[17] M. Blackman, in: Handbuch der Physik, edi ted by S. Flügge, Part 1, Vol. VII, Springer Verlag, Berlin, 1955, p. 327

[18] S. Datz, B.L. Berman, B.A. Dahling, M.V. Hynes, H. Park, J.O. Kephart, R.K. Klein, R.H. Pantell, Nucl. Instr. Meth. B **13** (1986) 19

[19] J.O. Kephart, B.L. Berman, R.H. Pantell, S. Datz, R.K. Klein, H. Park, Phys. Rev. **B 44** (1991) 1992

[20] M. Posselt, L. Bischoff, J. Teichert, Appl. Phys. Lett. **79** (2001) 1444

# Low Quartz Structure at the $SiO_2$/Si Interface Revealed by Positron Annihilation Spectroscopy

G. Brauer, W. Anwand, W. Skorupa, A.G. Revesz[1] and J. Kuriplach[2]

[1] *Revesz Associates, Bethesda, MD, USA;*
[2] *Department of Low Temperature Physics, Charles University, Prague, Czech Republic*

Silicon and its oxide have been the dominant electronic materials of semiconductor technology for several decades up to now. The industrial drive to an ever higher packing density of CMOS devices requires the need of ever thinner oxides for gate dielectrics, and in the present standard technology this thickness is already down to about 2 nm. Nevertheless a physical understanding of the $SiO_2$/Si interface is still far from being complete but crucial to the future of very-large-scale integration (VLSI) technologies. Attempts to model the $SiO_2$/Si interface, and the search for experimental support of these models, can be broadly divided into three categories: (i) the transition is thought to proceed via an ordered, stable bulk phase of $SiO_2$ bearing an epitaxial relationship to the Si substrate, (ii) the transition is thought to proceed via a ‚substoichiometric' oxide layer, and (iii) an abrupt transition, with no intervening layer, takes place. A comprehensive review of such efforts until 1995 can be found in the literature [1].

Positron Annihilation Spectroscopy (PAS), mainly in the form of Slow Positron Implantation Spectroscopy (SPIS) using monoenergetic positrons thereby studying the Doppler broadening of annihilation radiation as a function of positron energy $E$, has been used to study the $SiO_2$/Si system – a review of the work until 1994 was published in Ref. [2].

The interpretation of experimental results has usually been based on the assumption of an interface region at the $SiO_2$/Si interface. The width of this region was considered to be 1 nm and it was concluded that positrons are trapped at unspecified defects in this region, i.e. the nature of these defects could not be revealed. An improved approach for the analysis of SPIS Doppler broadening data was introduced by using a combination of the Doppler broadening lineshape parameters $S$ and $W$ [3, 4]. $S$ is a measure of the electron momentum density at low momentum, i.e. represents preferably valence electrons, whereas $W$ is a measure of the electron momentum density at high momentum, i.e. represents more tightly bound electrons of the atom where the annihilation takes place. From detailed studies of different metal-oxide-semiconductor (MOS) systems under bias [3, 4] it was concluded that the $SiO_2$/Si interface can be characterized by its own $S$ and $W$ parameters. However, in the case of low and intermediate electric fields, and even when no bias is applied, the trapping of positrons also occurs in the oxide layer and an additional positron trapping layer between the interface and bulk oxide was invoked. Again, the structure of this layer could not be specified.

It is well known that thermally grown or deposited $SiO_2$ films on silicon are similar to silica glass [vitreous (v)-$SiO_2$] in the sense that they are also non-crystalline (nc). Therefore, PAS results obtained with v-$SiO_2$ and with quartz crystals (having similar but not exactly identical Si-O bonds) are relevant to PAS studies of $SiO_2$ films on silicon. Differences in any parameters obtained by PAS of such solids are mainly due to the fact that all these materials differ by the amount of positronium (Ps), a bound state between an electron and a positron, formed. Ps atoms may exist in a para- or ortho-state, i.e. with the spins of electron and positron being antiparallel (p-Ps) or parallel (o-Ps), respectively, and are formed in the ratio p-Ps / o-Ps = 1/3 for probabilistic reasons.

Based on these considerations, it is certain that the interactions of positrons and Ps (if formed) in $SiO_2$ polymorphs affect not only $S$, as it has usually been considered until 1994 [2], but $W$ as well. Indeed, all SPIS work performed after 1995 on $SiO_2$/Si systems and other materials present data on $S$ and $W$ and/or make use of $S$-$W$ plots. Ps formation in $SiO_2$ films [5-7], or the lack of it [2], has been discussed up to now in conjunction with unspecified defects in the $SiO_2$/Si interface layer. Another study claims that (i) high concentrations of divacancies exist in Si domains at the interfaces formed with natural oxides obtained after etching, and (ii) positrons see the same annihilation state at various $SiO_2$/Si interfaces where the oxides are either commercial, thermally grown, native, or obtained after rapid thermal annealing [8]. From a combined SPIS/AES (AES = Auger electron spectroscopy) study of $SiO_2$ layers wet grown on

silicon the existence of an extensive transition zone of 17-23 nm thickness has been discussed and concluded [9].

During the past decades repeatedly observations of various features were reported from which it was concluded that the oxide at the $SiO_2$/Si interface is similar in a varying degree to one of the crystalline $SiO_2$ polymorphs [1]. For example, from transmission electron microscopy (TEM) [10] and X-ray diffraction [11] studies the transformation from crystalline silicon to amorphous $SiO_2$ was suggested to take place via a very thin ordered crystalline oxide layer consisting of tridymite, a stable bulk form of $SiO_2$. More recently, interface structures of $SiO_2$/Si(001) were studied by using the first-principles molecular dynamics method [12].

In our investigation, a $SiO_2$ film of ~80 nm thickness was thermally grown on a Czochralski-grown Si (100) substrate (n-type, 6-10 Ωcm) at 1000 °C. After cutting, several samples having a size of about 10 mm x 10 mm were obtained. Thinner $SiO_2$ films were then produced by etching multiples of about 20 nm from a sample having the originally grown film of ~80 nm thickness. The standard etchant consists of 300 ml $H_2O$, 19 ml HF and 11 ml $H_3PO_4$, and an etching rate of 12 nm/min was experimentally determined in good agreement to values known from the literature [13]. An estimation of the remaining $SiO_2$ layer thickness after etching was performed using standard ellipsometry (Sentech SE 400) based on a refractive index of $n$ = 1.467, well known for relaxed thermally grown $SiO_2$. In addition, for two samples the film thickness was estimated using the refractive index $n$ = 1.549, well known for low quartz, and by TEM for comparison. The $SiO_2$/Si samples studied and their characteristics are listed in Table 1. It must be stressed that thickness values below 5 nm given from standard ellipsometry should be taken with caution [14] and are presented for completeness only. Therefore, the thickness values measured by TEM seem to be more reliable but this does not imply any indication of a preferred refractive index of the $SiO_2$ film when compared with the ellipsometric data given.

For the sake of interpretation and comparison of SPIS results obtained on thermally grown $SiO_2$ , the *S-W* plot of data measured on reference samples of silicon, Brazilian quartz having low quartz structure, and synthetic silica glass (v-$SiO_2$) are shown in Fig. 1. The *S-W* plots of data measured on samples thermally grown $SiO_2$ and etched afterwards are presented in Fig. 2.

The *S(E)* and *W(E)* data differ from any corresponding SPIS data presented in earlier studies in the literature by the fact that the lowest positron energy chosen is $E$ = 30 eV. In addition, *S-W* plots (Figs. 1, 2) shed a new light on the understanding of *S(E)* and *W(E)*. Taking all data together, the densification of the $SiO_2$ towards the interface, as already concluded in a recent work [15], is confirmed to exist in thinner oxides obtained by etching, too.

**Table 1:** Thickness $d$ of $SiO_2$ films of $SiO_2$/Si samples studied: Samples 1-5 are thermally grown and etched films, whereas sample 6 is a native oxide film grown for at least six months. Thickness values given in column 1 are estimated using the refractive index of thermally grown $SiO_2$, those of column 2 are estimated using the one for low quartz. The values of column 3 are measured by TEM.

| Sample | $n$=1.467 $d$ (nm) | $n$=1.549 $d$ (nm) | TEM $d$ (nm) |
|---|---|---|---|
| 1 | 84.2 | | |
| 2 | 62.7 | | |
| 3 | 38.3 | | |
| 4 | 20.5 | | |
| 5 | 1.8 [a] | 2.0 [a] | 1.4 |
| 6 | 2.4 [a] | 3.7 [a] | 1.7 |

[a] Values < 5 nm should be taken with caution (see [14])

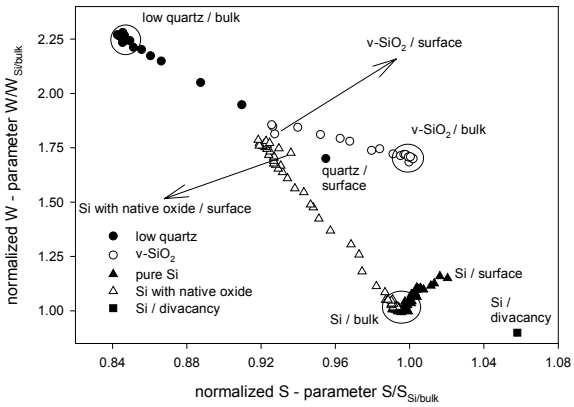


**Fig. 1:** $W/W_b$ vs. $S/S_b$ plot for different standard samples and a defect state in Si. An untreated Si(100) sample served as a reference ($S_b$ , $W_b$) for normalization.

When only two distinct annihilation characteristics, described by ($S_1$, $W_1$) and ($S_2$, $W_2$), contribute to a set of experimental data, a straight line is obtained in the *S-W* representation where the endpoints represent the two states itself. In Figs. 1, 2 some distinct characteristics of $SiO_2$ polymorphs and Si are given. If no interface state

existed, we should observe a straight transition, as indicated by a dashed line in Fig. 2, between the *S*-*W* values characterizing the bulk of v-$SiO_2$ and Si,

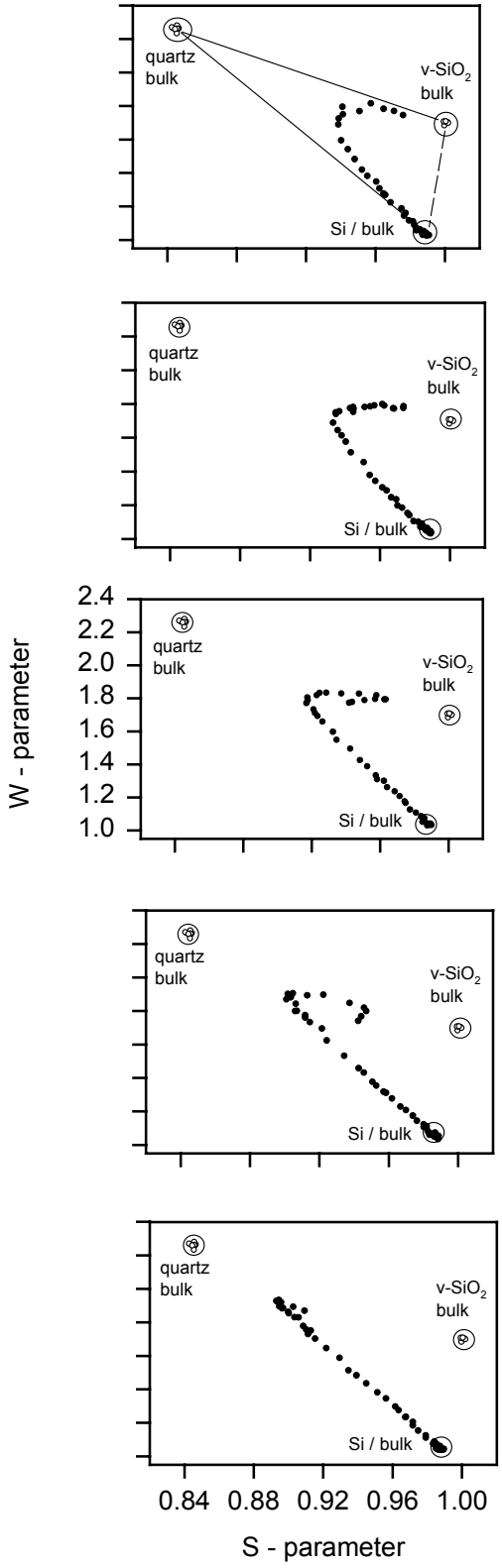


**Fig. 2:** $W/W_b$ vs. $S/S_b$ plot for different $SiO_2$/Si samples, 1(top) to 5 (bottom) with $SiO_2$ thickness values as given in Table 1, in relation to the bulk state of different standard samples. An untreated Si(100) sample served as a reference ($S_b$ , $W_b$) for normalization.

respectively. Indeed, from the data measured for the etched samples (Fig. 2) we observe that an annihilation state is revealed in the oxide which must resemble low quartz in its structure. Interestingly, the comparison with native oxides does reveal the same features, i.e. allows to draw the same qualitative conclusion about its structure being close to the one of low quartz. In case of Si divacancies supposed to exist in Si domains at the $SiO_2$/Si interface [8] the transition between the bulk values of v-$SiO_2$ and Si should exhibit a curvature towards the *S*-*W* value representing the Si divacancy (see Fig. 1) which is evidently not the case. Therefore, the present results certainly rule out such an interpretation of the experimental data.

Further support of the conclusion that a very thin $SiO_2$ layer with the structure of low quartz does exist at the $SiO_2$/Si interface may be taken from independent PAS/SPIS results available in the literature as follows:

Positrons in a MOS structure driven towards the $SiO_2$/Si interface by a bias are always stopped and annihilated at the interface – this is an experimental fact [3] which could not be explained by these authors in terms of the interface structure. If our interpretation of low-quartz structure at the interface is combined with recent theoretical results [16], indicating that thermalized positrons are repelled from the interface if coming from a crystalline $SiO_2$ side to Si, the experimental facts from Ref. [3] can now be understood completely.

Although our conclusion from SPIS that the interface exhibits the structure of low quartz is based on solid experimental evidence, it has to be pointed out that this does not necessarily mean that indeed a crystalline quartz layer must exist at the $SiO_2$/Si interface with an exclusive fixed Si-O-Si bond angle of 144°, like in low quartz. This is connected with the fact that an oxide grows inwards, i.e. towards the Si substrate, so that a crystalline layer - if it is present at all at the beginning of the oxidation – would be permanently pushed towards the outer surface or becomes non-crystalline during growth, which eventually has to result in this fixed bond angle.

In conclusion, an annihilation state is revealed in thermally grown and etched, as well as in native oxide, which must resemble low quartz in its structure. In our recent paper [17], a more extensive discussion of this finding together with further experimental details is combined with a variety of state-of-the-art theoretical calculations. There it is also discussed why the SPIS results corroborate the model of quasi-epitaxial oxide growth and pseudo-polymorphic relaxation of the grown oxide.

## Acknowledgements

The contribution of G. Brauer was supported by Sächsisches Staatsministerium für Wissenschaft und Kunst, Grant no. 7531.50-02-844-01/3. We are thankful to colleagues from FZ Rossendorf for their help with oxide sample preparation (T. Gebel), and thickness measurements by ellipsometry (I. Beatus) and TEM (A. Mücklich).

## References

[1] C.J. Sofield, A.M. Stoneham, Semicond. Sci. Technol. **10** (1995) 215

[2] P. Asoka-Kumar, K.G. Lynn, D.G. Welch, J. Appl. Phys. **76** (1994) 4035

[3] M. Clement, J.M.M. De Nijs, A. van Veen, H. Schut, P. Balk, J. Appl. Phys **79** (1996) 9029

[4] M. Clement, J.M.M. De Nijs, A. van Veen, H. Schut, P. Balk, IEEE Trans. Nucl. Sci. **42** (1995) 1717

[5] A. Uedono, L. Wei, S. Tanigawa, R. Suzuki, H. Ohgaki, T. Mikado, T. Kawano, Y. Ohji, J. Appl. Phys. **75** (1994) 3822

[6] M. Hasegawa, M. Tabata, T. Miyamoto, Y. Nagashima, T. Hyodo, M. Fujinami, S. Yamaguchi, Mat. Sci. Forum **175-178** (1995) 269

[7] K. Eriguchi, Y. Harada, M. Niwa, J. Appl. Phys. **87** (2000) 1990

[8] H. Kauppinen, C. Corbel, L. Liszkay, T. Laine, J. Oila, K. Saarinen, P. Hautojärvi, M.-F. Barthe, G. Blondiaux, J. Phys.: Condens. Matter **9** (1997) 10595

[9] W. Anwand, G. Brauer, P.G. Coleman, A. Goodyear, H. Reuther, K. Maser, J. Phys.: Condens. Matter **9** (1997) 2947

[10] A. Ourmazd, D.W. Taylor, J.A. Rentschler, J. Bevk, Phys. Rev. Lett. **59** (1987) 213

[11] L. Brügemann, R. Bloch, W. Press, P. Gerlach, J. Phys.: Condens. Matter **2** (1990) 8869

[12] T. Yamasaki, C. Kaneta, T. Uchiyama, T. Uda, K. Terakura, Phys. Rev. B **63** (2001) 115314

[13] T. Gebel, PhD Thesis, Technical University of Dresden (2002)

[14] G. Jungk, T. Grabolla, Thin Solid Films **335** (1998) 253

[15] A.G. Revesz, W. Anwand, G. Brauer, H.L. Hughes, W. Skorupa, Appl. Surf. Sci. **194** (2002) 101

[16] J. Kuriplach, W. Anwand, G. Brauer, W. Skorupa, Appl. Surf. Sci. **194** (2002) 84

[17] G. Brauer, W. Anwand, W. Skorupa, A.G. Revesz, J. Kuriplach, Phys. Rev. B **66** (2002) 195331

# A Modified Cs Sputter Ion Source with Increased Lifetime

M. Friedrich and H. Tyrroff

Cs sputter ion sources are the mainly applied negative ion sources at electrostatic tandem accelerators [1]. For example, the injector of the Rossendorf Tandetron accelerator [2] is equipped with a Cs sputter ion source of type HVEE 860-C (Fig. 1).

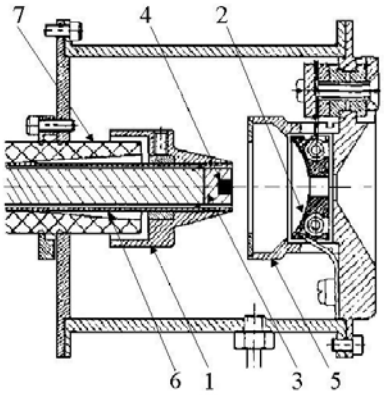


**Fig. 1:** Construction of the inner part of the Cs sputter ion source HVEE 860-C: (1) cathode-shielding electrode, (2) spherical ioniser, (3) sputter cathode, (4) sputter material insert, (5) primary beam-forming electrode, (6) cathode rod leading tube, (7) cathode insulator.

The availability of electrostatic accelerators is significantly influenced by the lifetime and the operation stability of the ion sources. Therefore, development activities have been directed to the improvement of the ion source operation. In a first step, the time between two maintenance openings of the Cs sputter ion source could be increased from 300 h to about 1000 h by careful source handling, especially by source operation only at sufficiently low gas pressure [3]. However, a significant erosion was observed at the inner source parts, in particular the cathode shielding electrode (see Fig. 1), which limits the lifetime critically. This erosion could not be reduced by any alteration of the operation conditions, nor by use of different materials for the source parts. It was found to be independent of the species of generated ions. Because of the cylindrical symmetry of the observed erosion patterns, any gas discharge in the mirror-symmetric field of the electron-suppression magnets could be excluded as a reason. However, the independence of the magnetic field for electron suppression indicated that the erosion may be created by heavy ion bombardment. Especially noticeable is the sharp borderline of the erosion on the outer side of the shielding electrode and the ring cut from the inner side of the cathode rod leading tube (Fig. 2).

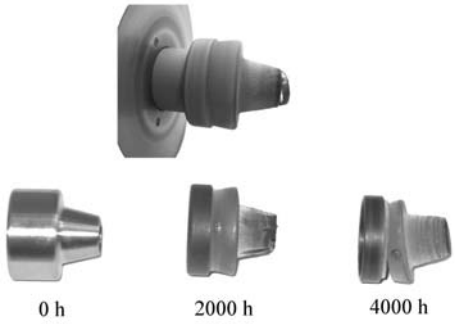


**Fig. 2:** View of the erosion at the cathode parts after about 1000 h (top), and time dependent erosion at the cathode-shielding electrode (bottom).

The trajectories of the primary Cs ions generated at the surface of the spherical ioniser hit the centre of the sputter cathode (for simulations generated with the program SIMION [4], see Fig. 3), and cannot cause these patterns. A progress in understanding the phenomenon has been achieved by including into the calculations Cs ions generated at other hot surfaces outside the spherical ioniser surface. In Fig. 3, the corresponding trajectories are also shown.

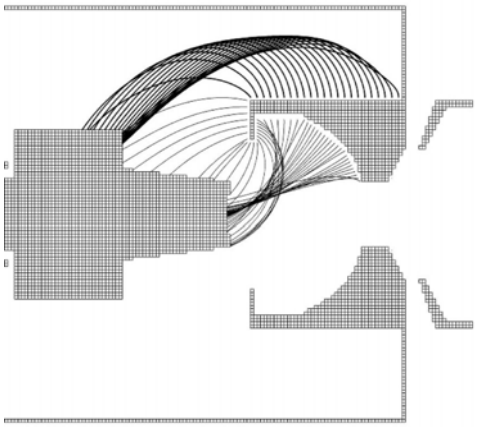

**Fig. 3:** Calculated trajectories of Cs ions generated at the ioniser and at hot surfaces around it with an initial energy of 1 eV and at a sputter voltage of 7 kV.

There is an excellent match between the calculated ion trajectories and the observed erosion

patterns. The sputter effects on the outer side of the shielding electrode are created by Cs ions starting at the outer surface of the beam-forming electrode, especially from the front corner, where a high electric field exists. The ring cut from the cathode rod leading tube is created by Cs ions from the inner side of the beam-forming electrode opposite to the ioniser.

The calculations demonstrate that unwanted Cs ions from hot surfaces close to the ioniser destroy the cathode parts and lead to a necessary source maintenance after about 1000 h of operation time. To increase the lifetime of the ion source the generation of these ions should be prevented, or they have to be stopped before hitting the cathode. In a first step a shielding electrode on ground (ioniser) potential was arranged between the cathode and the beam-forming electrode. It prevents the bombardment of the cathode by ions from the outer surface of the beam-forming electrode and results in reduced sputter effects at the cathode-shielding electrode, and thereby in an increased lifetime of the source. The Cs ions from the inner side of the beam-forming electrode could not be suppressed in this way so that significant erosion remained at the border of the sputter cathode and the neighbouring leading tube. As the suppression of these ions by additional electrodes turns out to be rather complicated, the activities were directed to reduce the generation of Cs ions at this surface. A reduced surface ionisation is obtained by reducing the temperature of the electrode. Therefore, the beam-forming electrode was connected with the additional shielding electrode and the direct thermal connection to the ioniser was interrupted.

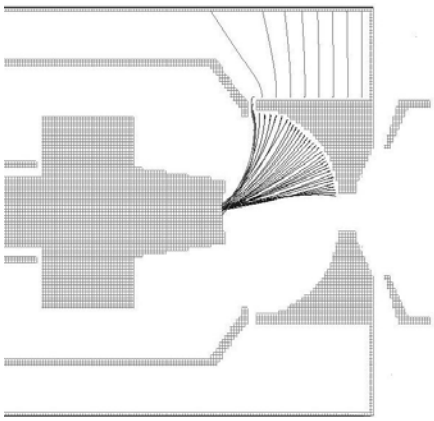

**Fig. 4:** Modified inner part of the Cs sputter ion source HVEE 860-C and calculated trajectories.

To reduce the temperature of the beam-forming electrode the additional shielding electrode is connected to the coldest part of the inner ion source arrangement, which is positioned far from the ioniser. The arrangement [5] and the calculated trajectories are shown in Fig. 4.

During test operation this modified source has not shown any remarkable erosion on any cathode part. Furthermore, the primary beam spot on the sputter material insert has been improved. The beam diameter on the sputter material has been decreased from 1.0-1.5 mm to about 0.5 mm, and the sputter crater now exhibits a better cylindrical shape also for materials melting at lower temperatures. The installed additional shielding electrode reduces also the thermal radiation to the cathode. Due to the reduced temperature a stronger condensation of Cs on the sputter cathode has been observed, which requires a more careful handling of the Cs heating procedure, especially at start of source operation. The last version of this source is in operation since July 2002 without any maintenance, except for two refillings of the Cs reservoir without opening the ion source. The operation time at end of 2003 was about 3300 h.

In conclusion, parasitic Cs ions generated at hot surfaces nearby the ioniser were found to erode the cathode parts and limit the lifetime of the Cs sputter ion source HVEE 860-C. The observed erosion patterns and the calculated Cs ion trajectories show an excellent agreement. The unwanted Cs ions have been suppressed by an additional shielding electrode inside the ion source, and by reducing the temperature of the beam-forming electrode. Due to these modifications, the erosion of the inner ion source parts has been significantly reduced. This results in an increased lifetime of the ion source and a higher availability of the accelerator. The described modification is covered under FZR/DE Patent Number 10241252.9 and US Application Number 10/655.896.

## References

[1] D.W.J. Mous, A. Gottdang, R. van den Brook, R.G. Haitsma, Nucl. Instr. Meth. B **99** (1995) 697

[2] G.D. Alton, Nucl. Instr. Meth. B **73** (1993) 221

[3] M. Friedrich, W. Bürger, D. Henke, S. Turuc, Nucl. Instr. Meth. A **382** (1996) 357

[4] D.A. Dahl, SIMION 3D Version 6.0 (1995)

[5] M. Friedrich, H. Tyrroff, Nucl. Instr. Meth. B **201** (2003) 645

# Ion-Solid-Interaction

*D. Kost*
*S. Facsko*
*H. Tyrroff*
*Z.D. Pešić*[1]
*R. Hellhammer*[1]
*N. Stolterfoht*[1]

**Potential energy retention of highly charged argon ions in Au surfaces**

For a comparative study for different solid surfaces, the retention of potential energy of multiple charged Ar ions into clean Au surfaces was studied. With a calorimetric setup the target temperature increase was measured during the bombardment with $Ar^{q+}$ (q=1-8) ions with kinetic energies varying between 60 eV/q and 200 eV/q. Extrapolating to zero kinetic energy, the deposited potential energy is separated from the deposited kinetic fraction. The potential energy retention coefficient into clean Au surfaces results as 0.9±0.1, almost independent on the charge state of the ions. Compared to former results obtained on Si (0.6±0.2) and on unprepared Cu surfaces (0.2±0.1) the retention in clean Au surfaces is considerable higher. Additionally, in order to identify the differences in the relaxation mechanisms on the different surfaces, the amount of energy was measured, which is released from Si and Au surfaces during the ion-surface interaction by secondary electrons. First results of the measured integral electron emission show a dependence of the re-emitted energy on the kinetic energy of the multiple charge ions.

**Collaboration**: [1]Hahn-Meitner Institut, Berlin

*Ü. Dagkaldiran*[1]
*J. Meijer*[1]
*D. Grambole*
*F. Herrmann*
*H.-W. Becker*[1]
*E. Fritz*[1]
*H.-U. Schreiber*[1]

**Microchanneling investigation of ß-$FeSi_2$-structures**

The suggested direct band gap of 0.8 eV renders ß-$FeSi_2$ a promising candidate for silicon based µ-LED's. Monocrystalline ß-$FeSi_2$ layers would even open possibilities for µ-laserdiodes. However, the synthesis of these structures appears to be difficult. The combination of the ion projector at the Ruhr University of Bochum and the µ-Channeling set-up at FZR allows a fast synthesis as well as the analysis of such layers. First µC-RBS analyses of $FeSi_2$-structures, produced by Fe implantation into Si at an ion energy of 800 keV at different implantation temperatures and with structure sizes of 70-190 µm, demonstrate that bulk formation by Ostwald ripening depends on implantation temperature and structure size. Even if the layers do not show the desired crystalline characteristics, valuable information could be obtained on the damage and the layer structures. Additional Raman measurements showed clear fingerprints of ß-$FeSi_2$.

*Supported by DFG*

**Collaboration:** [1]Ruhr-Universität Bochum, Experimentalphysik III, Bochum

*W. Pilz*
*M. Friedrich*
*K.-H. Heinig*
*B. Schmidt*
*J. von Borany*

**AMS depth profiling of humidity in silica**

The AMS facility at the 3 MV Tandetron has been applied to depth profiling of humidity penetrated into as-implanted $SiO_2$ layers. For this aim, $Ge^+$ and $Si^+$ ion implanted $SiO_2$ layers ($10^{14}$-$10^{16}$ $cm^{-2}$) were exposed to an artificial atmosphere with $H_2{}^{18}O$ humidity. AMS allows the discrimination of isobar atomic and molecular ions, thus depth profiles of $^{18}O^-$ and $(^{18}OH)^-$ molecular ions could be investigated. Due to the separation of mass 19 by the injector magnet for depth profiling of $(^{18}OH)^-$ the influence of the disturbing molecules $H_2{}^{16}O$ and $^{17}OH$ is further suppressed. The measured depth profiles show enhanced humidity related $^{18}O$ and $^{18}OH$ concentrations up to a depth of about 40 nm, which is consistent with former results of H depth profiling by NRA and $^{18}O$ depth profiling by ToF-SIMS.

*C. Ramboz*[1]
*D. Strivay*[1,2]
*D. Grambole*
*F. Herrmann*

**Quantitative analysis of intra-crystalline inclusions by combined PIXE and RBS: Application to the dating of hydrothermal monazites**

Preceding PIXE and RBS investigations of ≈ 20 µm-wide solid and fluid inclusions in quartz at the Laboratoire Pierre Sue (CEA-Saclay, France) and CERI (Orléans, France) show that the quality of these analyses strongly depends on the availability of a µm-sized beam and its position stability. Thus,

additional PIXE measurements were carried out at FZR on six intra-crystalline monazite and two fluid inclusions in quartz using a 3x3 $\mu m^2$-sized beam which was scanned over a 10x10 $\mu m^2$ surface area. The depth and thickness and depth of the inclusions were deduced from the RBS spectra. By using these results in the PIXE data treatment with the GUPIX code, it was possible to compute the Th, U and Pb concentrations from the PIXE spectra and to determine the monazite age.
**Collaboration**: [1]ISTO-CNRS, Orléans, France; [2]Liège University, Belgium

*N. Razek*[1]
*D. Grambole*
*A. Schindler*[1]
*B. Rauschenbach*[1]

**H-depth distribution in semiconductor materials after hydrogen ion bombardment at 300 and 500 eV**

Recently, the effective removal of native oxide layers and carbon contaminations from GaAs, InP, Si and Ge surfaces has been demonstrated using low energy H-ion bombardment. For this purpose, a hot filament type broad beam ion source was employed with mass separation capability ( $H_2^+$, 300 eV, 4.5 $\mu A/cm^2$). Processing times between 5 and 25 min are usually applied which result in relatively low surface temperatures between 150°C and 350°C. For Si substrates, the $H_2^+$-cleaning treatment was successfully performed at 500 eV, 39 $\mu A/cm^2$, 250°C and 5 min. Hydrogen depth profiles were investigated after such cleaning procedures using NRA with a $^{15}N$ ion beam. An enhanced H concentration of > 5 at.% was found only up to a depth of 1.5 nm for GaAs, InP, Ge and 4.5 nm for Si, respectively.

*Supported by DFG*

**Collaboration:** [1]Leibniz-Institut für Oberflächenmodifizierung, Leipzig

*C. Neelmeijer*
*H.-P. Schramm*[1]

**Non-destructive surface characterization of a historic church window**

Visual inspection of historic windows (St. Marien Church Rostock) gave restorers the impression that the outside glass front might have been covered originally by a light attenuating organic painting material. This assumption was supported by chemical protein analysis showing a slight positive reaction. The hypothetical organic layer was visible on a 5 mm wide glass strip along the edge of the fretted lead. The adjacent large surface region was covered by corrosion products due to natural weathering. Analyses were performed using the combination of RBS and PIXE at the external proton beam ($E_p$ = 4 MeV, $I_p \sim$ 200 pA). On the bare glass strip RBS identified a thin Pb and Fe containing surface layer. PIXE proved that Si-K-radiation from the glass bulk was attenuated by this top layer. On the weathered glass area RBS-PIXE analysis found an extended surface layer containing Pb (leaching of the fretted lead) and Fe (pollution from metallic struts). From both results it was straightforward to identify the questionable painting material as a thin layer of initial corrosion. Obviously, the weathering process was suppressed in the narrow glass region due to its protection from the adjacent fretted lead.
**Collaboration:** [1]Laboratory of Scientific Art Analysis, Dresden

*C. Neelmeijer*
*A. Gumprich*[1]
*E. Pernicka*[1]

**The "Sky Disk of Nebra": Non-destructive gold composition analysis**

The spectacular bronze disk of 32 cm diameter and 2 kg weight (dated 1600 B.C.) is supposed to represent the world oldest image of the star sky. Green patina coating, naturally grown, is interrupted by numerous gold applications showing the sun and the moon set in a field of 30 glimmering gold stars, a golden horizontal arc (one lost) as well as another arc interpreted as a barque. Archaeologists are interested whether all the gold applications have one and the same composition. PIXE on air was chosen for non-destructive characterization of the silver and copper containing gold foils. Two PIXE detectors were used for simultaneous measurements: PIXE1 (no filter) for survey analysis and low-Z constituents, PIXE2 (30 µm Zn absorber) with selective filtering of the intense Au-L radiation for improvement of the Ag-K/Au-L intensity ratio. As

found, only the barque does not match the otherwise consistent gold composition.

**Collaboration:** [1]TU Bergakademie Freiberg, Archäometrie

# Biocompatible Materials

*T. Fitz*
*M.T. Pham*
*F. Prokert*
*H. Reuther*
*M.F. Maitz*
*E. Richter*

**Ion-beam assisted deposition of iridium oxide on stainless steel**

Vascular stents coated with $IrO_x$ thin films already have shown superior behaviour over bare metal stents in clinical studies due to free radicals scavenging properties that improve the blood compatibility. Reactive magnetron sputtering in oxygen atmosphere was tested as an alternative method for the production of these films. Plasma immersion ion implantation (PIII) of oxygen ions was applied to achieve good adhesion between the coating and the stainless steel substrate as well as to modify the film properties. Adherent films could be produced both on the outer and inner surfaces of the stent. The films are nanocrystalline with an average grain size which is adjustable by the deposition parameters. PIII, either as post implantation or during the deposition, improves the corrosion properties. Only then the redox current due to degradation in $H_2O_2$ was detectable in electrochemistry.

*Supported by Boston Scientific SCIMED*

*M.F. Maitz*
*M.-T. Pham*
*T. Fitz*
*I. Tsyganov*

**Blood compatibility of metal oxide surfaces**

Metal oxides can be produced by means of metal plasma immersion ion implantation in a very controlled way. This makes them interesting to investigate basic interactions of the haemostatic systems with foreign surfaces. $TiO_x$, $HfO_x$ and $IrO_x$ were deposited on stainless steel or silicon substrates; some were further ion implanted with C, N, P, or Ta ions at doses from $10^{15}$ to $10^{17}$ $cm^{-2}$. The films were physically characterized for composition, crystal structure, roughness, surface free energy, and corrosion properties. These parameters were correlated with blood platelet adhesion and degranulation, activation of the clotting and complement cascade, and adsorption and configuration changes of fibrinogen. Non-textured, nanocrystalline $IrO_x$ was the strongest activator of the two enzyme cascades. $TiO_x$ and naturally grown titanium oxide on nitinol generally induced lowest haemostatic reactions in all systems. Ion implantation generally resulted in an impaired hemocompatibility. No direct correlation with any of the surface properties could be found.

*Supported by Boston Scientific SCIMED*

*N. Shevchenko*
*M.T. Pham*
*M.F. Maitz*
*E. Richter*

**Ion implanted nitinol surfaces for biomedical applications**

The superelastic or memory shape alloy nitinol has big potential for biomedical applications, but due to the high content of the toxic nickel there are restrictions against it. Nickel has a higher sputtering yield than titanium, therefore PIII with nitrogen and/or argon was performed to reduce the surface nickel content of nitinol. Especially by implantation of nitrogen and by a sequential implantation of argon and nitrogen at 20-40 kV, fluences of (3-5)x$10^{17}$ $cm^{-2}$, temperature below 200°C, Nickel was depleted down to max. 1 at-% over a 50-70 nm surface layer. Below this a nickel enriched zone up to 500 nm was found with phases $Ni_4Ti_3$ and $Ni_{2.67}Ti_{1.33}$, indicating a reactive diffusion rather than a sputtering process. The surface obtained shows improved corrosion resistance. Growth and differentiation of rat bone marrow cells on these surfaces was not obviously altered, compared with untreated nitinol, but pro-coagulative effects, adherence of blood platelets and adsorption of fibrinogen, were higher than on native nitinol. This indicates that the titanium nitride rich surface may be more applicable for implants in bone, whereas for implants in the blood flow the production of an oxide surface might be preferable.

*M.T. Pham*
*M.F Maitz*
*H. Reuther*
*A. Muecklich*
*F. Prokert*

**Calcium phosphate nucleation by surface–bound extracellular matrix**

Implant coatings with calcium phosphate are widely used clinically by reason of their bone bonding–supporting behavior. The deposition from a solution allows mimicking the conditions to form bioactive hydroxyapatite, a modification of calcium phosphate. Generating homogeneous thin films is difficult

*G. Steiner*[1]

because the implant surface does not have enough nucleating sites. An organic polymer film of extracellular matrix (ECM) was shown to improve efficiently the nucleation of hydroxyapatite on a solid surface. The effect was demonstrated for a Si surface. Osteoblast–like SAOS–2 cells were plated and cultured on Si surfaces. The ECM secreted by cells and attached to the Si surface was exposed by selective removing of cells. This type of material surface ECM–Si was examined for its precipitation of calcium phosphate from a simulated body fluid. Hydroxyapatite homogeneously nucleated was observed on the ECM coated surface while a blank control Si surface did not induce any precipitation. Microscopic and spectroscopic results revealed the effect being associated with a collagen fibre–free extracellular matrix.

**Collaboration:** [1]TU Dresden, Institut für Analytische Chemie, Dresden

*S. Tunç*[1,2]
*G. Steiner*[1]
*M.T. Pham*
*M.F. Maitz*

**Conformation analysis of fibrinogen adsorbed on Si surfaces by FTIR, AFM and immunosorption**

Protein adsorption and changes in configuration are the primary interaction of a biological environment with foreign surfaces. Here Fourier Transform Infrared (FTIR) Imaging Spectroscopy, atomic force microscopy and specific enzyme linked immunosorption are used as three independent methods to analyze the fibrinogen adsorption in a model system on hydrophilic or hydrophobic Si surfaces, in order to work out the possibilities and limitations of these methods. Compared with the protein in solution, the amid I band of fibrinogen shifted by 7 $cm^{-1}$ when adsorbed on the more hydrophilic surface and by 9 $cm^{-1}$ on the more hydrophobic surface. In AFM the fibrinogen on the hydrophilic surface also appeared mainly in its native, elongated shape, whereas it was globular deformed on the hydrophobic surface. The configuration changes in the C-terminal region of the γ chain, which is detected by the antibody clone B4-2, were too discrete to be detectable on both surfaces; this was not the case with polystyrene as reference surface. On the base of these results the adsorption on different titanium oxide layers will be investigated.

**Collaboration:** [1]TU Dresden, Institut für Analytische Chemie, Dresden; [2]Akdeniz University, Antalya, Turkey

*M.V. Vinnichenko*[1]
*R. Gago*
*U. Kreissig*
*N. Huan*[2]
*M.P. Kulish*[1]
*M.F. Maitz*

**Spectroscopic ellipsometry investigation of amorphous carbon films with different $sp^3$ content: Relation to protein adsorption**

The albumin adsorption on non-hydrogenated amorphous carbon films with different diamond-like character (i.e. $sp^3$ content) was studied. The films were produced by ion beam assisted deposition and by filtered cathodic vacuum arc deposition to obtain a wide range of $sp^3$ contents. A combination of spectroscopic ellipsometry, Raman spectroscopy and ERDA was used to characterize the films. An increase of the deposition temperature up to 400°C leads to a decrease of the film band gap, its density, and a shift of the Raman G-band position with the main changes between 250°C and 300°C. The wettability of the film is not influenced by its $sp^3$ content, because the top surface layer in any case is mainly graphitic. For the same reason albumin adsorption on the surface also was independent of the $sp^3$ content. By an Ar ion irradiation of the layers the wettability could be increased and the amount of adsorbed proteins was reduced.

*Supported by INTAS and NSCF, China*

**Collaboration:** [1]Kyiv National Taras Shevchenko University, Kyiv, Ukraine; [2]Southwest Jiaotung University, Chengdu, China.

*I. Tsyganov*[1]
*M.F. Maitz*
*T. Migunova*[1]
*E. Malyshko*[1]
*E. Wieser*

**Titanium based coatings prepared by Metal Plasma Immersion Ion Implantation and Deposition (MePIIID) as hemocompatible surfaces**

Titanium based materials are known to be well hemocompatible, therefore they are suggested as coatings for blood contacting implants. Layers of pure Ti, Ti oxynitrides ($TiN_{1-x}O_x$ with x=0.25, 0.50, and 0.75) and Ti oxides were depo-

sited on oxidized Si from a plasma produced by cathodic arc evaporation under addition of $N_2$ and/or $O_2$ to the ambient near the substrate. The oxynitrides are crystalline with the fcc structure of TiN up to x = 0.25. For x = 0.5 a two phase system of fcc TiN and fcc TiO has been found. In dependence on the deposition parameters amorphous and crystalline layers (anatase + brookite, or rutile) of $TiO_2$ have been obtained. To study the correlation between structure of the coating and blood compatibility, the clotting time of blood plasma as well as the adhesion and activation of blood platelets on the surface were investigated. The clotting time on TiN and oxynitrides was longer than on rutile, which means that their clotting activation is lower. Minimum platelet adhesion was observed on pure $TiO_2$. Contrasting tendencies in the dependence of clotting time and platelet adhesion on the microstructure are observed.

*Supported by DAAD*

**Collaboration:** [1]Lipetsk State Technical University, Lipetsk, Russia

# Nanostructures

*T. Müller*
*K.-H. Heinig*

**Percolation of electron tunneling between Si nanocrystals synthesized in thin $SiO_2$ films by ion implantation**

The controlled fabrication of a narrow layer of Si nanocrystals (NCs) in thin $SiO_2$ films for multi-dot non-volatile memories (NC memories) is still a critical materials science issue. A NC density being as high as possible is required in order to achieve a substantial threshold voltage shift of the MOS transistor. On the other hand, the advantages of the NC memory like a good scalability and data retention are lost at too high NC densities. Then charge could spread over neighboring NCs by direct $e^-$ tunneling (i.e. due to electrical in-plane percolation paths). One single oxide defect could discharge several electrically percolated NCs. Studies on the synthesis of Si NCs by low energy $Si^+$ implantation into thin gate oxides of NC memories were performed. Using a kinetic 3D lattice Monte Carlo code, the nucleation, growth and Ostwald ripening of the Si NCs has been simulated. On the basis of these simulations, the dependence of the Si NC density, the distribution of the NC spacing as well as the threshold for extended electron tunneling paths were predicted. Thus, process conditions were identified, under which NCs align in a thin layer at high density but still at sufficient electrical isolation.

*Supported by EU*

*T. Müller*
*K.-H. Heinig*
*W. Möller*
*C. Bonafos*[1]
*H. Coffin*[1]
*N. Cherkashin*[1]
*G. Ben Assayag*[1]
*S. Schamm*[1]
*G. Zanchi*[1]
*A. Claverie*[1]
*M. Tencé*[2]
*C. Colliex*[2]

**Multi-dot floating-gates in MOSFETs for nonvolatile memories – their ion beam synthesis and morphology**

Theoretical and experimental studies on low-energy ion beam synthesis of multi-dot layers consisting of Si nanocrystals (NCs) have been performed. Kinetic Monte Carlo (KMC) simulations of phase separation of implanted Si from $SiO_2$ predict a strong fluence dependence of the morphology of the Si multi-dot floating gate layer. A pronounced transition from isolated, spherical Si NCs at low $Si^+$ to percolated spinodal Si patterns at high $Si^+$ fluences is predicted. This has been confirmed experimentally. Energy-filtered scanning TEM (EF-STEM) studies allowed to image Si precipitates buried in the $SiO_2$ which are not accessible by conventional TEM due to contrast problems. A remarkable agreement between elemental Si morphologies of KMC predictions and EF-STEM observations has been found. However, the predicted fluence critical for spinodal patterns is lower than the experimental ones. This discrepancy is attributed to parasitic oxidation of the implanted Si by ambient humidity which penetrates readily into as-implanted $SiO_2$.

*Supported by EU*

**Collaboration:** [1]CNRS/CEMES, Toulouse, France; [2]Laboratoire de Physique des Solides, Université Paris-Sud, Orsay, France

*K.-H. Heinig*
*T. Müller*
*L. Röntzsch*
*W. Möller*
*B. Schmidt*
*K.-H. Stegemann*[1]
*M. Fanciulli*[2]
*M. Perego*[2]

**Fabrication of Si nanocrystals in gate oxides by ion irradiation through an oxide buried under the poly-Si gate**

The ion-irradiation-induced formation of Si nanoclusters (NCs) in a thin $SiO_2$ layer sandwiched between the (001)Si substrate and a capping poly-Si layer is predicted by TRIDYN calculations and kinetic Monte Carlo (KMC) simulations. $Si^+$ ion irradiation causes mixing of the upper and lower $Si/SiO_2$ interface, i.e. $SiO_x$ regions form, and subsequent thermal treatment leads in the $SiO_x$ region to phase separation of Si excess from $SiO_2$. The phase separation in the former interface region proceeds via spinodal decomposition and results in a re-formation of the $Si/SiO_2$ interface, whereas the small Si excess in the more distant mixing tails separates via nucleation and growth, i.e. a Si nanocluster layer forms there. Predictive simulations were performed in order to optimize the Si NC formation process for multi-dot floating-gate non-volatile memory fabrication. Ion irradiation with $3x10^{15}$…$10x10^{15}$ $Si^+$ $cm^{-2}$ at 50…100 keV through 50 nm poly-Si and 8…15 nm $SiO_2$ on (001)Si results in a considerable

Si excess within the oxide, as predicted by TRIDYN. The electrical properties of the Si NC memory cell (low write/erase voltages due to tunnel distance of NCs from the $SiO_2$/Si interface, highest programming window) suggest a good agreement with their structure simulated by means of KMC simulations which predict optimal parameters for a fluence of $7x10^{15}$ $Si^+$ $cm^{-2}$ through a 15 nm thick buried $SiO_2$ layer resulting in a high Si NC area density.

*Supported by EU*

**Collaboration:** [1]ZMD AG, Dresden; [2]Laboratorio MDM-INFM, Agrate, Italy

*L. Röntzsch*
*K.-H. Heinig*
*B. Schmidt*

**Self-organization of nanocluster δ-layers in buried and thin $SiO_2$ layers after ion irradiation**

Experimental evidence is presented of a theoretical concept (see preceding contribution) which predicts the self-organization of δ-layers of Si nanoclusters (NCs) in the buried oxide of a MOS-like structure. This approach might be of eminent importance for a future generation of non-volatile flash memories based on gate oxides which contain Si NCs. Ion irradiation ($Si^+$, E = 50 keV, D = [$3x10^{15}$; $1x10^{16}$] $cm^{-2}$) through a layer stack of 50 nm poly-Si, 15 nm $SiO_2$, and the Si substrate leads to collisional mixing in the oxide. During thermal annealing, phase separation takes place in the course of which the Si-$SiO_2$ interfaces recover rapidly. Excess Si remaining in the oxide precipitates and – in a self-organizing manner – grows up to Si NC δ-layers which are ~3 nm apart from the Si-$SiO_2$ interfaces. Because of the very low mass contrast of Si NCs to the surrounding $SiO_2$ and their tininess, the Si NC δ-layer structure is outside the visibility limit of common XTEM. In order to enhance their mass contrast, a 5 nm thin Ge layer was inserted in between the 15 nm gate oxide and an 50 nm capping layer of $SiO_2$ which replaces the poly-Si. During ion irradiation, Ge atoms are mixed into the gate oxide. In the course of annealing, these Ge monomers diffuse through the oxide and attach to the growing Si precipitates due to the energetically favorable Si-Ge bond. Differently from δ-layers of pure Si NCs, the $Si_xGe_{1-x}$ NC δ-layer is now observable in XTEM because of the considerably enhanced mass contrast to the surrounding $SiO_2$. Without the presence of Si NCs no NC δ-layer is found at the position of interest. Consequently, the existence of Si NCs which align in a collective manner at a distinct distance of ~3 nm from the Si-$SiO_2$ interface was successfully proven.

*K-H. Stegemann*[1]
*E. Voitintseva*[1]
*P. Dimitrikas*[2]
*P. Normand*[2]
*B. Schmidt*
*K.-H. Heinig*
*T. Müller*
*L. Röntzsch*

**Memory properties of $Si^+$ irradiated poly-Si/$SiO_2$ gate stacks**

Memory properties n-MOSFET devices were investigated for different implantation and annealing conditions. The devices exhibit significant memory windows at low gate voltages. Devices with a memory window of about 0.1V for write/erase voltages of –7 V/+7 V and a programming time of $10^{-5}$ s were achieved. The memory window increases up to 0.6 V and 0.7 V for programming times of $10^{-2}$ s and $10^{-1}$ s, respectively. The memory properties of n-MOSFETs are similar to the ones measured on MOS capacitors indicating that the fabrication process is well controlled. In terms of memory window and transistor characteristics an implanted $Si^+$ dose of 5-$7x10^{15}$ $cm^{-2}$ and annealing at 1050°C for 30 s appear as the most promising conditions. Data retention tests were performed at temperatures of T = 25, 85, 105, 125 and 145°C. No degradation of the memory windows was observed for devices after $10^7$ write/erase cycles with +7 V/-7 V and $t_{pp}$ = 1 ms programming conditions. It was found that the data retention time is too low for EEPROM applications. For the wafers with highest implantation dose (D = $7x10^{15}$ $cm^{-2}$) a preliminary statistical analysis was performed. For each wafer the average threshold voltage, standard deviation and coefficient variation was calculated.

*Supported by EU*

**Collaboration:** [1]ZMD AG Dresden, [2] National Center for Scientific Research "DEMOKRITOS" Athens, Greece

*J. von Borany*
*V. Beyer*
*S. Ammous*[1]
*B. Schmidt*

**An RBS study of the Ge-loss in implanted $SiO_2$ films**

Contrary to Si nanocluster (NC) formation, the ion beam synthesis (IBS) of Ge nanoclusters in thin $SiO_2$ films is significantly influenced by surface chemistry effects, which result in, e.g., redistribution, oxidation, and out-diffusion. 1μm $SiO_2$ films were implanted with $^{74}Ge$ ions of various energies (1.5–12 keV) with peak Ge concentrations of 7 and 20 at%. Subsequently the samples were treated using different wet chemical cleaning and annealing (600–1000°C) procedures. In all cases, a Ge loss has been observed which increases significantly with the annealing budget. For ultra-shallow implants (1.5 keV, mean range $R_p$ = 4 nm), the Ge release is between 62 % (600°C, 10 min) and > 80 % (950°C, 10 min), but also for the deeper implant (12 keV, $R_p$ = 13 nm) about half of the Ge is lost after an annealing treatment at 950°C, 30 s. A very strong Ge loss has been obtained for shallow Ge implants ($R_p$ < 5 nm) already after standard Piranha treatment in which $H_2O_2$ acts as an etchant of Ge due to the formation of water soluble $GeO_2$. No remarkable differences are found for annealing in a neutral atmosphere (Ar, purity 9.0) and under high-vacuum conditions (< $5x10^{-6}$ mbar). Thus, all species ($H_2O$ or H, OH) responsible for the Ge loss during heat treatment (probably due to volatile $GeH_x$ or $GeO_x$) are incorporated into as-implanted oxide before annealing by absorption of moisture from ambient and water during wet chemical treatment.

*Supported by BMBF and DAAD*

**Collaboration:** [1] Jordan State University Amman, Jordan

*A.N. Trukhin*[1]
*J. Jansons*[1]
*H-J. Fitting*[2]
*T. Barfels*[2]
*B. Schmidt*

**Cathodoluminescence decay kinetics in $Ge^+$, $Si^+$, $O^+$ implanted $SiO_2$ layers**

Cathodoluminescence spectral shapes and respective decay times of red (1.85 eV), blue (2.7 eV) and UV (4.4 eV) bands show no similarity in the nature of luminescence centers in different crystalline and amorphous modifications of $SiO_2$ and $GeO_2$. On the other hand, the additionally produced red luminescence centers (650 nm) by oxygen implantation into $SiO_2$ layers are of the same nature as in stoichiometric $SiO_2$ and are attributed to the non-bridging oxygen hole center (NBOHC). Furthermore, the elevated blue luminescence (460 nm) in Si implanted $SiO_2$ belongs to the silicon related oxygen deficient center (SiODC) as in stoichiometric layers also. Ge implantation into $SiO_2$ and thermal post-annealing leads to a huge violet luminescence (400 nm) with a first rapid decay of $\tau$ = 24 ns followed by a slow hyperbolic decay with $t^{-0.15}$ to $t^{-0.54}$. The last 10% show again an exponential decay with a mean life time $\tau$ = 125 μs. This complex luminescent center is related to the GeODC center formed during the thermal treatment by Ge nanocluster formation.

**Collaboration:** [1]University of Latvia, Institute of Solid State Physics, Latvia; [2]Universität Rostock, Fachbereich Physik, Rostock

*K.-H. Heinig*
*T. Müller*

**Theoretical studies and atomistic simulations of nanowire growth and stability as well as synthesis of functional nanowire structures**

Theoretical studies and preliminary atomistic simulations have been performed to evaluate the potential of the ion beam synthesis and the Rayleigh instability for the fabrication of novel functional nanostructures based on nanowires. It has been shown that the reaction paths of nanowire evolution might be controlled in such a manner that (i) NC chains for light transport by surface plasmon-polaritons can be fabricated, (ii) multi-gate nanowire transistors and room-temperature single-electron transistors could be achieved, and (iii) magnetic pillars ("nanowires") for vertical magnetic recording can be formed.

*L. Bischoff*
*Ch. Akhmadaliev*
*G.L.R. Mair*[1]
*C.J. Aidinis*[1]

**The emission behaviour of a $Sn_{0.99}Pb_{0.01}$ and an $Au_{0.82}Si_{0.18}$ alloy LMIS**

Tin is very suitable metal for use in a liquid metal ion source (LMIS) configuration, due to its low melting point of 232°C, and low vapor pressure of $5.8x10^{-21}$ Pa at that temperature. The mass spectrum of a tin LMIS was studied

*C.A. Londos*[1]
*Th. Ganetsos*[1]
*A.W.R. Mair*[2]

in detail. $Sn^{++}$ was found to dominate in the beam both over $Sn^{+}$ and over cluster ions. For the relative intensities of $Sn^{+}$ and $Sn^{++}$, as a function of emission current, the conclusion is reached that both $Sn^{+}$ and $Sn^{++}$ are emitted as a result of direct field-evaporation from the liquid surface. Cluster ions form by ion impact-aided droplet disintegration. This source was stable running down to an emission current of 1 μA with an energy spread of 7 eV for the $Sn^{+}$ line. Secondly, the mass spectra of an $Au_{0.82}Si_{0.18}$ eutectic molten LMIS was investigated as a function of emitter temperature. It emerges that while $Au^{+}$, $Si^{+}$ and $Si^{++}$ are the result of direct field-evaporation from the liquid surface, $Au^{++}$ forms by the post-ionization of $Au^{+}$. Cluster ions are most probably the product of droplet break-up. Furthermore the energy distribution of the monomer ion species is studied as a function of emitter temperature. Secondary peaks, or shoulders, in the distribution of some of the species are explained in terms of Hornsey's model, which involves the fast movement of the jet in conjunction with a space-charge energy broadening mechanism within the beam.

*Supported by LSF*

**Collaboration:** [1]University of Athens, Department of Physics, Greece; [2]University of Manchester, Faculty of Science and Engineering, UK

*B. Schmidt*
*L. Bischoff*
*S. Oswald*[1]

**Self-aligned etch masking by $Ga^{+}$ implantation into silicon**

Silicon implanted with $Ga^{+}$ ions at 35 keV and 1-5x$10^{16}$ $cm^{-2}$ show a reduced Si etch rate during wet chemical etching (WCE) in $KOH/H_2O$ solution and during reactive ion etching (RIE) in $SF_6/O_2$ plasma. A still open question is the reason for this etch rate lowering. Therefore, the surface chemistry and the change of the Ga profile during WCE and RIE were studied by XPS and SIMS/RBS, respectively. XPS depth profiling as well as angle-resolved XPS showed that during WCE some monolayers of Ga-oxide are formed at the Si surface preventing the etching of (100)Si due to nonsolubility of Ga oxide in the etch solution. For the investigated etch times up to 5 min (corresponding to an etch depth in non-implanted Si of 5 μm) the Ga profile remains unchanged. In the case of RIE in $SF6/O_2$ plasma a thicker Ga oxide surface layer up to 10 nm is formed also reducing the etch rate. In contrast to WCE at RIE the Ga profile piles up at the surface indicating that Si is partially etched and that the Ga is transformed into the corresponding Ga oxide layer.

**Collaboration:** [1]Institut für Festkörper- und Werkstoffforschung Dresden

*S. Mucke*
*L. Bischoff*
*Ch. Akhmadaliev*
*H. Reuther*

**FIB aided metal-organic-CVD for nanostructure fabrication**

The new Orsay Physics FIB was used to optimise the deposition process of tungsten nanowires from the precursor tungsten-hexacarbonyl ($W(CO)_6$). Digital and analogue pattern generation was used to transfer the layout design onto Si or $SiO_2$ substrates. A crucial condition for the deposition is the balance between the gas molecule and the ion beam flux. Thus the pixel dwell time, refresh time and the current density were varied for the ion beam; for the gas only the heating temperature of the gas reservoir and the position of the injection nozzle could be adjusted. The strongest influence was found to be the pixel dwell time, which must be lower than 1 μs to minimize the sputtering. Wires as thin as 150 nm and up to 100 μm length were fabricated and analyzed by SEM and AES. The composition of the wires was determined to be 80% W, 6% C, 5% O from the cracked gas and 9% Ga from the ion beam for optimized process parameters. Furthermore, the electrical conductivity of such wires placed between two lithographic formed Al-stripes on $SiO_2$ was measured to be in the range from 150 to 300 μΩcm.

*L. Bischoff*
*I.W. Rangelov*[1]
*T. Ivanov*[1]
*S. Mucke*

**FIB modification of micromechanical cantilevers**

Micromachined thermally driven micromechanical cantilevers with a piezoresistive readout for micro- and nanorobotic systems and advanced high speed scanning probe microscopy were fabricated and characterized. The thermal

*B. Schmidt*

influence of the integrated microheater located at the cantilever end to the piezoresistive detector with respect to the beam motion should be investigated. Thus, the thermal conductivity through the lever was varied by FIB milling. Three different designs of ensembles of 2 x 6 $\mu m^2$ trenches were sputtered between heater and detector. For a precise adjustment of the FIB on the insulating $Si_3N_4$ or $SiO_2$ covered Si material of the cantilever a charge neutralization by a low energy electron shower was applied. In spite of a reduction of the cross section of the cantilever only a weak lowering of the heat propagation was found due to the high thermal conductivity of Si as well as a small decrease of the spring constant.

**Collaboration:** [1]Universität Kassel, Institut für Mikrotechnologie und Analytik, Kassel

*J. Grenzer[1]*
*U. Pietsch[1]*
*L. Bischoff*
*B. Köhler[2]*

**Depth resolved strain analysis of lateral nanostructures fabricated by FIB Ga implantation in GaAs**

A two dimensional dot lattice structure was studied which was produced in a GaAs (001) substrate using a $Ga^+$ focused ion beam with a diameter of less than 50 nm and a dose of $10^{14}$ $cm^{-2}$ at an energy of 30 keV. The fabricated 2D-lattice structure has a period of 200 nm in x and y direction with dots of almost circular shape with an area of about 100 $nm^2$. The whole implanted area has a size of less than 1 $mm^2$. Two samples were investigated. On sample A the implantation was performed normal to the sample surface, i.e. the beam penetrates parallel to the vertical lattice planes (channelling direction), whereas on sample B the implantation was performed 7° off to the surface normal tilted towards the [110] direction. We studied the strain distribution of the implanted samples by means of grazing-incidence XRD at the beamline ID-10B at the ESRF. Two symmetry equivalent in-plane reflections, the (220) and the (2-20) were measured at two different penetration depths for each sample. The average strain $\Delta a/a$ induced by the ion implantation was calculated. For sample A it amounts to -4 $x10^{-4}$ near the surface ( $\Lambda = 4$ nm) and decreases to -2 $x10^{-4}$ in the bulk ( $\Lambda = 400$ nm). For sample B we found an almost depth independent average strain of about -8 $x10^{-4}$. An additional line periodic structure between the expected X-ray pattern of the dot lattice aligned along the K direction was found. This behavior appeared in sample B and can be attributed to a different (in comparison with sample A) interaction of the implanted ions with the host lattice.

**Collaboration:** [1]University of Potsdam, Institute of Physics, [2] FhG, EADQ Dresden

*J. Seidel[1]*
*S. Grafström[1]*
*L. Eng[1]*
*F.I. Baida[2]*
*D. Van Labeke[2]*
*B. Guizal[2]*
*L. Bischoff*

**Coupling between surface plasmon modes on metal films**

Using scanning near-field optical microscopy for probing surface plasmon fields, we show that energy can be transferred from the plasmon propagating on one interface to the mode bound to the other interface. This coupling is mediated by a narrow groove interrupting the silver film, fabricated using the improved IMSA system equipped with the high-resolution ion-optical column CANION 31Mplus (Orsay Physics). The excitation of the second plasmon mode is detected by mapping the spatial intensity modulation induced by the interfering fields of the two plasmons. A quantitative analysis provides detailed knowledge about the degree of coupling. Our interpretation of the experimental results is confirmed by a numerical simulation of the field distribution.

**Collaboration:** [1]TU Dresden, Institut für Angewandte Physik, Dresden; [2]Universite de Franche-Comte, Besancon, France

*A.V. Dvurechenskii[1]*
*J.V. Smagina[1]*
*R. Grötzschel*
*V.A. Zinovyev[1]*

**Ge/Si quantum dot nanostructures grown with low energy ion-beam assisted epitaxy**

The density, size distribution and shape of Ge nanoislands on Si can be tuned by low energy (100 – 200 eV) ion beam assistance during epitaxial growth. By

*P.L. Novikov*[1]
*S.A. Teys*[1]
*A.K. Gutakovskii*[1]

a subsequent epitaxial growth of Si as a capping layer, nanostructures with a high density of quantum dots of a small size can be produced for, e.g., electronic devices based on quantum effects, operating at room temperature. For the Ge epitaxy, MBE was used in combination with a Ge ion source specially developed for low energies. During MBE growth Ge ion beam pulses were applied after the completion of each monolayer. RHEED, STM, TEM and RBS were used as complementary techniques to study the obtained nanostructures. The low-energy ion irradiation results in a narrower size distribution compared with conventional MBE, and with increasing ion energy it stimulates the island shape transition from "hut" to "dome" islands. Defect-free nanostructures with Ge quantum dot densities up to $10^{12}$ $cm^{-2}$ and an average size of 10 nm were grown.

**Collaboration:** [1]Institute of Semiconductor Physics, Novosibirsk, Russia

*F. Eichhorn*
*R. Fromknecht*[1]

**XRD studies of Au nanocrystals in rutile $TiO_2$ (001) formed by ion implantation and thermal annealing**

Besides promising applications for electronic nanostructures or nonlinear optical devices nanocrystalline Au may be used as efficient catalysis material (e.g. chemisorption of CO or hydrocarbons). The catalytic reaction is often very sensitive to the structure and size of the metal crystallites which may be controlled by growing the nanocrystals in a single crystalline non-metallic matrix. $8.5x10^{16}$ $cm^{-2}$ Au ions were implanted with an energy of 260 keV into rutile (001) oriented $TiO_2$ crystals. In the as-implanted state both randomly oriented crystals with a size of 7 nm and crystals oriented in a fibre texture with <110> axis parallel to the rutile [001] axis have been obtained. Due to annealing (770°C, 30 min) the randomly oriented crystals grow to 14 nm, and an increasing part of Au nanocrystals is highly oriented to the $TiO_2$ lattice: Au <110> || $TiO_2$ <001>. In the azimuthal direction there exist two sub-groups rotated by +9.7° and –9.7° around the surface normal from the "ideal" orientation: Au <110> + 9.7° and –9.7° || $TiO_2$ <110 > and Au <100 > + 9.7° and –9.7° || $TiO_2$ <110>.

**Collaboration**: [1]Forschungszentrum Karlsruhe, Institut für Festkörperphysik

# Doping and Defects in Semiconductors

*M. Smith*[1]
*R. McMahon*[1]
*M. Voelskow*
*J. Stoemenos*[2]
*D. Panknin*
*W. Skorupa*

**Flash lamp supported deposition of 3C-SiC (FLASiC) - modelling and regrowth mechanism**

Flash lamp annealing has been shown to be effective in annealing SiC layers on silicon substrates. In this FLASiC process, the silicon below the SiC layer is transiently melted by an intense pulse of light lasting about 20 ms. As the extent and duration of the melt depend on both the parameters of the flash lamp process and the structure of the substrates, a thermal model has been developed to enable studying the effect of these variables. The model is a numerical solution of the enthalpy equation, using a modified implicit Crank-Nicholson scheme to combine accurate prediction of melt depths with reasonable computation times. The model has been calibrated against experiments and then used to compute temperature profiles. The results show the time and extent of melting as a function of layer thickness, wafer preheat temperature, and pulse intensity and duration. The evolution of the temperatures at the front, middle and back of the wafers are given. The availability of the temperature profiles enables one to study the underlying mechanisms of flash lamp annealing. In particular, the kinetics of the regrowth and the diffusion of carbon in the melt zone are addressed.

*Supported by EU*

**Collaboration:** [1]University of Cambridge, UK, [2]Aristotele University of Thessaloniki, Greece

*D. Panknin*
*W. Anwand*
*M. Voelskow*
*J. Stoemenos*[1]
*G. Ferro*[2]
*J. Pezoldt*[3]
*W. Skorupa*

**Flash lamp supported deposition of 3C-SiC on (100)-Si (FLASiC)**

The epitaxial deposition of good quality 3C-SiC on Si requires maximum crystallographic perfection of the seed layer during the early stage of the growth process. Due to the lattice misfit of about 20% between Si-bulk and 3C-SiC this perfection is usually not obtained. The patented FLASiC technology was developed including (i) the deposition of a thin SiC layer (< 100 nm) (ii) flash lamp processing to anneal this layer (iii) epitaxial deposition of thick SiC using the annealed thin SiC layer as seed for the growth of good quality 3C-SiC. The available flash lamp equipment was reconstructed for the specific annealing conditions of the FLASiC technology. The irradiation parameters (preheating temperature, flash energy density) were optimised. The improvement of the quality of the seed, the development of a new flash lamp annealing apparatus and the production of device demonstrators are the most important features of the future work.

*Supported by EU*

**Collaboration:** [1]Aristotle University Thessaloniki, Physics Department, Greece; [2]University Claude Bernard Lyon, France, [3]Technische Universität Ilmenau

*G. Ferro*[1]
*D. Panknin*
*J. Stoemenos*[2]
*W. Skorupa*

**Formation of thick 3C-SiC films using the FLASiC process**

A first experiment was carried out to produce a 3µm thick 3C-SiC film using the FLASiC technology. A three-step process was developed for the formation of thick 3C-SiC layers: firstly a 35 nm thick 3C-SiC film on a (100)-Si substrate is deposited followed, secondly, by flash lamp annealing. The flash energy is mainly absorbed at the highly defected interface. If the irradiated energy density is sufficiently high, a rapid melting of the Si near the interface region is obtained. Due to the contact with the melted Si the neighbouring SiC dissolves. During the following epitaxial solidification process a phase separation occurs, resulting in a recrystallized Si and SiC interface. In a third step, this film is used as a seed for deposition of a 3 µm thick 3C-SiC layer. Compared to the non-flashed SiC layers the thick FLASiC SiC films show a distinctly lower defect density, which is closely related to the quality of the SiC seed.

*Supported by EU*

**Collaboration:**[1]University Claude Bernard Lyon, France; [2]Aristotle University Thessaloniki, Physics Department, Greece

*M. Posselt*
*F. Gao*[1]
*W.J. Weber*[1]
*V. Belko*[2]

**Comparative study of structure and energetics of elementary defects in 3C- and 4H-SiC**

The potential non-equivalent defects in both 3C- and 4H-SiC were classified by a new method that is based on symmetry considerations. In 4H-SiC their number is considerably higher than in 3C-SiC, since the hexagonal symmetry leads to diversification. The different theoretical methods hitherto used to investigate defects in 3C-SiC were critically reviewed. Classical MD simulations with a recently developed interatomic potential were employed to investigate the stability, structure and energetics of the large number of non-equivalent defects that may exist in 4H-SiC. Most of the potential defect configurations in 4H-SiC were found to be stable. The interstitials between hexagonal and trigonal rings, which do not exist in 3C-SiC, are characteristic for 4H-SiC and other hexagonal polytypes. The structure and energetics of some complex and anisotropic dumbbells depend strongly on the polytype. On the other hand, polytypism does not have a significant influence on the properties of the more compact and isotropic defects, such as vacancies, antisites, hexagonal interstitials, and many dumbbells. The results allow conclusions about the energy hierarchy of the defects.

**Collaboration:** [1]Pacific Northwest National Laboratory, Richland, USA; [2]Belarus State University, Minsk, Belarus

*V. Belko*[1]
*M. Posselt*
*E. Chagarov*

**Improvement of the repulsive part of the classical interatomic potential for SiC**

In order to enable a better description of ballistic and athermal processes occurring in the initial stage of ion-beam-induced defect formation, the repulsive part of the interatomic potentials of Gao and Tersoff was improved. The first modification concerns the two-body part of the potentials. At small interatomic distances it was replaced by the well-tested potential of Ziegler, Biersack, and Littmark (ZBL). For repulsive interactions between zero and some ten electron volt, an exponential spline function was employed to connect the ZBL potential with the two-body parts of the Tersoff and the Gao potential. The modified potentials are in good agreement with data obtained by density-functional-theory calculations. Furthermore, the three-body part of the Tersoff and the Gao potential was modified in order to avoid the strong dependence of repulsive interactions between two atoms on the bond-order parameter, i.e. on their coordinations. The modifications were performed in such a manner that the total potential and its first derivative remain continuous and monotonic for all repulsive interactions.

**Collaboration:** [1]Belarus State University, Minsk, Belarus

*V. Heera*
*A. Mücklich*
*C. Dubois*[1]
*M. Voelskow*
*W. Skorupa*

**Layer morphology and Al implant profiles after annealing of supersaturated single crystalline, amorphous and nanocrystalline SiC**

Al supersaturated SiC layers ($5x10^{20}$ Al $cm^{-3}$) were produced by multi-energy, high dose ion implantation into 6H- and 4H-SiC. Several implantation schemes with varying implantation sequence and temperature were investigated. Depending on the implantation conditions damaged single-crystalline, amorphous or nanocrystalline layers were formed. The layer morphology and Al distribution in the as-implanted state as well as structural changes and the related Al redistribution after high-temperature annealing (1500-1700°C) were characterized by XTEM, RBS/C, AFM and SIMS analysis. Remarkable Al redistribution effects were found after annealing of Al supersaturated SiC. During high temperature annealing Al atoms in excess to the solid solubility ($2x10^{20}$ Al $cm^{-3}$) tend to precipitate in single-crystalline SiC, whereas they diffuse out in amorphous or nanocrystalline SiC. Al with a concentration below the solid solubility remains almost immobile in SiC independent of the layer morphology. Amorphization of SiC is advantageous in the case of Al doping to levels higher than

the solid solubility, because it prevents Al precipitation during annealing and helps to form box-like Al profiles with a smooth plateau and abrupt edge.

*Supported by DFG*

**Collaboration:** [1]INSA Lyon, France

*G. Brauer*
*S. Brandstetter[1]*
*C. Teichert[1]*
*W. Anwand*
*W. Skorupa*

**SPIS and AFM characterization of 6H-SiC surfaces after ion implantation and annealing**

Recently it was found by SPIS that n-type 6H-SiC co-implanted at 800°C by $Al^+$ and $N^+$ and subsequently annealed at 1650°C shows the presence of a sub-surface layer containing rather large Si-C divacancy clusters. This motivated the present surface morphology study of ion implanted 6H-SiC substrates and epi-layers. First AFM results did not give direct evidence of any influence of these clusters on the surface morphology, but revealed instead the formation of periodic step bunches. On the terraces in-between, stripe-like islands with a discrete height in the nanometer range were observed. More systematic AFM studies of various 6H-SiC samples were conducted in order to separate the influences of conductivity type, crystal quality, ion implantation ($B^+$, $Al^+$, $N^+$), and annealing (1650°C, 10 min) on the observed changes in surface morphology. In addition, all samples were characterized by SPIS.

**Collaboration:** [1]Institut für Physik, Montanuniversität Leoben, Austria

*W. Anwand*
*G. Brauer*
*W. Skorupa*
*J. Kuriplach[1]*

**SPIS investigations of defects caused by $B^+$ implantation into epitaxial 6H-SiC**

For $B^+$ implantation (120 keV, $1x10^{16}$ $cm^{-2}$, 400°C) into epitaxial 6H-SiC TRIM predicts an increasing defect concentration from the surface to a depth of about 230 nm where a maximum is reached, and no defects should be formed deeper than 320 nm. In contrast, SPIS reveals a damaged layer of 230 nm thickness only with homogeneously distributed defects clusters (3–4 Si-C-divacancies / defect). This discrepancy is attributed to the relatively low substrate temperature of 400°C during implantation. The vacancy-type damage formed is completely annealed by a heat treatment at 1650°C (10 min) in Ar atmosphere. However, the formation of B precipitates is indicated. From positron affinity calculations it may be concluded that these B precipitates have a radius $\geq \sim 0.17$ nm.

**Collaboration:** [1]Charles University Prague, Czech Republic

*J. Ristic[1]*
*A. Sanchez-Garzia[1]*
*E. Calleja[1]*
*A. Perez-Rodriguez[2]*
*C. Serre[2]*
*A. Romano-Rodriguez[2]*
*J,R. Morante[2]*
*R. Kögler*
*W. Skorupa*

**Growth of GaN layers on ion beam synthesized SiC layers**

High quality GaN layers were grown by molecular beam epitaxy, with and without AlN buffer on ion beam synthesized SiC layers in Si. Ion beam synthesis of such buried layers was performed by multiple C implantation at 500°C into (111) Si substrate and subsequent thermal treatment at 1150°C for 6 h in $N_2$. The Si top layer and the non-stoichiometric interface region above the SiC layer were removed by TMAH (tetramethyl ammonium hydroxide) etching and reactive ion etching using a $SF_6$:$O_2$ gas mixture. XRD analysis revealed that the SiC layer was not perfectly monocrystalline. Despite the lack of a perfect SiC surface GaN layers of high quality could be grown which consist of microcrystals with tensile strain.

*Supported by WTZ*

**Collaboration:** [1]University of Madrid, [2]University of Barcelona, Spain

*H. Weishart*
*V. Heera*
*F. Eichhorn*
*W. Skorupa*
*B. Pécz[1]*
*A. Barna[1]*

**High-fluence Si-implanted diamond: Influence of implantation temperature**

The effect of implantation temperature on the structural properties of diamond implanted with high fluences of Si was investigated. In order to reduce radiation-induced damage and to enhance formation of the new SiC-phase the implantations were performed at elevated temperatures in the range between 900 - 1200°C. Subsequently, all samples were annealed for 10 min at 1500°C in an rf-heated furnace. Raman spectroscopy was employed to analyze radiation-damage-induced graphitization of the surface. XRD revealed the crystallogra-

phic structure of the samples and XTEM showed their structure on a nanometer scale. A buried layer of cubic SiC nanocrystals forms inside the implanted diamond. Increasing the Si fluence at a fixed implantation temperature increases the implantation-induced damage, and the alignment of the formed SiC crystallites within the host diamond lattice deteriorates. Raising the implantation temperature at a fixed fluence reduces the damage in the diamond and increases amount, size and epitaxial alignment of the crystalline SiC precipitates. However, for each fluence there exists a critical implantation temperature, above which a conversion of the diamond into graphite starts and the formation of SiC crystallites is obstructed.

*Supported by DFG*

**Collaboration**: [1]Research Institute for Technical Physics and Materials Science, Budapest, Hungary

*H. Weishart*
*V. Heera*
*W. Skorupa*

**Hall measurement of N- and Si-implanted diamond**

Natural IIa-type diamond was implanted at 900°C with N (90 keV) to a fluence of $1x10^{15}$ $N^+$ $cm^{-2}$ and with Si (150 keV) to a fluence of $5.5x10^{17}$ $Si^+$ $cm^{-2}$. These implantation parameters yield a 200 nm thick buried layer of SiC-nanocrystals with a mean N-concentration of $5x10^{19}$ $cm^{-3}$. Four contacts were applied to the sample by local graphitization of the diamond using N-implantation at RT through a mask. Subsequently the sample was annealed at 1500°C for 10 min in pure Ar. Hall measurements were performed in the temperature range between 110 K and 820 K. The sample shows a high n-type conductivity. The electron concentration increases from $7x10^{19}cm^{-3}$ at 110 K up to more than $1x10^{20}cm^{-3}$ at 820 K. This exceptional high electron concentration may originate from implantation-induced electrically active defects as well as additional unintentionally co-implanted $^{28}N_2$ Assuming that these two mechanisms (activated N-donors and electrically active defects within the bandgap) independently contribute to the conductivity, the temperature dependence can be fitted using a homogenous medium model. The electrically active N-concentration of $1.3x10^{20}$ $cm^{-3}$ determined with this model supports the hypothesis of unintentionally co-implanted nitrogen molecules. The Hall mobility is found to be approx. 3 $cm^2/Vs$ with only a weak temperature dependence.

*Supported by DFG*

*R. Kögler*
*A. Peeva*
*A. Lebedev*
*M. Posselt*
*W. Skorupa*
*M. Behar*[1]

**Cu gettering in silicon implanted with P ions in random and channelling direction**

Damage generation in P-implanted silicon was experimentally investigated by Cu decoration of the defects and theoretically by Crystal-TRIM simulations. The results showed that the gettering centres for Cu are formed in regions with either an excess of interstitials (at $R_P$) or an excess of vacancies (around $R_P/2$). In both cases for random and channelling ion incidence only two Cu peaks were observed after rapid annealing at 900°C for 30 s just at $R_P/2$ and $R_P$ in good agreement with the calculated distribution of excess defects. For channelling ion implantation, both Cu peaks and the corresponding excess defects were shifted a certain distance toward a larger depth. The third Cu peak observed beyond $R_P$ (trans-$R_P$) in P-implanted silicon after long term annealing was found not to be a consequence of fractional ion channelling during implantation. Instead the gettering centres of this Cu peak are formed by defect diffusion and damage annealing. Their detailed structure is not yet known.

*Supported by DFG*

**Collaboration:** [1]UFRGS Porto Alegre, RS, Brasil

*H. Bracht*[1]
*J. Fage Pedersen*[2]
*N. Zangenberg*[2]
*A. Nylandsted-Larsen*[2]
*E.E. Haller*[3]

**Radiation enhanced silicon self-diffusion and the silicon vacancy at high temperatures**

Proton radiation enhanced self-diffusion (RESD) in Si-isotope heterostructures was investigated. Self-diffusion experiments under irradiation were performed at temperatures between 780°C and 872°C for various times and proton fluxes. Detailed modeling of RESD provides direct evidence that vacancies diffuse at

*G. Lulli*[4]
*M. Posselt*

high temperatures with a migration enthalpy of $H_V^m$ = (1.8±0.5) eV, significantly more slowly than expected from their diffusion at low temperatures, which is described by $H_V^m < 0.5$ eV. It is concluded that this diffusion behavior is a consequence of the microscopic configuration of the vacancy which influences both entropy and enthalpy of migration.

**Collaboration:** [1]Universität Münster; [2]University of Aarhus, Denmark, [3]University of California and Lawrence Berkeley National Laboratory, USA, [4]CNR-IMM Bologna, Italy

*A. Lebedev*

**Development of the Crystal-TRIM module of the process simulator FLOOPS-ISE**

The next generation process simulator tool FLOOPS-ISE includes now Crystal-TRIM as its primary Monte-Carlo implantation engine. Due to the latest requirements of industry, novel device geometries as well as new target materials have to be considered for process simulation. Crystal-TRIM capabilities have been extended to simulate ion implantation in truly three-dimensional structures. The model description of crystalline target materials in Crystal-TRIM has been generalized, so that a simulation of ion implantation into arbitrary semiconductors with zincblende structure is possible now. The composition of the target material may be either homogeneous or the result of previous processing steps (e.g. SiGe can be treated as a single-crystalline silicon with a varying fraction of incorporated Ge atoms).

*Supported by ISE*

**Collaboration:** Integrated Systems Engineering (ISE) AG, Zürich, Switzerland

*J. von Borany*
*M. Friedrich*
*M. Rüb*[1]
*G. Deboy*[2]
*J. Butschke*[3]
*F. Letzkus*[3]

**Application of ultra-high energy boron implantation for superjunction power (CoolMOS®) devices**

Superjunction devices (SJDs) are a relatively novel class of power devices which break the physical limit of silicon with respect to the area specific turn-on-resistance. SJDs consist of a modified vertical MOSFET structure which is characterized by additional deep pillar-like p-type doped regions formed inside the $n^{(-)}$ epi-layer below the gate. Charge compensation between p- and n-type regions enables a reduction of the on-resistance up to a factor of 10 without a loss in blocking capability. Present commercial fabrication technology is based on a multistep epitaxy and low energy implantation process sequence. Alternatively, ultra-high energy boron ion implantation has been applied using the 5 MV Tandem accelerator at the FZR. Multi-energy boron implantation (2-25 MeV, total dose ~ $10^{13}$ $cm^{-2}$) was performed to create deep p-regions up to 30 µm depth with a nearly homogeneous concentration of 1-3x$10^{16}$ B/$cm^3$. For laterally structured implantations micromechanically fabricated Si stencilmasks were used. Due to the small openings (2-6 µm) and the high aspect ratio (up to 20:1) of the mask structures the implantation was carried out at an angle of (0° ± 1°) to avoid shadowing effects. For energies above 10 MeV the incident ions exceed the Coulomb barrier for Si which lead (i) to a significant gamma and neutron emission during implantation (~ 1 mSv/h) and, (ii) an activation of the wafer and the mask material. Fortunately, the most relevant reaction ($^{11}B+^{28}Si \rightarrow n\alpha + ^{34m}Cl \rightarrow {}^{34}S+\beta$) has a half-life of only 32 min so that the radiation level of the wafers drop below the radiation protection limit (<10 µSv/h) if the implantation is performed in a sequence from high to low energies. Based on this technology Infineon Technologies successfully prepared a set of prototype wafers with fully functional high-voltage transistors. Typical blocking capability was in the range of 500 V with an on-state resistance of about 185 mΩ.

*Supported by BMBF*

**Collaboration:** [1]Infineon Technologies Austria AG, Villach, Austria; [2]Infineon Technologies AG, München; [3]Institut für Mikroelektronik Stuttgart

*A. Nazarov*[1]
*W. Skorupa*
*I.N. Osiyuk*[1]
*I.P. Tjagulskii*[1]
*V.S. Lysenko*[1]
*R.A. Yankov*[2]
*T. Gebel*[2]

**Charge Trapping in High-Dose Si or Ge-Implanted Al/$SiO_2$/Si Structures**

Negative and positive charge trapping in Si-implanted $SiO_2$ layers of Al/$SiO_2$/Si-based devices was studied during high-field electron injection from the Si substrate under conditions typically used for obtaining the well documented blue-violet EL. The location, capture cross-section and concentration of negatively and positively charged traps were determined as a function of the time of heat treatment by RTA. A comparison between the results obtained from Si- and Ge-implanted oxide layers showed that in the case of Si-rich oxides an increase in the RTA time (6-150 sec) leads to the formation of hole and electron traps of high concentration, both of which are located within the oxide. For Ge-rich oxide layers, however, the hole traps are found primarily in the vicinity of the $SiO_2$/Si interface while the electron traps are present within the oxide.

*Supported by WTZ*

**Collaboration:** [1]Institute of Semiconductor Physics, NASU, Kyiv, Ukraine; [2]nanoparc GmbH, Dresden

# Optoelectronic Materials

*A. Dreyhaupt*
*S. Winnerl*
*T. Dekorsy*
*M. Helm*

**Time-domain THz spectroscopy of electronic exitations in GaAs/AlGaAs superlattices**

The electronic properties of a weakly coupled n-doped GaAs/AlGaAs superlattice by time-domain THz spectroscopy in the low energy range from 0.5 to 3.5 THz have been investigated. THz transmission spectra are recorded by modulating the carrier density in the superlattice with an AC bias voltage at a gate electrode. The transmission signal is detected at the frequency of the modulation voltage by a lock-in amplifier leading to a signal-to-noise ratio superior compared to conventional FTIR spectroscopy in this frequency range. The spectra reveal the existence of electronic transitions between minibands and donor states and the existence of plasmons. The features are assigned to the effects by their energies and temperature dependence. Our experiments expand the insight gained previously from experiments with Fourier-transform spectrometers. Further on we prepared experiments with more strongly coupled superlattices in order to investigate the possibility to obtain THz gain from such devices. The mesa size dependent appearance of negative differential conductivity was investigated.

*S. Winnerl*
*T. Dekorsy*
*M. Helm*

**THz emission from GaSb samples with non-stochiometric surfaces**

The optimization of emitters for THz radiation pulses has gained a lot of interest in recent years. They can be based on accelerating charge carriers, which are photoexcited by fs-laser pulses in the surface field of a semiconductor. The surface field is due to pinning of the Fermi level caused by surface states in the band gap. We studied the THz emission from GaSb samples that were annealed at different temperatures in the range from 300 to 700°C. Without annealing, no THz emission was observed under fs excitation at 800 nm. This is consistent with the fact that for GaSb no surface states in the band gap have been found. We observed that with increasing annealing temperature the THz emission increased, reached a maximum for the annealing temperature 450°C, and decreased for higher annealing temperatures. The amplitudes of the THz field were comparable to the fields from an InGaAs emitter. We attribute the THz emission to a surface field caused by decomposition of the surface of the annealed samples. The decomposition is confirmed by measuring the surface stoichiometry using AES. We suggest that the decrease of THz intensity for the higher annealing temperatures is due to a lowering of the carrier mobility. Our experiment demonstrates the possibility to modify materials for THz emission in a very simple way.

*N. Georgiev*
*T. Dekorsy*
*M. Helm*
*M. Ziegler*[1]
*M.P. Semtsiv*[1]
*S. Dreßler*[1]
*W.T. Masselink*[1]

**Strain-compensated quantum cascade laser operating at room temperature**

Since the invention of quantum cascade lasers (QCL) ten years ago these infrared emitters have undergone a rapid development. So far, QC lasers with wavelengths from 3.4 to 17 μm have been fabricated in the InGaAs/InAlAs material system. The shortest wavelength operation of a QCL is limited by the conduction band offset, $\Delta E_c$, between the well and barrier materials. For InGaAs/InAlAs grown lattice-matched on InP ($\Delta E_c$=0.52 eV), lasers with wavelengths >4.3 μm have been realized. To achieve QCL with $\lambda < 4$ μm, strain-compensated $In_xGa_{1-x}As$/ $In_yAl_{1-y}As$ ($x>0.53$ and $y<0.52$) has to be used, since it provides a larger $\Delta E_c$. Using strain-compensated InGaAs/InAlAs grown on InP the QCL with the shortest wavelength of 3.4 μm was demonstrated. However, the maximum operating temperature and output power of this QCL were inferior compared to the corresponding lattice-matched devices. Using a strain-compensated $In_{0.73}Ga_{0.27}As/AlAs/In_{0.55}Al_{0.45}As$ structure on InP,

we demonstrate a QCL operating at room temperature in the range of 3.9 – 4.2 μm, with a low-temperature peak power of several W and a threshold current density of only 1.2 kA/cm$^2$.

*Supported by DFG*

**Collaboration:** [1]Humboldt-Universität Berlin, Fachbereich Physik, Berlin

*N.Georgiev*
*T. Dekorsy*
*M. Helm*
*M. Semtsiv*[1]
*W.T. Masselink*[1]

**Near infrared intersubband transitions in InGaAs-AlAs-InAlAs double quantum wells**

Intersubband transitions (ISBT) in quantum wells (QW) are attractive for applications as all-optical modulators and switches due to their ultrafast relaxation, large dipole moment, and widely tuneable transition wavelength. An ultrafast all-optical switch is one of the crucial devices for future ultrahigh-bit-rate optical time-division multiplexed communication systems. For this application, ISBT in InGaAs/AlAs QWs grown strain-compensated on an InP substrate are promising because of their large conduction band offset of 1.1-1.3 eV. However, for near-infrared wavelengths shorter than 2 μm, QWs with thickness as small as 5-7 monolayers are required. This leads to a significant carrier leakage due to the overlap of the ground state in the well and the X-band of the barrier layer which deteriorates the ISBT in InGaAs/AlAs single QW structures. We have designed asymmetric couple double QW structures in order to realize ISBT in the telecommunication wavelength by utilizing the splitting of the overlapping bands in the coupled quantum wells. Absorption peaks are observed over a broad wavelength range covering 1.55 μm, which originate from transitions between different subbands. The investigated structures consist of a wide $In_{0.7}Ga_{0.3}As$ well (widths 2.4 nm, 2.6 nm, and 2.8 nm) and a broader well of 3.2 nm, coupled by a 0.9 nm central AlAs barrier.

*Supported by DFG*

**Collaboration:** [1]Humboldt-Universität Berlin, Fachbereich Physik, Berlin

*N. Georgiev*
*T. Dekorsy*
*M. Helm*
*K. Biermann*[1]
*H. Künzel*[1]

**Intersubband transitions in InGaAs/AlAsSb quantum well structures: Towards short-wavelength quantum cascade lasers**

Intersubband transitions in semiconductor quantum wells have been attracting much attention in various infrared optoelectronic device applications such as lasers, detectors, ultrafast all-optical modulators and switches. For realizing devices that can be employed at wavelengths <2 μm, large conduction band offsets (> 1 eV) are required, which are e.g. offered by the InGaAs/ AlAsSb heterosystem, lattice matched to InP substrates. In multi-quantum wells based on this system we observed strong intersubband absorption at wavelengths between 2 and 4 μm, depending on the well thickness. Based on these results, a quantum cascade emitter structure designed for a wavelength of 3 μm was grown. A first characterization by XRD is encouraging, but the crucial test will be forthcoming measurements of the photocurrent and electroluminescence.

*Supported by DFG*

**Collaboration:** [1]Fraunhofer Institut Nachrichtentechnik, Heinrich-Hertz-Institut, Berlin

*S. Sinning*
*T. Dekorsy*
*M. Helm*
*G. Mußler*[1]

**Time resolved investigations of nitrogen containing GaAs**

Nitrogen containing III-V-semiconductors have attracted considerable interest over the past few years due to their unique electronic properties and their potential for optoelectronic applications. While MBE growth of GaNAs is well established, ion implantation has been less explored for the synthesis of GaNAs. We investigated the ultrafast carrier dynamics of pure GaAs and ion-implanted GaNAs with a nitrogen content smaller than 4%. The samples were prepared by $^{14}N^+$ implantation with different energies (30 keV to 300 keV) in order to achieve a homogeneous nitrogen profile over 800 nm. In addition samples were implanted at temperatures up to 400°C to minimize damage production. Subsequently the samples were annealed by rapid thermal annealing. From photoreflectance measurements we conclude that the highest achieved

active nitrogen content in the implanted samples is 0.5% for an equivalent implantation dose of 1%. Carrier dynamics are investigated by one-colour pump-probe measurements in reflection geometry covering a wide excitation wavelength range from 720 to 870 nm (1.7 to 1.42 eV). The carrier relaxation in the implanted samples is found to be trap dominated. The results are interpreted based on rate equations simulating carrier dynamics by using the band-anticrossing model for the conduction band.
**Collaboration:** [1]Paul-Drude Institut für Festkörperelektronik, Berlin

*J. Sun*
*T. Dekorsy*
*W. Skorupa*
*B. Schmidt*
*M. Helm*

**The importance of excitonic traps for efficient silicon light-emitting diodes prepared by ion implantation**

Efficient EL with power efficiency up to 0.12 % was observed from silicon pn diode prepared by boron implantation. Two electroluminescence bands with maxima around 1.05 eV and 0.95 eV are observed at low temperature in silicon pn diodes prepared by high-dose boron implantation into n-type silicon and subsequent high-temperature annealing. The temperature dependences of bound excitons and band-edge electron-hole recombination are studied for pn diode implanted with different boron doses. The temperature dependences of the different peaks can be very well calculated with a rate equation theory taking into account the transition between the bound excitons and free electron-hole pairs. The theoretical calculation indicated that the bound excitons have a strong capture rate plus a very low recombination rate in the high-dose boron implanted diode as compared to the normal diodes with a low boron concentration. Therefore the excitonic traps, as a sink of electron-hole pairs at low temperature, can effectively enhance the band-edge radiative recombination in silicon pn diode by emitting free electron-hole pairs at elevated temperature. The consistency between theory and experiment suggests a new way for making efficient light-emitting pn diodes by introducing localized highly-doped spikes by dopant ion implantation as a source of spatially indirect bound excitons near the pn junction of a semiconductor diode.

*F. Aquistapace*[1]
*J.L. Coutaz*[1]
*T. Dekorsy*

**Fabrication and characterization of THz photomixers for 1.55 µm wavelength**

The generation of continuous THz waves by optical beating of two CW laser beams requires a nonlinear mixing material. In the past, low-temperature grown GaAs photoswitches exhibiting sub-picosecond carrier lifetimes have been used for mixing of laser diodes at 0.8 µm. High-power fiber lasers operating around 1.55 µm would provide an ideal laser source for photomixing. However, low-temperature grown GaAs does not work in this wavelength range due to its large bandgap. Hence ultrafast materials are required with band-gap energies below 0.8 eV. Since low temperature growth of InGaAs do not yield high resisitivity material with ultrafast carrier lifetimes, we investigated $As^+$ ion implantation of InGaAs grown lattice matched on InP. Multiple-energy $As^+$ implantation and subsequent thermal annealing was performed to achieve 0.3%, 0.6% and 1% excess As. For 0.3% excess As we observed a sub-picosecond carrier lifetime of 780 fs, which should be well suited for photomixing applications.

*Supported by EU*

**Collaboration:** [1]Université de Savoie, Le Bourget-du-lac, France

# Equipment

*M. Friedrich*
*W. Bürger*
*S. Turuc*

**Operation and development of the electrostatic accelerators**

The *2 MV VdG* accelerator has been used exclusively for RBS analysis. The old analysing magnet has been replaced by a new double-focusing magnet including a highly-stabilized power supply (Danfysik). The *5 MV Tandem* has been applied mainly for ion beam analysis and high-energy implantation. The control system of the Cs sputter ion source injector has been modernized. Using hydrogen ions split from $(NH_2)^-$ ions during the stripper process, the lowest final energy for $H^+$ and $D^+$ ions could be reduced from 1.6 MeV to 0.85 and 0.89 MeV, respectively. The *3 MV Tandetron* has been applied mainly for high-energy implantation and ion beam analysis. An additional injector for $He^-$ ions and a dedicated beam line with an commercial implantation end station (EATON NV-10) have been installed. A modified Cs sputter ion source is in operation since July 2002 without any maintenance (see extended report). In 2003 the total operating hours of the high-energy accelerators were 1420 h (VdG), 2378 h (Tandetron) and 1906 h (Tandem).

*Ch. Akhmadaliev*
*M. Friedrich*
*W. Bürger*
*J. von Borany*
*T. Gebel*[1]

**A new He implantation facility at the 3 MV Tandetron**

An additional injector has been developed and installed at the 3 MV Tandetron to increase the beam current for high-energy implantation of He ions and to provide an alternative ion source for industrial service implantations. Positive He ions are extracted from a duoplasmatron source with a beam current of 1-1.5 mA at an ion energy of 20-25 keV. The transmission of the Li charge exchange canal is about 50 %. Nearly 0.5 % of the transmitted positive He ions are converted into negative ones. The injector provides a maximum $He^-$ ion current of 3-3.5 μA at the entrance of the accelerator. On the high-energy side of the Tandetron a dedicated implantation beam line was installed which is connected with an EATON NV-10 end station for large-throughput He irradiation of Si-wafers for power devices. These services are performed in a close collaboration with the "nanoparc" spin-off company.

**Collaboration:** [1]nanoparc GmbH, Dresden

*F. Eichhorn*
*J. Sass*[1]
*K. Mazur*[1]
*A. Bauer*

**ROBL materials research goniometer: Improvement of the analyzer resolution**

High-resolution XRD investigations like stress relaxation studies in $In_{0.1}Ga_{0.9}As/GaAs$ epitaxial layers require besides a low-divergence incident beam an analyzer unit of a similar resolution. Therefore, the usual detector slit system at ROBL was replaced by a channel-cut analyzer (CCA) which reduces the analyzer acceptance angle by a two-fold diffraction of the beam at the walls of the channel in monolithic Ge. Using the (220) reflection the accessible energy ranges from 6.2 keV to 13.7 keV. The detailed characterization yielded an acceptance angle of 17 ", which is close to the calculated (ideal) resolution of 12 ". The intensity is reduced by a factor ≈ 10…1000 without, however, imposing severe limitations for specular reflection or single-crystal diffraction studies. The highest improvement of resolution was found for a symmetric beam path. The CCA may be used for reciprocal space mapping and reflectivity studies.

*Supported by BMBF*

**Collaboration**: [1]Institute of Electronic Materials Technology, Warsaw, Poland

# Glossary

| | |
|---|---|
| AES | Auger Electron Spectroscopy |
| AFM | Atomic Force Microscopy |
| AMS | Atomic Mass Spectrometry |
| CVD | Chemical Vapour Deposition |
| EEPROM | Electrically Erasable Programmable Read-Only Memory |
| EL | Electroluminescence |
| ERDA | Elastic Recoil Detection Analysis |
| ESRF | European Synchrotron Radiation Facility, Grenoble |
| FIB | Focused Ion Beam |
| FTIR | Fourier Transform Infrared Spectroscopy |
| GDOS | Glow Discharge Optical Spectroscopy |
| GIXRD | Gracing Incidence X-ray Diffraction |
| HRTEM | High-Resolution Transmission Electron Microscopy |
| IBAD | Ion Beam Assisted Deposition |
| ITO | Indium-Tin Oxide |
| LED | Light Emitting Diode |
| MBE | Molecular Beam Epitaxy |
| MOS | Metal-Oxide-Semiconductor |
| MOSFET | Metal-Oxide-Semiconductor Field Effect Transistor |
| NRA | Nuclear Reaction Analysis |
| OES | Optical Emission Spectroscopy |
| PAS | Positron Annihilation Spectroscopy |
| PIGE | Proton-Induced Gamma-Ray Emission |
| PIII | Plasma Immersion Ion Implantation |
| PIXE | Proton-Induces X-ray Emission |
| RHEED | Reflection-High Energy Electron Diffraction |
| ROBL | ROssendorf Beam Line (at the ESRF) |
| RBS | Rutherford Backscattering Spectroscopy |
| RBS/C | Rutherford Backscattering Spectroscopy under Channelling Conditions |
| RT | Room Temperature |
| RTA | Rapid Thermal Annealing |
| SAD | Selected Area Diffraction |
| SEM | Scanning Electron Microscopy |
| SIMS | Secondary Ion Mass Spectrometry |
| SPIS | Slow Positron Implantation Spectroscopy |

| | |
|---|---|
| STM | Scanning Tunneling Microscopy |
| TEM | Transmission Electron Microscopy |
| ToF-SIMS | Time-of-Flight Secondary Ion Mass Spectrometry |
| TRIM | Trajectories of Ions in Matter (Computer-Program) |
| XANES | X-ray Absorption Near Edge Structure |
| XPS | X-ray Photoelectron Spectroscopy |
| XRD | X-ray Diffraction |
| XTEM | Cross-Section Transmission Electron Microscopy |

# Supporting Institutions

| | |
|---|---|
| AiF | Arbeitsgemeinschaft Industrieller Forschungsvereinigungen e.V. |
| AvH | Alexander-von-Humboldt Stiftung |
| BMBF | Bundesministerium für Bildung und Forschung |
| BMWA | Bundesministerium für Wirtschaft und Arbeit |
| DAAD | Deutscher Akademischer Austauschdienst |
| DFG | Deutsche Forschungsgemeinschaft |
| EU | European Union |
| MPG | Max-Planck-Gesellschaft |
| SMWK | Sächsisches Staatsministerium für Wissenschaft und Kunst |
| SMWA | Sächsisches Staatsministerium für Wirtschaft und Arbeit |
| WTZ | BMBF-Programm der „Wissenschaftlich-Technischen Zusammenarbeit“ |